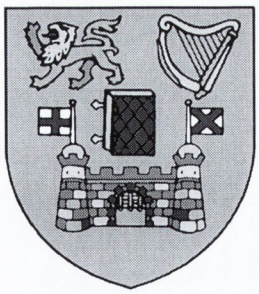

Multiphoton Processes in a Series of Designer Organic Materials

By

Margaret Elizabeth Brennan

submitted for the degree of

Doctor of Philosophy

in the

University of Dublin

Department of Physics

Trinity College Dublin

November 2001

Declaration

I declare that the work in this thesis has not been previously submitted as an exercise for a degree to this or any other university.

The work described herein is entirely my own, except for the assistance mentioned in the acknowledgements and the collaborative work mentioned in the list of publications.

I agree that Trinity College Library may lend or copy this thesis on request.

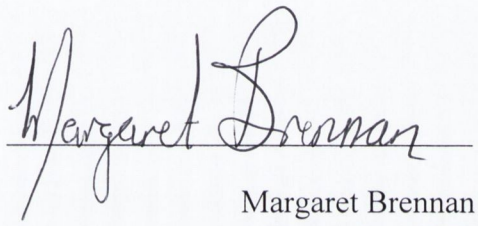

Margaret Brennan
November 2001

Pour Patrick, pour tout.

Castleiney

The evening sun sinks slowly o'er the City's gloomy brow
As wearily I make my way to where I call home now
Through crowded streets where strangers meet, so alien to me
Ti's times like this that I always miss my own Castleiney

When bright lights pall, when shadows fall, when one feels just a fool
When daily grind dulls soul and mind ti's then I long to be
Neath the homely skies, the simple joys of sweet Castleiney

For my heart still goes where the Iney flows, through woodland hill and dell
Through the golden yields and verdant fields which memory calls so well
The Washpen scene so calm more as I did of yore through my own Castleiney

By Crannagh grove my memory roves through silent Ballinroe
Through bog and moor 'round Gortdalure through Strouge and Laha too
Through Cobbs, Aughall loved places all, Through ancient Templeree
And I breathe a prayer that God will care for my own Castleiney

Ballinlass's sheen and sweet Gurteen e'er remain with me
The homely folk 'round old Kilcoke, Cuguilla, Kilkurkee
And fond thoughts span from Kilanigan to Kylemore's lovely lea
The townlands all that I recall 'round Castleiney

Where cares and few and friends are true and Winter slips away
The Springtime new and Summers blue and harvest time so gay
Where loads are light and days are bright, in happy company
For God's good grace shows every place in good Castleiney

For wealth for fame, what foolish aim that so deluded me
To leave behind a place so kind, so sweet in memory
To rue the day I sailed away across the lonely sea
And, a stranger roam, far from my home in loved Castleiney

Robert Mahony (1909 – 1996)
Poet & Playwright

Acknowledgements

The enlightenment received while working for this thesis extended far beyond the scope of the physical sciences. For these experiences, I am indebted to many people. Firstly, I would like to thank Prof. Werner Blau for the many opportunities granted, and the support and inspiration provided throughout. I am grateful to those who provided guidance and expertise; Dr. David Gray, Dr. Jonathan Coleman, Dr. Takeyuki Kobayashi, and I would also like to thank Dr. Hugh Byrne, Dr. Alan Dalton, and Dr. Shay Curran, who offered consultation and encouragement at various stages.

For technical support, provision of materials and other kinds of aid, I am grateful to, Jean-Edouard Communal, Dr. Brendan McCarthy, Dr. Sean Martin, Kieran Ryder, Tom Burke, Jeannette Cummins, Sean O'Flatherty, Anna Drury, Dr. Stefanie Maier, Bernd Lahr, Martin Cadek and Robert Murphy.

There are many people, whose character and humour helped make the bad times good, and the good times even better. The contingent who introduced me to the group includes; Ines, Dave, Rob, Sandhya, Alan, Kieran, Shay and Diarmuid. The present contingent includes Patrick, Jean, Bernd, Stephen, Colin, Sean, Adam, Brendan, Valerie, Brian, Johnny, Keith, Rob, Sandy, Anna, Steffi, Taky, Michael, Manuel, Martin, Mathew, Marie-Laurence, Cathriona, Kevin and Grace.

Finally I wish to thank my family and especially my father, for their support.

Abstract

Multiphoton processes in a series of promising organic materials; an endohedral metallofullerene, La@C_{82}, carbon nanotubes and a set of axially substituted phthalocyanines have been studied.

Linear optical studies were used to examine each of the materials and providentially resulted in the first optical detection of van Hove singularities (VHS), in multiwalled carbon nanotubes (MWNT). These VHS, which are energy levels with very high associated density of states, were observed from the visible spectral region through to the infrared.

Extensive nonlinear optical characterisation of the materials was carried out. Large, broadband reverse saturable absorption behaviour in La@C_{82}, indicates the suitability of these materials for optical limiting purposes. MWNT showed large broadband ultrafast refractive nonlinearities. VHS were found to greatly influence the nonlinear absorption behaviour of MWNT with significant saturable absorption occurring in the region of the VHS peaks. The axially substituted phthalocyanines showed tunable reverse saturable absorption behaviour.

Unexpected visible/NIR photoluminescence from MWNT, observed using near infrared excitation, was also attributed to the presence of VHS. The nonlinear excitation is believed to be resonantly enhanced by the presence of the VHS. It is suggested that luminescence is produced as a result of the radiative transition rate becoming appreciably large in the region of the VHS absorption. These results suggest that VHS can facilitate efficient nonlinear optical activity in MWNT.

Optical limiting is found to be a suitable application for these materials. La@C_{82} in particular is found to exhibit a large figure of merit and a broadband response. In the axially substituted phthalocyanines, effective control of their optical limiting performance was demonstrated by means of chemical adjustment of the dipole moment of the axial substituent, hence enabling modulation of the response. MWNT showed effective broadband optical limiting behaviour using nanosecond irradiation, which is believed to originate from nonlinear scattering. MWNT also possess a high refractive nonlinearity suitable for ultrafast switching purposes.

Contents

Tables and Figures

Chapter 1
Introduction

A multiphoton process refers to the interaction of more than one photon in a medium, in any single event. Such processes deviate from linear optics and fall within the regime of nonlinear optics. It is well accepted that the realisation of efficient multiphoton interactions, in suitable media, for which purpose organic materials have been earmarked as promising candidates, would revolutionise the technological world. The relevance of multiphoton processes and the motivation for their investigation is described here. Also presented is an overview of the studies undertaken during the course of this thesis.

1.1 Scientific Background

The tumultuous rate of progress in electronics technology means that the limitations of this technology are fast being approached. Continued advancement relies on further device miniaturisation and increased processing speed. However, in electronics, which is the basis of current technology, the boundaries for these improvements are being approached. Photonics, involving multiphoton processes, provides an exciting answer to these problems.

Photonics is analogous to electronics in that it describes the technology in which photons instead of electrons are used to acquire, store, transmit and process information[1]. Most attractive is the fact that photonics enables processing of information at the speed of light. Optical circuits can also carry more information than their electrical counterparts, due to larger bandwidths, lower loss and cross talk. Realisation of these photonic capabilities would give rise to the emergence of the new age of 'optopia'.

The realisation of photonics technologies depends on two main factors; the existence of appropriate optical techniques and suitable optical interconnects. The invention of the laser and the discovery of multiphoton processes fulfil the first of these criteria. The powerful coherent nature of laser light can be used to perform intricate optical interactions in materials in a controlled and precise manner. Most important for photonics technology was the discovery that the properties of materials behave in a nonlinear manner under intense laser irradiation. This gave rise to new optical phenomena and the field of study known as nonlinear optics. The nonlinear response of materials, which arises from multiphoton interactions with light, offers the possibility of controlling optical signals using external electric fields and light sources.

The second factor required for photonic technologies are suitable materials, which can facilitate efficient multiphoton processes and form the building blocks of optical circuits. At present, the ideal materials for this purpose remain elusive. The design and optimisation of suitable materials is the focus of much research and the quest to find ideal materials is ongoing. As candidates, organic materials have many positive attributes including; their ability to support considerable multiphoton interactions and hence produce large and ultra fast nonlinear optical responses, their architectural flexibility, high optical damage thresholds, and ease of fabrication as well as low production cost[2,3]. During the past decade, organic materials have begun to encroach on areas traditionally dominated by inorganic semiconductors for electronic applications. Polymeric devices have been developed, such as photodiodes[4], photovoltaic cells[5], field effect transistors[6], optically pumped lasers[7] and recently, commercial products based on polymeric LED devices have begun to be marketed by such companies as Phillips, Uniax Corporation, and Cambridge Display Technologies. Progress continues to be made in the nonlinear optical properties of organic materials for the photonics applications. In the future, stable optically clear organic materials may be as important to photonics as inorganic semiconductors have been to electronics.

The field of organic materials for photonic applications encompasses a wide range of interesting materials including the familiar polymers or plastics, the naturally occurring prophyrins and their phthalocyanine relatives, as well as fullerenes and

carbon nanotubes. The capacity of these materials to accommodate substantial multiphoton interactions has a common origin: the π-electrons. These, π-electrons are not tightly bound to the individual nuclear sites, and thus their orbitals extend over long distances, hypothetically spanning an entire molecule or even a macroscopic solid[8]. Such π-electron distributions are characteristic of unsaturated organic compounds and render these molecules highly polarisable, due to the relative ease with which optical fields can affect the electronic motions.

Initial advances in organic materials, were in the area of polymers, with linear rigid polymers such as polydiacetylenes receiving widespread attention[9]. Endeavours to improve the material nonlinear response included the incorporation of metals and the addition of supplementary groups and chromophores[9]. Modified polymer materials were designed with a view to all optical switching processes. Aromatic compounds such as the prophyrin molecules, found in many living systems, also showed many promising features[10]. These were followed by the closely related phthalocyanine molecules, which showed much chemical flexibility and were found to be particularly suitable for optical limiting purposes[11].

A pioneering breakthrough in the field of organic materials came in 1985, with the discovery of a third allotrope of carbon, the C_{60} molecule, or Buckminster Fullerene[12]. The C_{60} molecule has since become the prototypical member of a vast class of carbon cage molecules collectively known as the fullerenes. Other fullerene members include; C_{70}, C_{76}, C_{78}, and C_{80}. The versatility of fullerenes stems, in part, from the possibility of doping either by attaching atoms to the outer bonds of the cage or by inserting one or more atoms inside the cage. Encapsulation of one or more metal atoms inside fullerene cages (endohedral metallofullerenes) has the potential of creating new species or materials with new properties, unexpected for hollow fullerenes. Recent progress is marked by the successful production of several endohedral fullerene species including one studied here, La@C_{82}[13]. For successful fullerene applications, it is interesting to investigate how increased fullerene size and how modification by endohedral doping affects multiphoton interactions and influences the nonlinear optical properties compared to smaller hollow fullerenes.

In 1991, a new subfamily of the fullerenes, the carbon nanotubes were discovered[14]. These tubular fullerenes have captured the imagination of researchers around the world. Just nanometres in diameter, these cylindrical tubes can be tens of microns long, with each end "capped" with half fullerene molecules. Carbon nanotubes occupy a unique intermediate position between molecule and material and have an impressive list of attributes. They can behave like metals or semiconductors, can conduct electricity better than copper, can transmit heat better than diamond, and they rank among the strongest materials known[15]. Regarding their nonlinear optical properties, carbon nanotubes posses many of the attributes which can contribute to a large nonlinear optical response and theoretical predictions indicates significant nonlinear optical activity[16,17]. They possess the necessary conjugation, which in the case of nanotubes has the advantage of being very extensive providing a large area, which can support multiphoton interactions. In addition, the π-electron delocalisation is confined to one dimension, which is expected to produce a large optical nonlinearity. An extra factor, which can be expected to greatly influence the nonlinear optical response in carbon nanotubes, results from the quantum confinement in nanotubes. The reduced dimensionality of carbon nanotubes gives rise to singularities in their electronic density of states[17]. Multiphoton processes are expected to be significantly, enhanced at energies that are resonant with density of state singularities.

Beyond their usefulness for technological applications, the nonlinear optical properties of a medium and the multiphoton interactions that it supports can shed light on the nature of the medium itself. Multiphoton spectroscopy can be used to probe energy transitions, and other bulk and molecular properties of a material that are not accessible by other spectroscopic methods. The increased complexity of materials, as in the case of the fullerenes and in particular the carbon nanotubes, means that complete characterisation and understanding of certain materials is difficult using just the traditional linear spectroscopic methods. Investigation of the multiphoton processes which give rise to the nonlinear optical properties can result in a better understanding of the fundamental nature of the material.

This thesis presents a detailed study of a variety of the latest organic molecules designed for nonlinear optics; the endohedral metallofullerene, La@C_{82}, carbon

nanotubes and a set of axially substituted phthalocyanines. Each of these materials possess individual features, which are expected to enhance their nonlinear optical properties. La@C_{82} is an opportune species incorporating a heavy metal charge transfer complex within a fullerene structure. Carbon nanotubes posses many remarkable electronic properties of which quantisation induced van Hove singularities, which are energy levels with very high associated density of states, are of particular interest here. Axial substitution is a new approach in the area of chemical modulation of the nonlinear optical response in phthalocyanine materials.

These materials form a model set, spanning a range of spatial dimensions and topologies. The fullerenes present as quasi zero-dimensional materials, with a spheroidal structure while the carbon nanotubes are essentially one-dimensional systems with rod like structures or quantum wires. The phthalocyanines represent the two-dimensional system based on a planar configuration. This systematic variation in the structure is reflected in their electronic and optical properties. This in turn is shown to have a profound effect on their nonlinear optical response.

The object of these studies is two fold. The first is to identify materials, which have potential for photonic applications and ascertain how these materials can be optimised. The second objective is to use the knowledge gained from investigations of the material nonlinear optical responses to gain an insight into and elucidate further information about the electronic properties of these materials.

Thesis Outline

A range of organic materials, namely a set of axially substituted phthalocyanines, a lanthanum endohedral fullerene and carbon nanotubes are selected for multiphoton investigations. The objective is to determine their performance as photonic materials and use this information elucidate properties of these materials.

Chapter 2 reviews the general properties of organic materials and these are then applied to the materials studied here, the endohedral fullerene La@C_{82}, carbon nanotubes and phthalocyanines. This includes a discussion of their structural and electronic properties and an account of their particular attributes for nonlinear optical functions. A second section is devoted to the background theory of

nonlinear optics and the multiphoton processes of relevance to the studies carried out here.

Chapter 3 presents the characterisation of the basic properties of the materials in view of their influence on their multiphoton processes and hence their nonlinear optical performance. The experimental methods employed are described and the results of the characterisation are used to establish an understanding and to build a profile of the materials. This information is used to give an insight into how various aspects of the materials will affect their nonlinear optical properties.

Chapter 4 details the characterisation of the material nonlinear optical properties. A description of the nonlinear optical techniques used, z-scan and degenerate four wave mixing is given. Analysis of the results of the nonlinear investigations is used to designate which particular photonic tasks the materials might be suited. Their nonlinear optical behaviour is also related back to their linear optical properties.

Chapter 5 gives details of a new phenomenon, the observance of unexpected nonlinear photoluminescence from multiwalled carbon nanotubes. A multiphoton absorption mechanism is suggested involving interactions from van Hove singularities, which are energy levels with very high associated density of states regions arising due to the unique electronic properties of carbon nanotubes.

Chapter 6 presents an investigation of multiphoton absorption for the application of optical limiting in the materials studied here. The various merits of the materials are analysed.

Finally, Chapter 7 concludes this thesis, by reviewing the research presented here and addressing its implications.

References

[1] T. Kobayashi, Optoelectronics - Devices and technologies **8** *309* (1993).

[2] J. Messier, F. Kijzar, and P.N. Prasad, *Organic Materials for Nonlinear Optics and Photonics*. Kluwer, Drodrechti, 1991.

[3] H.S Nalwa, Adv. Mater. **5** *341* (1993).

[4] J.J.M. Halls, C.A. Walsh, N.C. Greenham, E.A. Marseglia, R.H. Friend, S.C. Moratti, and A.B. Holmes, Nature **376** *498* (1995).

[5] J.J.M. Halls, D.R. Baigent, F. Cacialli, N.C. Greenham, R.H. Friend, S.C. Moratti, and A.B. Holmes, Thin Solid Films **276** *13* (1996).

[6] J.H. Burroughs, C.H. Jones, and R.H. Friend, Nature **335** *137* (1988).

[7] N. Tessler, G.J. Denton, and R.H. Friend, Nature **382** *695* (1996).

[8] J Zyss, *Molecular Nonlinear Optics*. Academic Press, New York, 1994.

[9] C. Sauteret, J.P. Hermann, K. Frey, J. Ducuing, R.K. Chance, and R.H. Baughmann, Phys. Rev. Lett **36** *956* (1976).

[10] F. Z. Henari, W. J. Blau, L. R. Milgrom, G. Yahioglu, D. Phillips, and J. A. Lacey, Chemical Physics Letters **267** *3-4*, 229 (1997).

[11] H.S. Nalwa and J.S. Shirk, *Phthalocyanines, Properties and Applications*. New York, 1996.

[12] H.E. Kroto, J.R. Heath, S.C. O'Brien, R.F. Curl, and R.E. Smalley, Nature **318** *162* (1985).

[13] Y. Chai, T. Caio, C Jin, R.E. Haufler, L.P.F. Chibante, J. Fure, L. Wang, J.M. Alford, and R.E. Smalley, J. Phys. Chem. **95** *7564* (1991).

[14] S. Iijima, Nature **354** *56* (1991).

[15] M. Dresselhaus, G. Dresselhaus, and P.C. Eklund, *Science of Fullerenes and Carbon Nanotubes*. Academic Press, San Diego, 1996; M. S. Dresselhaus, Abstracts of Papers of the American Chemical Society **218**, 34 (1999).

[16] V. A. Margulis, E. A. Gaiduk, and E. N. Zhidkin, Diamond and Related Materials **8** *7*, 1240 (1999).

[17] P. Kim, T. W. Odom, J. L. Huang, and C. M. Lieber, Physical Review Letters **82** *6*, 1225 (1999).

Chapter 2
Materials and Nonlinear Optics Background

Targeting organic materials for photonic applications requires collaboration between the disciplines of material synthesis and nonlinear optics. The production of suitable nonlinear optical materials entails the design of structures and the incorporation of species, which enhance their capacity to support multiphoton interactions and give rise to a large nonlinear optical response. Here we review the basic physics of organic materials and nonlinear optics and these concepts are then used to understand the origin of nonlinear optical processes in organic materials

2.1 Organic Materials

The term organic material is used to refer to all materials whose chemistry is determined by their carbon atoms. They encompass a vast range of materials, from methane to polymers, fullerenes and nanotubes, large macrocyclic molecules such as the phthalocyanines and most biological materials. For this work a series of these materials including an endohedral metallofullerene, La@C_{82}, carbon nanotubes and a set of phthalocyanine molecules are selected. Each of these materials, posses their own particular attributes which increase their capacity for multiphoton processes and promise an improved nonlinear optical performance.

2.1.1 Basic Concepts of Organic Materials

Carbon is a remarkable element forming a variety of stable configurations, not only with itself but also with other elements. The adaptability of carbon relates to the many possible arrangements of the electronic states of the carbon atom. The carbon

atom has six electrons, which occupy $1s^2$, $2s^2$, and $2p^2$ atomic orbitals with the $1s^2$ orbital containing two core electrons and the remaining four electrons occupying the $2s^2 2p^6$ valence orbitals. The energy difference between the upper 2p and lower 2s energy levels in carbon is small compared with the binding energy of chemical bonds and therefore the electronic wavefunctions for these four electrons can readily mix with each other in a process known as hybridisation. In carbon, three possible hybridisations can occur: sp, sp^2 and sp^3, where the superscript indicates the number of 2p electrons which are involved. The various bonding states are related to certain structural arrangements, so that sp bonding gives rise to chain structures, sp^2 bonding to planar structures and sp^3 bonding to tetrahedral structures.

The type of carbon hybridisation adopted in a molecule is strongly reflected in its properties. In sp^3 bonded molecules all the electrons are tightly bound in . bonds. Due to the high bonding energy of these bonds, it takes a large amount of energy to excite these electrons, and they tend to be relatively inert. In sp^2 hybridisation, three of the valence electrons are involved in bonding leaving the fourth electron on each carbon atom unaffected in the unhybridised p_z orbital. The p_z orbitals are arranged in a dumbbell shape out of plane and form π bonds.

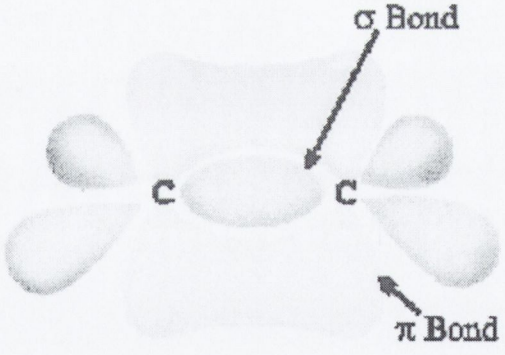

Figure 2.1 Example of σ and π bonds

These π-electron orbitals overlap to form extensive delocalised molecular orbitals. These bonds are weaker and much more delocalised, therefore requiring much less energy to excite them. Excitations of the π-electrons can therefore produce a large perturbation of the molecular orbital and enable the induction of a large polarisation.

Organic molecules in which sp^2 bonding dominates are conjugated, which means they are composed of alternating carbon single and multiple bonds and so exhibit π-bonding. This is the feature of most importance for the nonlinear optical performance of an organic material.

2.1.2 Chemical Structure

The versatility of carbon results in conjugated structures, which span a range of dimensions and topologies. Long chain polymers are examples of one-dimensional systems. Aromatic rings form the basis of many two–dimensional structures while cage molecules, namely the fullerenes, have a three-dimensional delocalisation of the π-electrons. A vast array of molecular configurations can be created from these basic structures.

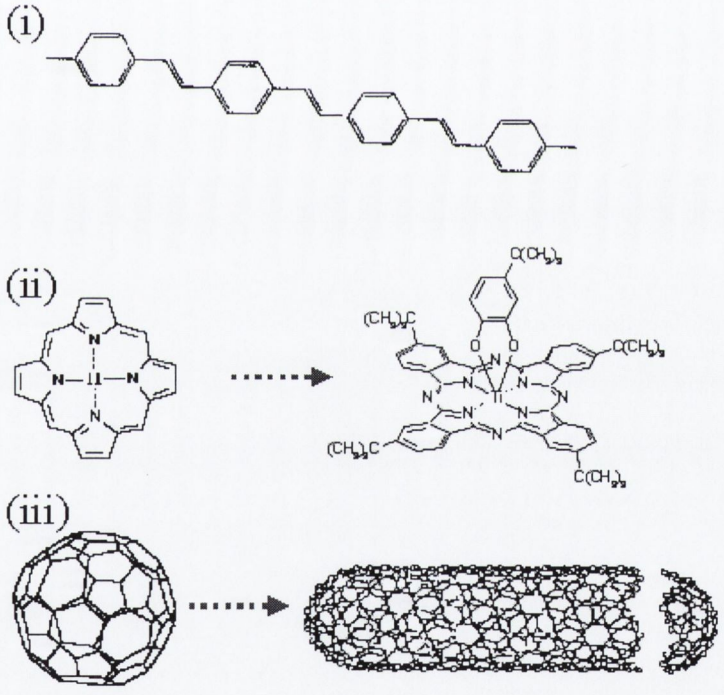

Figure 2.2 Examples of organic compounds
(i) Linear polymer PPV, (ii) Aromatic Pyridine and an axially substituted Ti:Phthalocyanine, (iii) Primary Fullerene C_{60} and a Carbon Nanotube

The structure of organic molecules can be manipulated almost as desired using chemical techniques. Examples of basic organic structures and some of their more elaborate counter parts are shown in figure 2.2. Both the linear and nonlinear

optical parameters of a molecule are strongly dependent on their conformational and chemical structure. An understanding of how molecular structure relates to its capacity for multiphoton interactions and hence its nonlinear optical performance is essential in the design of materials with enhanced nonlinearities. Although a large body of information exists on this subject, the story is not yet complete. The creation of new materials and their optimisation continues, giving rise to more information and new criteria which serve to further develop the understanding of the interplay between material structure and its nonlinear response.

2.1.3 Electronic and Photophysics Properties of Organic Molecules

The electronic levels and photophysical processes in organic materials can be represented schematically in a Jablonski diagram such as that shown in figure 2.3. In this scheme the molecular electronic levels are divided into singlet and triplet levels. These electronic levels are vibrationally broadened to form bands. A variety of excitation and relaxation transitions can occur, which can be either radiative or non-radiative. The transitions are represented as lines; dashed lines denote non-radiative transitions while solid and wavey lines denote radiative transitions.

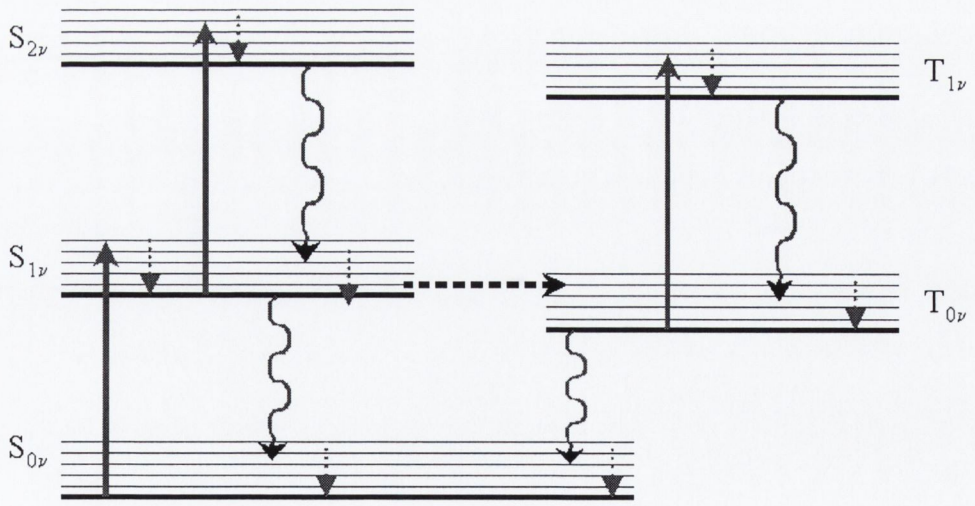

Figure 2.3 Jablonski diagram of photophysical processes

Selection rules govern the possible transitions that may take place. The selection rules are different for single and multiphoton events. Single photon transitions may

only occur between states of opposite parity, while two photon events, which are responsible for a variety of nonlinear optical phenomena, can only occur between states of even parity. These rules can be relaxed to a certain extent by such processes as spin orbit coupling and symmetry breaking interactions.

The most familiar radiative excitation is ground state absorption where a molecule is excited from its lowest ground state into a vibrational level in the first excited state. The probability of this transition is given by the ground state absorption cross section σ_0, which is related to the ground state absorption coefficient by, $\alpha_0 = \sigma_0 N_0$, where N_0 is the number density of the absorbing species. Absorption processes are extremely rapid and occur on a timescale of $\sim 10^{-15}$ s.

Absorption is also possible out of an excited state in a multiphoton process known as excited state absorption. Excited states of molecules can also be populated by a multiphoton processes in which more than one photon is simultaneously absorbed from the radiation field. The probability of N photons being absorbed by a molecule at a given point in space and in time is directly proportional to the N^{th} power of the density of photons per area unit per second. It therefore follows that these processes are likely to occur only at high intensities.

Following a molecule's excitation into a vibronic level of an excited state, it will rapidly cascade down the vibrational manifold. This is a thermal nonradiative process, which occurs on a timescale of 10^{-13} s. Once in the lowest vibrational level of its excited state the molecule may then relax radiatively into the ground state vibrational manifold. If both states have the same multiplicity this process is known as fluorescence. It is a spin allowed process and occurs over a timescale of 1-100 ns. Radiative relaxation from a triplet state is known as phosphorescence and is a spin forbidden process. It is therefore a slow process occurring on a time scale of microseconds to days.

There are several processes, which may compete with radiative de-excitation, such as internal conversion, intersystem crossing and various quenching mechanisms. Internal conversion refers to isoenergetic transitions where transfer may occur between a zero vibrational level of a higher state to a high lying vibrational level of

a lower state. Intersystem crossing refers to isoenergetic transition between an excited singlet state and a triplet state. This process is spin forbidden, however it can be made possible through orbit spin coupling between states of different multiplicity. This coupling increases with atomic number Z in what is known as the "Heavy Atom Effect". Incorporation of heavy metal atoms in organic materials is often used as a method of increasing nonlinear absorption.

2.1.4 Low Dimensional Materials

Low dimensional materials refer to material structures, which cannot be described in terms of either molecular or bulk structures, but have an intermediate structure that extends to less than three dimensions. This may be because their lattice structures resemble sheets (two dimensional) or needles (one-dimensional) or clusters (zero-dimensional) with their short dimensions going to the scale of atoms (i.e. nanometre, nm). Such low dimensional materials are of interest since they allow fundamental theories of one and two-dimensional systems to be tested experimentally. Studies of the properties of quasi-low dimensional material have taken on added significance with the continued reduction in size of microelectronic devices since low dimensional effects are becoming increasingly dominant in such devices.

Carbon nanotubes constitute ideal low-dimensional materials possessing many remarkable properties, which are derived from their reduced dimensions. The electronic properties in low dimensional systems cannot be readily treated using the theory applied to molecular systems, but require a reduced dimension approach such as that described in section 2.3 for carbon nanotubes. The exotic properties of carbon nanotubes, which are revealed, such as a diameter dependent band gap and the presence of singularities in the density of states (DOS) have exceptional potential for the field of nanoelectronics as well as for photonic applications.

2.2 Application of Theory to Materials Studied

The general principles of organic materials presented above can be readily applied to the molecules chosen for study here. These include the endohedral

metallofullerene La@C_{82} as a representative of the fullerene family, a set of specifically designed phthalocyanine molecules, and a series of carbon nanotubes. Although these molecules present a range of contrasting structures, varying in size and dimensions they are in fact closely related. These progressive structural variations are reflected in their electronic structure and photophysical properties. Fullerenes and phthalocyanines can be treated in terms of molecular species while carbon nanotubes, which are intermediate between molecular and bulk materials, require a reduced dimension type treatment.

2.2.1 Phthalocyanines

Phthalocyanines (Pcs) are synthetic analogues of the naturally occurring porphyrin compounds. They are two-dimensional conjugated arrays, which are highly architecturally flexible. Phthalocyanines can be extensively chemical tailored allowing control over their electronic and optical properties[1]. Basic and more advanced phthalocyanine structures are shown in figure 2.4. They can accommodate a variety of substitutions; including peripheral and axial, while metals, semi-metals or hydrogens can be accommodated the centre position[2].

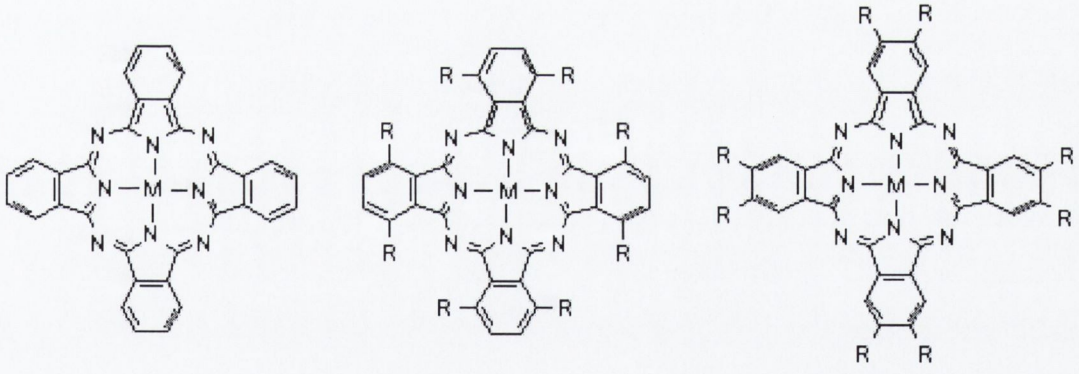

Figure 2.4 Phthalocyanine molecular structures

A case study of a set of axially substituted phthalocyanine molecules is carried out here. Axially substituents of different dipole moment strengths are attached to a

titanium phthalocyanine macrocycle and the influence of these substituents on multiphoton absorption in the phthalocyanines is investigated.

Electronic Structure and Photophysics

The absorption spectrum of phthalocyanines is characterised by two strong absorption peaks; a Q-band in the red/near infrared part of the spectrum and a B-band in the UV/blue part of the spectrum. The strong Q-band absorption is responsible for the characteristic intense blue-green colour of the compound. A window of weak residual absorption lies in between and has important implications for the multiphoton absorption behaviour of phthalocyanines. A typical linear absorption spectrum for a metal substituted phthalocyanine is shown in figure 2.5.

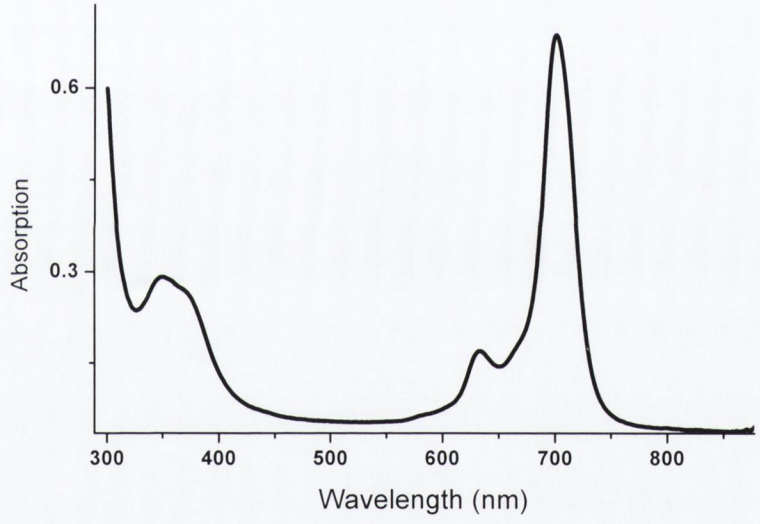

Figure 2.5 Metallophthalocyanine absorption spectrum

Multiphoton absorption in phthalocyanines can be explained with reference to a Jablonski diagram. Phthalocyanines are characterised by strong intersystem crossing between the singlet and triplet levels. This action results in a build up of the electronic population in the triplet levels and is a mechanism, which is responsible for a nonlinear absorption process known as reverse saturable absorption. This type of multiphoton absorption is facilitated by a weak linear absorption such as that which occurs in phthalocyanines between the two main bands.

Structural modifications and substitutions in phthalocyanines typically shift the linear absorption maxima and the corresponding vibronics. The main features of the linear absorption, which are due to the π-electrons within the conjugated ring, are generally retained[1].

2.2.2 Carbon Nanostructures

Graphite, which is sp^2 bonded, has a hexagonal layer structure and is an anisotropic semi-metal[3]. On the nanometric scale curved graphene structures can form[4]. Finite sized graphite has many edge atoms with dangling bonds, which are higher energy entities. The energy of such small carbon clusters is reduced by elimination of the dangling bonds[3]. This results in the formation of closed cage clusters such as fullerenes and carbon nanotubes. These species represent the third crystalline form of carbon.

2.2.3 Fullerenes

Collaborative research between Kroto, Smalley, Curl and co-workers, on unusual infrared emission from large carbon clusters in red giant carbon stars, led to the discovery of the C_{60} molecule[5]. This 60 carbon atom cluster has 7 Å diameter and is shaped like a football.

Electronic Structure and Photophysics

Fullerene C_{60} has an icosahedral symmetry structure formed with 12 pentagons separated by 20 hexagons. The high-level symmetry means that many optical transitions in C_{60} are strongly forbidden[6]. This is manifested in the absorption spectrum where absorption at the visible wavelengths is considerably weak. In figure 2.6 the absorption spectrum of C_{60} at both low and high concentrations is shown. The absorption between 450 nm and 650 nm corresponds to the HOMO-LUMO transition, which is symmetry forbidden and is only clearly visible at high concentrations.

Other significant features in C_{60} include an extremely efficient inter-system crossing and a long lived triplet state. This gives rise to an absorption mechanism similar to

that occurring in the phthalocyanines where a large electronic population can be accumulated in the triplet levels.

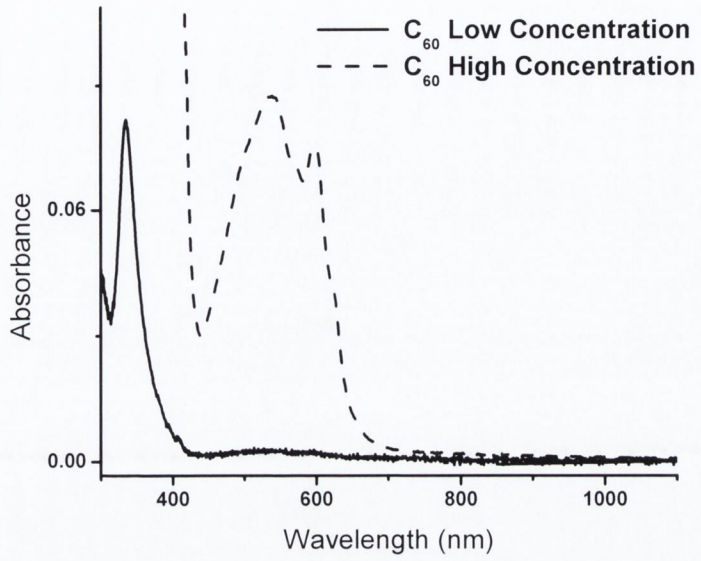

Figure 2.6 C_{60} absorption showing HOMO-LUMO band at high concentration

This feature, in addition to the low oscillator strength in the visible region, gives rise to efficient reverse saturable type multiphoton absorption in C_{60}.

Higher Order Fullerenes

Higher order fullerenes are formed by the addition of extra benzoid six-member rings. One of the main factors favouring the formation of a particular fullerene, is a structural configuration which ensures that individual pentagonal rings are isolated from each other, in what it also known as the isolated pentagon rule[7]. It is energetically more favourable to keep pentagons separated since they introduce curvature into the structure, hence increasing the local strain. According to the isolated pentagon rule, C_{60} is the smallest stable fullerene. In reality it is also the most abundant fullerene. The next most abundant is C_{70}, however beyond this the abundance of higher mass fullerenes, such as C_{76}, C_{82} and C_{84} decreases dramatically.

An increase in fullerene size leads to tubular type structures rather than larger spheroidal type structures as can be seen in figure 2.7. The reduced symmetry of these larger structures serves to relax the optical forbidden processes observed in

C_{60}. The oscillator strengths of transitions around 450 nm-600 nm increase and absorption continues into the near infra-red region.

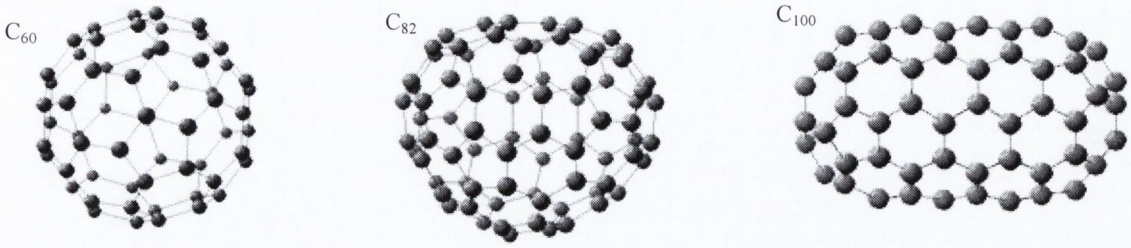

Figure 2.7 Fullerene structures

There is a pronounced change in colour of the material in solution as indicated in figure 2.8.

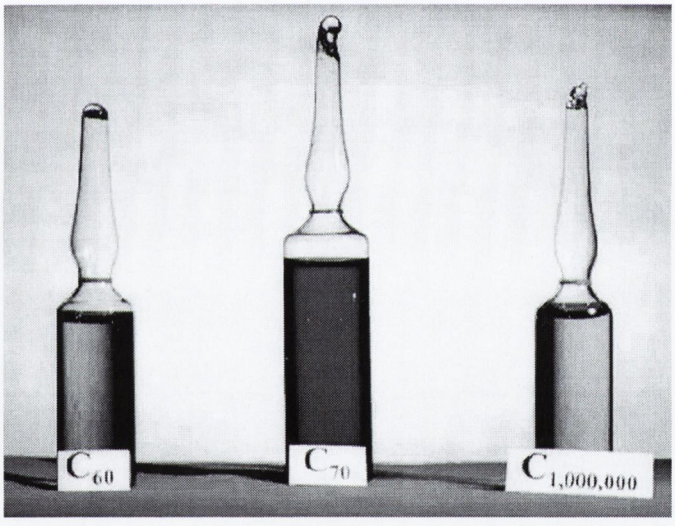

Figure 2.8 Fullerene solutions in toluene

Whereas C_{60} is magenta, C_{70} has a deep brown/orange colour and the higher fullerenes are dark brown.

2.2.4 Endohedral Fullerenes

Fullerenes have a spherical empty space inside the carbon cage. Endohedral fullerenes are formed when a small number of atoms are encapsulated inside the fullerene cage. These are generally prepared in an arc discharge generator where a

high purity oxide of the metal species to be incorporated, is combined with the graphitic electrode. Laser ablation can also be used where again the target is a composite of both the metal and carbon atoms. The endohedral metallofullerene La@C_{82} was found to be a particularly stable entity. A mass spectrum of the extracted of fullerene materials produced by laser vaporization of a 10% La_2O_3/graphite composite rod is shown in figure 2.9[3].

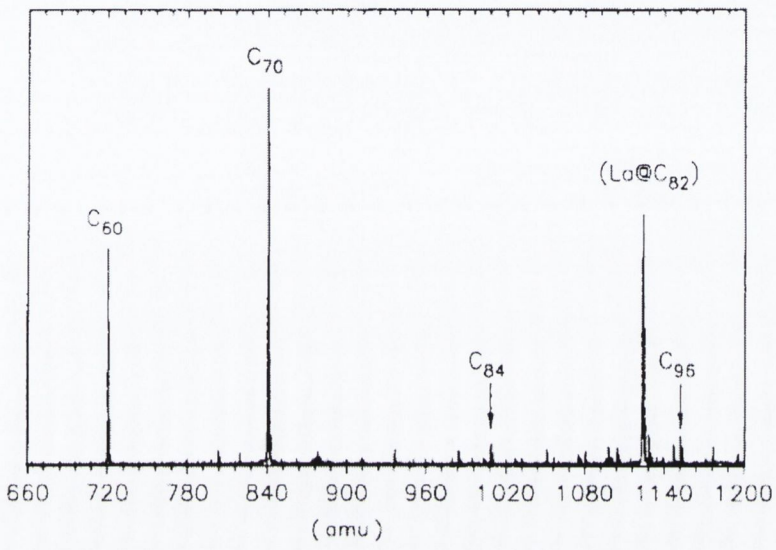

Figure 2.9 Mass spectrum of fullerene extracts produced by laser ablation[3]

As can be seen from the mass spectrum in figure 2.9, many fullerene species accompany the endohedral fullerene material including C_{60}, C_{70}, and C_{84}. However, C_{82} is not sufficiently abundant to enable it to be extracted using the necessary HPLC techniques[3] and as a result a sample of the isolated C_{82} was unavailable for investigation here. However, C_{82} is well described in the literature[3].

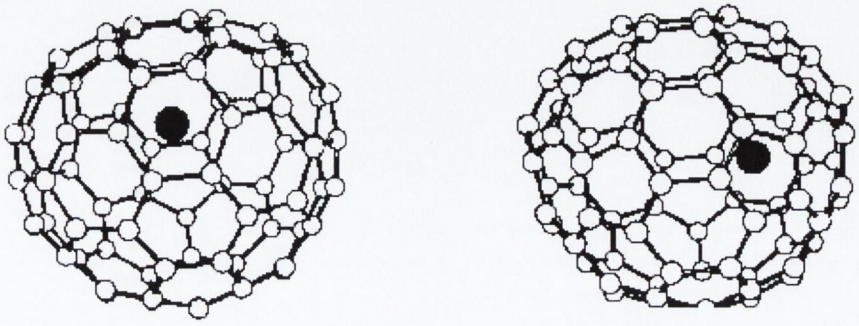

Figure 2.10 Structural models for La@C_{82} with La at different off-centre positions[8]

A model structure for the $La@C_{82}$ molecule[8] is shown in figure 2.10. Investigations of the endohedral lanthofullerene structure indicate that the La atom is displaced from the centre of the C_{82} cage by several angstroms[9]. Further study revealed that the La atom does not rest in the cage but rather is in a floating motion along the nearest six-member ring[10].

Electronic Structure and Photophysics

In endohedral metallofullerenes, substantial electron transfer takes place from the encaged metal atom to the fullerene cage, which significantly alters the electronic properties. Lanthofullerene has the charge state of $La^{3+}@C_{82}^{3-}$ with the three outer electrons of La transferring to the C_{82} cage[11]. Absorption spectra of endohedral metallofullerenes differ from those of empty fullerenes. The major influencing factors are the charge of the metal and the cage structure. Fluorescence spectra show peaks in the $La@C_{82}$, which are absent in the C_{82} spectrum[12].

2.3 Carbon Nanotubes

Carbon nanotubes are descendants of the fullerenes. These tube-like molecules called carbon nanotubes or "buckytubes" are unlike anything reported in the fullerene family and have come to be recognised as fascinating materials with nanometer dimensions promising exciting new areas of carbon chemistry and physics.

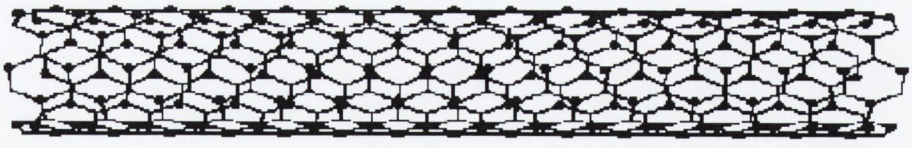

Figure 2.11 Section of a singlewalled carbon nanotube

A schematic of a section of a singlewalled carbon nanotube is shown in figure 2.11.

2.3.1 Physical structure of Carbon Nanotubes

A nanotube is essentially a single layer of graphite rolled into a tube that is closed at the ends by fullerene like caps. There are many ways in which a graphene sheet can be rolled, depending on the angle that the lattice makes with the tube axis. A nanotube of particular radius and chirality may be specified by choosing a "chiral" vector, which maps two given hexagons in the lattice onto each other. Any vector connecting two hexagons in the lattice is a linear combination of the primitive vectors with integer weight.

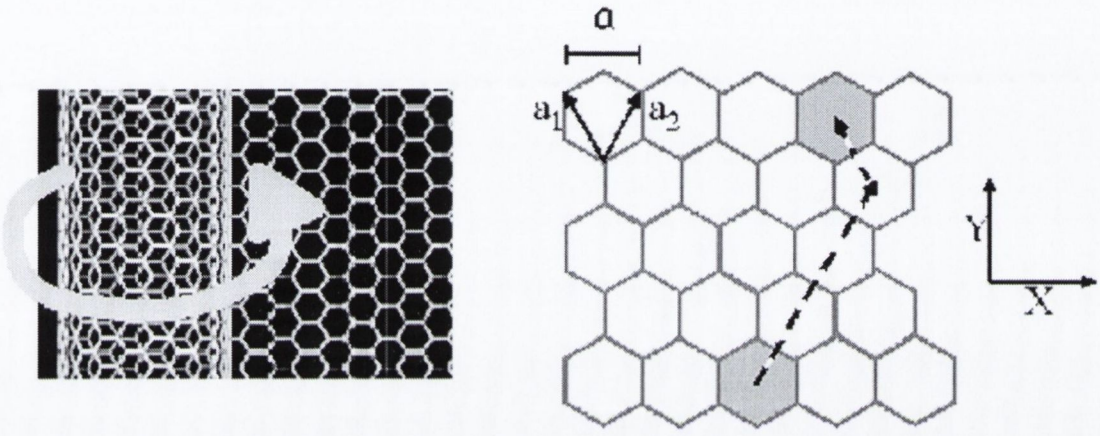

Figure 2.12 Nanotube rolled from graphene & unit vectors a_1, a_2, for (3,1) nanotube

A given nanotube is therefore associated with two indices that specify these integers. The nanotube formed by rolling the two hexagons, shown in grey, on top of each other in figure 2.12 would therefore be a (3,1) nanotube.

A general definition of the chiral vector is given by $C = na_1+ma_2$ where a_1 and a_2 are unit vectors in the hexagonal lattice and m and n are integers. A great many nanotubes chirality's can occur of which two have particularly high symmetry as depicted in figure 2.13. Chiral vectors of the form (n, 0), correspond to zigzag nanotubes in which the rows of the lattice structure are perpendicular to the nanotube axis. The opposite occurs for (n, n) chiral vectors which have bonds lying perpendicular to the nanotube axis and are known as armchair nanotubes.

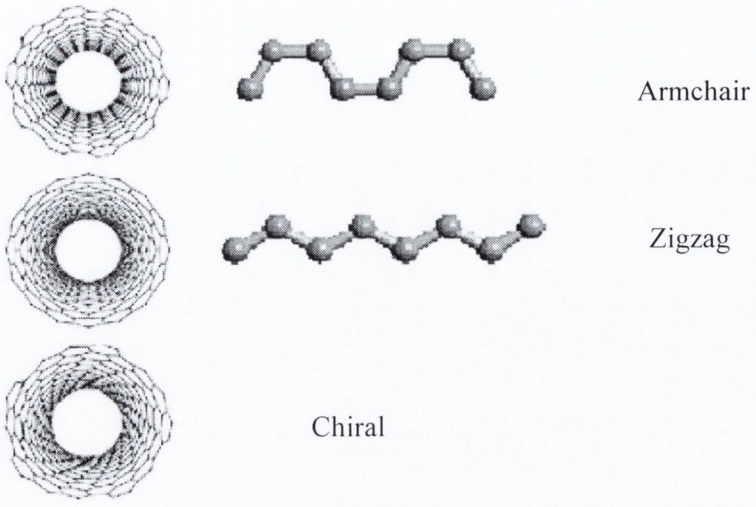

Figure 2.13 Carbon Lattice arrangement for armchair, zigzag & chiral nanotubes perpendicular to the cylindrical axis.

The (n,m) values of the chiral vector, determine all the characteristics of a nanotube, including diameter, chiral angle, and all electronic properties.

2.3.2 Electronic Structure of Carbon Nanotubes

For a very large radius tube, it can be expected that the properties of the nanotube are very similar to that of graphene.

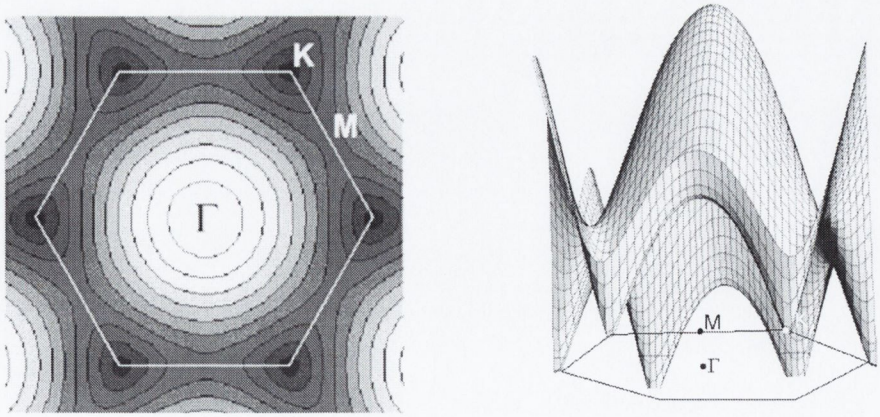

Figure 2.14 Brillouin zone of graphite

It has been found that even for small diameter nanotubes that the basic electronic properties of nanotubes may be deduced from the band structure of graphite. Graphite has a two dimensional hexagonal Brillouin zone whose corner points correspond to the points at which the conduction and valence bands touch as depicted in figure 2.14.

The band structure of nanotubes can be derived directly from that of graphite by imposing strict periodic boundary conditions for translations by the chiral vector that defines the nanotube. The periodic boundary conditions for one-dimensional nanotubes permit only certain wave vectors, k to exist in the circumferential direction. The allowed k values are then quantized in the direction perpendicular to the Chiral vector C such that $k \cdot C = 2\pi n$, where n is an integer as depicted in figure 2.15. This results in the two-dimensional Brillouin zone of graphite being reduced to the one dimension for nanotubes. Thus, the band structure of a nanotube consists of one–dimensional sub-bands. Lines are used to represent the allowed k values in figure 2.15. The nanotube may be insulating or metallic depending on whether these allowed k-values coincide with corners of the hexagon.

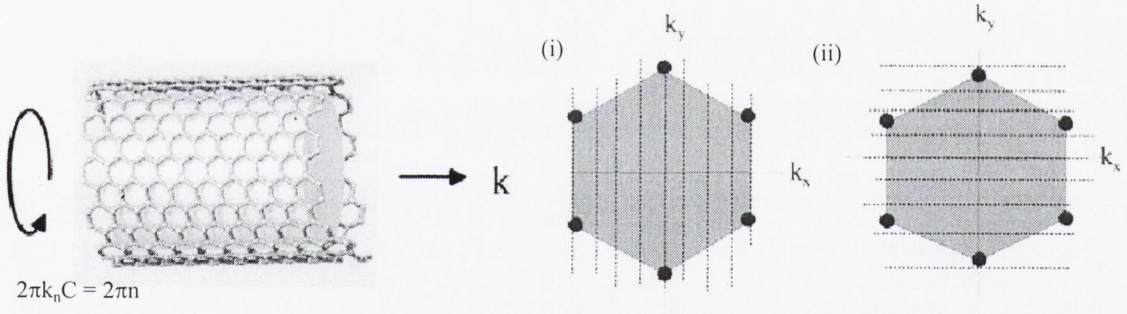

Figure 2.15 Confined electron motion along nanotube cylinder & Brillouin zones (i) metallic tube since the allowed k values pass through the corner points of the hexagon (ii)semiconducting tube[13]

In the case of tube (i) displayed in figure 2.15 the allowed k values pass through the hexagonal corner points making it metallic while tube (ii) is semiconducting. In general, an (n,m) nanotube will have a band gap unless n-m = 3p, where p is an integer[13]. Effects due to curvature result in corrections to this picture. For example,

some tubes that the above model would predict to be metallic may actually develop a small band gap.

The confinement of the electronic wavevectors gives rise to one further notable feature of the electronic structure of nanotubes. This is the presence of singularities in the density of states (DOS) of the nanotubes known as van Hove singularities. The van Hove singularities (VHS) corresponding to the calculated band structures[14] are shown in figure 2.16.

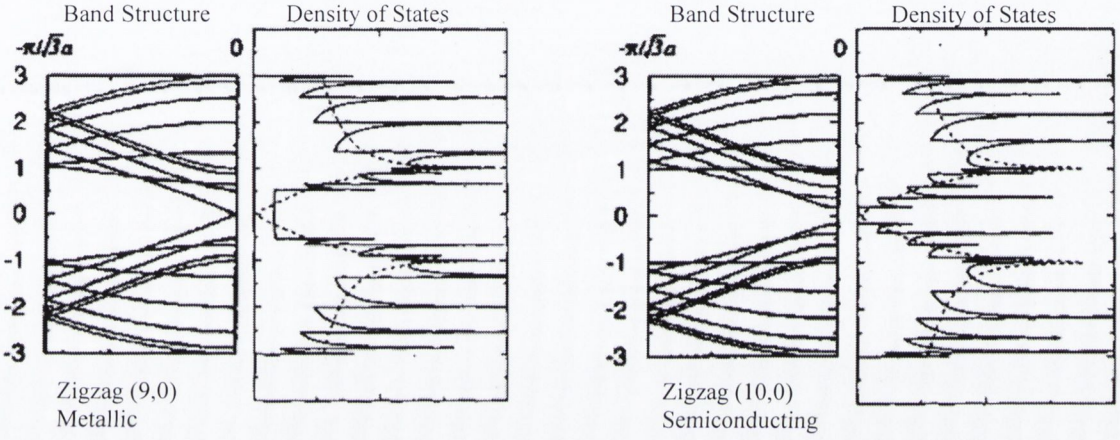

Figure 2.16 Band structure and density of state calculations for (i) a metallic tube as a finite density of states occurs at the Fermi energy. (ii) a semiconducting tube due to the presence of the bandgap [14]. In both (i) and (ii) the van Hove singularities are apparent as sharp spikes in the DOS

These are apparent as sharp spikes arranged symmetrically about the Fermi Level. The band structure of pristine graphite is indicated by the dashed lines. It can be seen that the band structure of carbon nanotubes follows the basic profile of that of graphitic with additional features induced as a result of quantisation effects. Calculations of the nanotube DOS[14] corresponding to the VHS is also shown in figure 2.16.

In figure 2.17 the electronic transitions, which can take place between mirror image singularities for various nanotubes are indicated[15]. The position of the singularities about the bandgap is noted seen to be dependent on the chiral vector of the nanotubes.

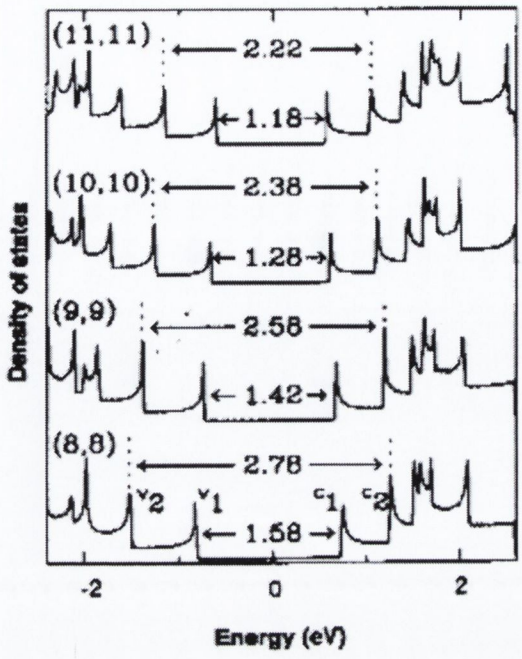

Figure 2.17 Electronic transitions between van Hove singularities[14] The arrows and corresponding energies indicate the first andsecond electronic transitions between van Hove singularities

The evolution of the singularities with tube size is also indicated and an inverse relationship between band gap and tube diameter is observed.

Singlewalled Nanotubes

The above explanation of the electronic structure of nanotubes is simplified as it refers only to an idealised single nanotube shell or singlewalled nanotubes (SWNT). In reality, the situation is much more complicated.

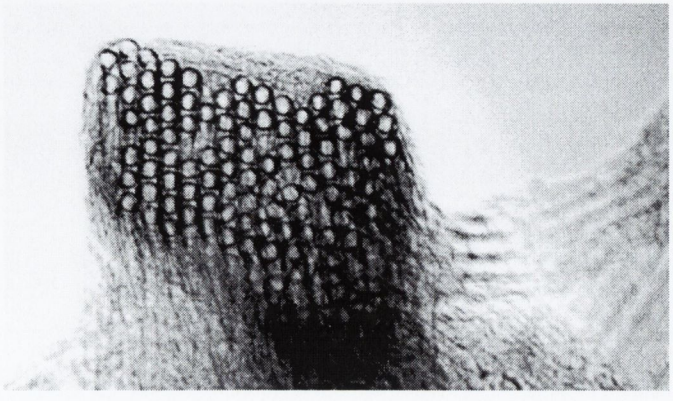

Figure 2.18 Singlewalled Carbon Nanotube bundle[16]

SWNT do not readily exist as isolated entities but tend to form intertwined ropes and bundles[16] as depicted in figure 2.18. These bundles consist of SWNT packed in a triagonal lattice held together by van der Waals forces[17]. Furthermore nanotubes are rarely free from defects. Inhomogeneties such as pentagons, heptagons or sp^3-hybridised carbon in the lattice are located mainly in the caps.

Multiwalled Nanotubes

Multiwalled carbon nanotubes (MWNT) consist of many concentric singlewalled cylinders. The interactions between these can greatly complicate their electronic structure. The density of states for a MWNT is far more complicated than for SWNT, however the outer shell is thought to dominate the electronic structure, since this is the shell, which interacts most with the external environment[18].

2.4 Multiphoton Processes and Nonlinear Phenomena

Nonlinear optical phenomena occur as a result of multiphoton processes in a material medium. Under an intense light field, the optical response of a material is driven beyond the familiar linear regime into the regime of nonlinear optics giving rise to new optical phenomena. The generation of these nonlinear optical phenomena can be described by considering the effect of incident light on the dipole moment of a material. The influence of an electromagnetic field on matter is manifested as an induced polarisation in the material. The polarisation characterises how the electric dipoles of the medium responds when illuminated by the oscillating electric field. In linear optics, the dipoles generally oscillate at the same frequency as the applied field in what can be classified as harmonic behaviour. However, this low intensity approximation, is only valid when the electric field does not cause an appreciably large oscillation in the electric dipoles. If the intensity of light is increased, the electronic dipoles can become hyperpolarized and multiphoton interactions can take place. Consequently, radiation can occur at frequencies, which are higher harmonics of the fundamental incident frequency. This anharmonic response of materials at high incident optical intensities can be identified with observable physical phenomena. For example, dipole oscillations at higher harmonics correspond to the nonlinear optical process of harmonic generation where

two photons are combined to produce one photon, whose energy is the sum of the two incident photons.

The optical response of a material can be presented more formally by defining the polarisation vector P. Under low irradiation intensity, this polarisation, is linearly dependent on the electric field strength, E and has the form

$$P = P_0 + \varepsilon_0 \chi^{(1)} E \tag{2.1}$$

where, P_0 is the initial polarisation, ε_0 is the permitivity of free space and $\chi^{(1)}$ denotes the linear optical susceptibility of the material. $\chi^{(1)}(-\omega;\omega)$ is a second rank tensor and describes the linear optical properties of a material such as absorption, emission, refraction and reflection. Such optical phenomena constitute the field of linear optics and are characterised by an induced response that is always linearly proportional to the incident field intensity.

In the case of high incident irradiation, the linear approximation no longer holds and a series expansion is required to express the induced polarisation response

$$P = P_0 + \varepsilon_0 (\chi^{(1)} E + \chi^{(2)} E^2 + \chi^{(3)} E^3 + ...) \tag{2.2}$$

$\chi^{(m)}$, denote the m^{th} order optical susceptibilities. Expressions with $m > 1$ constitute the nonlinear optical regime and signify that multiphoton interactions are involved. The induced response is characterised by its variation with some power of the incident field intensity.

The symmetry relationship P(E)=P(-E) means that even order susceptibilities do not feature in materials with centrosymmetry as is the case for the materials studied here. The third order susceptibility, $\chi^{(3)}$, is the next highest term and has no symmetry restrictions. It involves the interaction of three photons to produce a fourth and is of interest since it is responsible for several important phenomena including Self Phase Modulation (SPM), Phase Conjugation, Two Photon Absorption and Self Focusing and Defocusing. The implications of $\chi^{(3)}$, can be illustrated by considering the third-order contribution to the nonlinear polarisation

$$P^{(3)} = \varepsilon_0 \chi^{(3)} E^3 \tag{2.3}$$

Considering the simple case where the applied field is monochromatic given by

$$E = \mathrm{E}\cos(\omega \cdot t) \tag{2.4}$$

Then, since $\cos 3\omega t = 1/4\cos 3\omega t + 3/4\cos\omega t$, the nonlinear polarisation can be expressed as

$$P^{(3)} = \tfrac{1}{4}\varepsilon_0 \chi^{(3)} E^3 \cos(3 \cdot \omega t) + \tfrac{3}{4}\chi^{(3)}\varepsilon_0 E^3 \cos(\omega t) \tag{2.5}$$

The first term in equation (2.5) describes a response at frequency 3ω which is the process of third harmonic generation. This corresponds to the annihilation of three photons of frequency ω and the creation one photon of frequency 3ω and is represented symbolically as $\chi^{(3)}(-3\omega;\omega,\omega,\omega)$.

The second term in equation (2.5) describes a nonlinear contribution to the polarisation at the frequency of the incident field and hence corresponds to a nonlinear contribution to the refractive index of the medium. The refractive index, which in linear regime is defined as $n_0^2 = 1 + \chi^{(1)}$, becomes

$$n^2 = 1 + \chi^{(1)} + \chi^{(3)} E \cdot E \tag{2.6}$$

upon the incorporation of the third order contribution. The intensity dependent refractive index is represented as $\chi^{(3)}(-\omega;\omega,\omega,-\omega)$.

Applying a more general optical wave than that given by equation (2.4) gives rise to many more nonlinear optical phenomena. The different frequency combinations involved in these processes can be described symbolically; four wave mixing $\chi^{(3)}(-\omega_4;\omega_1,\omega_2,\omega_3)$, two photon absorption $\chi^{(3)}(-\omega_1;\omega_2,\omega_2,\omega_1)$.

The nonlinear optical processes described so far are examples of parametric processes, which implies that the initial and final quantum mechanical states involved in the multiphoton interactions are the same and photon energy is conserved. In these processes, the electronic population can be removed from the ground state for only a brief interval as permitted by the uncertainty principle. The temporary levels that the electrons reside in during these processes are known as virtual levels, which do not in effect correspond with real levels in the system.

Parametric processes occur at off resonance excitation wavelengths and are coherent since they maintain a well-defined phase relationship with the incident optical field. They have the fastest response time of all multiphoton processes and are desirable for ultrafast nonlinear optical switching.

Parametric processes are described by the real part of the optical susceptibility, while the imaginary part of the susceptibility implies damping of the optical wave in the medium resulting from the exchange of energy between the optical field and the nonlinear medium. These non-parametric processes occur under resonant conditions and involve the redistribution of electrons among the electronic states. A resonance contribution serves to enhance the nonlinearity by several orders of magnitude. However, response times are slower and absorption losses are involved as well as a loss of coherence between absorbed energy and the exciting fields.

The following sections present multiphoton induced nonlinear optical phenomena, which are of relevance to this work.

2.4.1 Nonlinear Refraction

A nonlinear refractive index is responsible for many important physical processes. Issues such as the development of an all optical switch, leading to the prospect of replacing conventional electronics with all optical systems, is based on this nonlinear optical phenomenon. $\chi^{(3)}$, allows for the possibility of a nonlinear refractive index change at the incident wavelength. This is seen in equation (2.6), which may be rewritten in the form

$$n = n_0 + n_2 I \,. \tag{2.7}$$

The process of self-focusing, is derived from the nonlinear response of the refractive index in the medium. This is the mechanism of z-scan technique which is used here to measure the nonlinear refractive index of the sample materials. Self-focusing can occur when an optical beam with a non-uniform intensity distribution, such a gaussian shaped laser beam, propagates through a material. If n_2 is positive, its intensity dependence will cause the refractive index of the material to be largest at the centre of the beam. The material then effectively acts as a positive lens, which

causes the rays to curve towards each other into a focus. This phenomenon is the basis of the Z-scan experiment, which is detailed in Chapter 4.

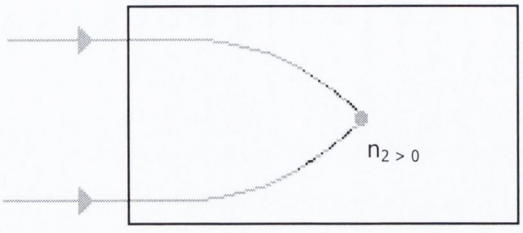

Figure 2.18 Self-focusing of light

The nonlinear refractive index is related to the real part of the third order susceptibility by

$$n_2 = \frac{3\Re e\chi^{(3)}}{4\varepsilon_0 c n_0^2} \tag{2.8}$$

Measurements of these parameters can be used to characterise the third order nonlinearity on the medium as described in chapter 4.

2.4.2 Nonlinear Absorption

The imaginary part of the third order optical susceptibility involves the modification of the absorption coefficient of a material. The absorption coefficient is then a function of the optical field intensity, and can be written in a form similar to that of the refractive index

$$\alpha = \alpha_0 + \beta I \tag{2.9}$$

where β is the nonlinear absorption coefficient and can be either positive or negative. Absorption can therefore either increase or decrease at high incident intensities depending on the sign of the nonlinear absorption coefficient.

The case where β is negative is known as saturable absorption which corresponds to a decrease in the absorption coefficient of a material under high intensity irradiation. Materials possessing strong electronic absorptions can behave as saturable absorbers

as long as the rate of populating the excited state exceeds the rate of return to the ground state. As the excited states are populated, there is a corresponding depletion in the ground-state population leading to a decrease in the ground state absorption coefficient. Consequently, the absorption saturates at high intensities and the medium can even bleach.

The opposite of saturable absorption is reverse saturable absorption, where the transmission as opposed to the absorption decreases with increasing intensity. This occurs when the excited state absorption cross section is greater than that of the ground state. One potential application for this type of effect is sensor protection where the amount of light that can be passed through the protecting medium is limited[19]. This process, known as optical limiting, can be used to protect sensitive optics from becoming exposed to light intensities which would otherwise cause damage. Chapter 5 presents the optical limiting effect of the materials used here.

Multiphoton absorption involving the simultaneous absorption of a number photons is another process which can occur when β is positive.

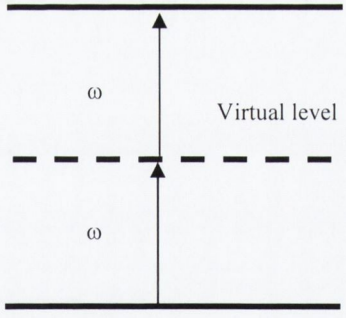

Figure 2.19 Two photon absorption

In this process an electron can be promoted to an excited state by the direct absorption of more than one photon in the manner indicated in figure 2.19. The selection rules for these processes differ from those which apply to familiar one-photon absorption. Multiphoton absorption is thus a useful tool in identifying states, which would not otherwise be detected in a linear absorption spectrum.

The nonlinear absorption coefficient is related to the imaginary part of the third order optical susceptibility by

$$\beta = \frac{3\Im m\chi^{(3)}}{2\varepsilon_0 c^2 n_0^2} \tag{2.10}$$

This parameter can also be used to characterise the third order nonlinearity on the medium as detailed later in section 4.3

2.4.3 Theory of Third Order Nonlinear Optics

The laws of quantum mechanics are used here to derive expressions for the third order optical susceptibility using the method described in Boyd[20]. These expressions are useful as they show explicitly how the material susceptibility depends on parameters such as dipole moment transitions and atomic energy levels. An abbreviated density matrix formulation is presented, since the full derivation of the expression for $\chi^{(3)}$ is unnecessarily complicated to present in complete detail.

To begin with, consider the density matrix ρnm, which represents a statistical description of the system where n and m run over the eigenstates of the system. The density matrix equation of motion describes how the density matrix evolves with time and is given by

$$\dot{\rho}_{nm} = \frac{-i}{\hbar}[\hat{H}, \hat{\rho}]_{nm} - \gamma_{nm}(\rho_{nm} - \rho_{nm}^{eq}) \tag{2.11}$$

where $\hat{H}$ is the Hamiltonian operator of the system and the brackets denote the usual commutator relationship. The second term on the right-hand side is a phenomenological damping term, which indicates that ρnm relaxes to its equilibrium value ρ_{nm}^{eq} at a rate γ_{nm}. A perturbative technique is used to solve the equation using a Hamiltonian in the form of $\hat{H} = \hat{H}_0 + \hat{V}(t)$. The Hamiltonian of a free atom is represented by $\hat{H}_0$ and $\hat{V}(t)$ represents the energy of interaction of the atom with the externally applied field. The electric dipole moment approximation $\hat{V}(t)$, given as

$$\hat{V}(t) = -\hat{\mu} \cdot \tilde{E}(t) \tag{2.12}$$

where $\hat{\mu} = -e\hat{r}$ denotes the electric dipole moment operator of the atom, is used. Expansion of the commutators and manipulation of the equations enables the density matrix equation of motion to be rewritten in the form

$$\dot{\rho}_{nm} = -i\omega_{nm}\rho_{nm} - \frac{i}{\hbar}\sum(V_{nv}\rho_{vm} - \rho_{nv}V_{vm}) - \gamma_{nm}(\rho_{nm} - \rho_{nm}^{eq}) \tag{2.13}$$

where $\omega_{nm} = \frac{E_n - E_m}{\hbar}$ is the transition frequency.

The perturbation is now expanded, by replacing $\hat{V}_{ij}$ in equation (2.13) by $\lambda\hat{V}_{ij}$ where λ is a parameter ranging between zero and one which characterises the strength of the perturbation.

Solutions to equation (2.13) in the form of a power series in λ, such that the coefficients of each power of λ satisfy equation (2.13) separately, give rise to the following relation

$$\rho_{nm} = \rho_{nm}^{(0)} + \lambda\rho_{nm}^{(1)} + \lambda^2\rho_{nm}^{(2)} + \ldots \tag{2.14}$$

A system of equations is obtained containing only linear homogenous terms and inhomogeneous terms that are already known. By employing a steady state solution for $\rho_{nm}^{(0)}$ and making a change of variables, the resultant $\rho_{nm}^{(i)}$ system of equations can be integrated. The perturbation expansion giving the third-order correction to the density matrix is given by

$$\rho_{nm}^{(3)} = e^{-(i\omega_{nm}+\gamma_{nm})t}\int_{-\infty}\frac{-i}{\hbar}[\hat{V},\hat{\rho}^{(2)}]_{nm}e^{(i\omega_{nm}+\gamma_{nm})t'}dt' \tag{2.15}$$

From the general result for the second order correction to $\hat{\rho}$, expressions for $\rho_{vm}^{(2)}$ and $\rho_{nv}^{(2)}$ are available from

$$\rho_{nm}^{(2)} = \sum_{v}\sum_{pq}\times\left\{\frac{\rho_{mm}^{(0)} - \rho_{vv}^{(0)}}{\hbar^2}\frac{[\mu_{nv}\cdot E(\omega_q)][\mu_{vm}\cdot E(\omega_p)]}{[(\omega_{nm} - \omega_p - \omega_q) - i\gamma_{nm}][(\omega_{vm} - \omega_p) - i\gamma_{vm}]}\right.$$

$$\left. - \frac{\rho_{vv}^{(0)} - \rho_{nn}^{(0)}}{\hbar^2}\frac{[\mu_{nv}\cdot E(\omega_q)][\mu_{vm}\cdot E(\omega_p)]}{[(\omega_{nm} - \omega_p - \omega_q) - i\gamma_{nm}][(\omega_{nv} - \omega_p) - i\gamma_{nv}]}\right\}\times e^{-i(\omega_p+\omega_q)t}$$

$$\equiv \sum_{v}\sum_{pq} K_{nmv} e^{-i(\omega_p+\omega_q)t} \tag{2.16}$$

where the applied field has been expressed as $\tilde{E}(t) = \sum E(\omega_p)e^{-i\omega_p t}$ and p and q are dummy indices. On changing the dummy indices and expanding the commutator $[\hat{V}, \hat{\rho}^{(2)}]_{nm}$ the integration of equation (2.15) can be performed.

$$\rho_{nm}^{(3)} = \frac{1}{\hbar}\sum_{vl}\sum_{pqr}\left\{\frac{[\mu_{nv}\cdot E(\omega_r)]K_{vml}}{(\omega_{nm}-\omega_p-\omega_q-\omega_r)-i\gamma_{nm}} \frac{[\mu_{vm}\cdot E(\omega_r)]K_{nvl}}{(\omega_{nm}-\omega_p-\omega_q-\omega_r)-i\gamma_{nm}}\right\} e^{-i(\omega_p+\omega_q+\omega_r)t} \tag{2.17}$$

The nonlinear polarisation at frequency $\omega_p+\omega_q+\omega_r$ is given by

$$P(\omega_p+\omega_q+\omega_r) = N\left\langle \mu(\omega_p+\omega_q+\omega_r)\right\rangle \tag{2.18}$$

where $\langle\tilde{\mu}\rangle = \sum \rho_{nm}\mu_{nm} \equiv \sum\langle\mu(\omega_s)\rangle e^{-i\omega_s t}$.

Expressing the nonlinear polarisation in terms of the third-order susceptibility

$$P_k(\omega_p+\omega_q+\omega_r) = \sum_{hij}\sum_{(pqr)}\chi^{(3)}(\omega_p+\omega_q+\omega_r,\omega_r,\omega_q,\omega_p)\times E_j(\omega_r)E_i(\omega_q)E_h(\omega_p) \tag{2.19}$$

Combining these equations gives the third order susceptibility as

$$\chi_{kjih}^{(3)}(\omega_p+\omega_q+\omega_r,\omega_r,\omega_q,\omega_p) = \frac{N}{\hbar^3}\zeta_1 \times \sum_{nmvl}\left\{(\rho_{mm}^{(0)}-\rho_{ll}^{(0)})\right.$$

$$\times\frac{\mu_{mn}^k\mu_{nv}^j\mu_{vl}^i\mu_{lm}^h}{[(\omega_{nm}-\omega_p-\omega_q-\omega_r)-i\gamma_{nm}][(\omega_{vm}-\omega_p-\omega_q)-i\gamma_{vm}][(\omega_{lm}-\omega_p)-i\gamma_{lm}]} - (\rho_{ll}^{(0)}-\rho_{vv}^{(0)})$$

$$\times\frac{\mu_{mn}^k\mu_{nv}^j\mu_{lm}^i\mu_{vl}^h}{[(\omega_{nm}-\omega_p-\omega_q-\omega_r)-i\gamma_{nm}][(\omega_{vm}-\omega_p-\omega_q)-i\gamma_{vm}][(\omega_{vl}-\omega_p)-i\gamma_{vl}]} - (\rho_{vv}^{(0)}-\rho_{ll}^{(0)})$$

$$\times\frac{\mu_{mn}^k\mu_{vm}^j\mu_{nl}^i\mu_{lv}^h}{[(\omega_{nm}-\omega_p-\omega_q-\omega_r)-i\gamma_{nm}][(\omega_{nv}-\omega_p-\omega_q)-i\gamma_{nv}][(\omega_{lv}-\omega_p)-i\gamma_{lv}]} + (\rho_{ll}^{(0)}-\rho_{nn}^{(0)})$$

$$\left.\times\frac{\mu_{mn}^k\mu_{vm}^j\mu_{lv}^i\mu_{nl}^h}{[(\omega_{nm}-\omega_p-\omega_q-\omega_r)-i\gamma_{nm}][(\omega_{nm}-\omega_p-\omega_q)-i\gamma_{nv}][(\omega_{nl}-\omega_p)-i\gamma_{nl}]}\right\} \tag{2.20}$$

The permutation operator ζ_1 means that everything to the right of it is to be averaged over all possible permutations of the input frequencies ω_p, ω_q and ω_r, with the Cartesian indices h,i,j permuted simultaneously.

The equation can be rewritten as eight separate terms by changing the dummy indices so that l is always the index of $\rho_{ll}^{(0)}$. It is also required that only positive frequencies appear if the energies are ordered so that $E_v > E_n > E_m > E_l$, and that the matrix elements are arranged so that they appear in a "natural order", $l \to m \to n \to v$. This gives the third order susceptibility in the form

$$\chi_{kjih}^{(3)}(\omega_p + \omega_q + \omega_r, \omega_r, \omega_q, \omega_p) = \frac{N}{\hbar^3}\zeta_1 \times \sum_{vnml} \rho_{ll}^{(0)}$$

$$\times \left\{ \frac{\mu_{lv}^k \mu_{vn}^j \mu_{nm}^i \mu_{ml}^h}{[(\omega_{vl} - \omega_p - \omega_q - \omega_r) - i\gamma_{vl}][(\omega_{nl} - \omega_p - \omega_q) - i\gamma_{nl}][(\omega_{ml} - \omega_p) - i\gamma_{ml}]} \right. \quad (a_1)$$

$$+ \frac{\mu_{lv}^k \mu_{vn}^j \mu_{nm}^i \mu_{ml}^h}{[(\omega_{nv} - \omega_p - \omega_q - \omega_r) - i\gamma_{nv}][(\omega_{mv} - \omega_p - \omega_q) - i\gamma_{mv}][(\omega_{vl} + \omega_p) + i\gamma_{vl}]} \quad (a_2)$$

$$+ \frac{\mu_{lv}^k \mu_{vn}^j \mu_{nm}^i \mu_{ml}^h}{[(\omega_{nv} - \omega_p - \omega_q - \omega_r) - i\gamma_{nv}][(\omega_{vm} + \omega_p + \omega_q) + i\gamma_{vm}][(\omega_{ml} - \omega_p) - i\gamma_{ml}]} \quad (b_1)$$

$$+ \frac{\mu_{lv}^k \mu_{vn}^j \mu_{nm}^i \mu_{ml}^h}{[(\omega_{mv} - \omega_p - \omega_q - \omega_r) - i\gamma_{mn}][(\omega_{nl} + \omega_p + \omega_q) + i\gamma_{nl}][(\omega_{vl} + \omega_p) + i\gamma_{vl}]} \quad (b_2)$$

$$+ \frac{\mu_{lv}^k \mu_{vn}^j \mu_{nm}^i \mu_{ml}^h}{[(\omega_{vn} + \omega_p + \omega_q + \omega_r) + i\gamma_{vn}][(\omega_{nl} - \omega_p - \omega_q) - i\gamma_{nl}][(\omega_{ml} - \omega_p) - i\gamma_{ml}]} \quad (c_1)$$

$$+ \frac{\mu_{lv}^k \mu_{vn}^j \mu_{nm}^i \mu_{ml}^h}{[(\omega_{nm} + \omega_p + \omega_q + \omega_r) + i\gamma_{nm}][(\omega_{mv} - \omega_p - \omega_q) - i\gamma_{mv}][(\omega_{lv} + \omega_p) + i\gamma_{vl}]} \quad (c_2)$$

$$+ \frac{\mu_{lv}^k \mu_{vn}^j \mu_{nm}^i \mu_{ml}^h}{[(\omega_{nm} + \omega_p + \omega_q + \omega_r) + i\gamma_{nm}][(\omega_{vm} + \omega_p + \omega_q) + i\gamma_{vm}][(\omega_{ml} - \omega_p) - i\gamma_{ml}]} \quad (d_1)$$

$$\left. + \frac{\mu_{lv}^k \mu_{vn}^j \mu_{nm}^i \mu_{ml}^h}{[(\omega_{ml} + \omega_p + \omega_q + \omega_r) + i\gamma_{ml}][(\omega_{nl} + \omega_p + \omega_q) + i\gamma_{nl}][(\omega_{vl} + \omega_p) + i\gamma_{vl}]} \right\} \quad (d_2) \qquad (2.21)$$

For the general case in which ω_p, ω_q and ω_r are distinct, six permutations of the field frequencies occur, and hence the expression for $\chi^{(3)}$ consists of 48 different terms once the permutation operator is expanded. The resonance structure of this

expression can be illustrated in terms of the energy level diagrams shown in figure 2.20.

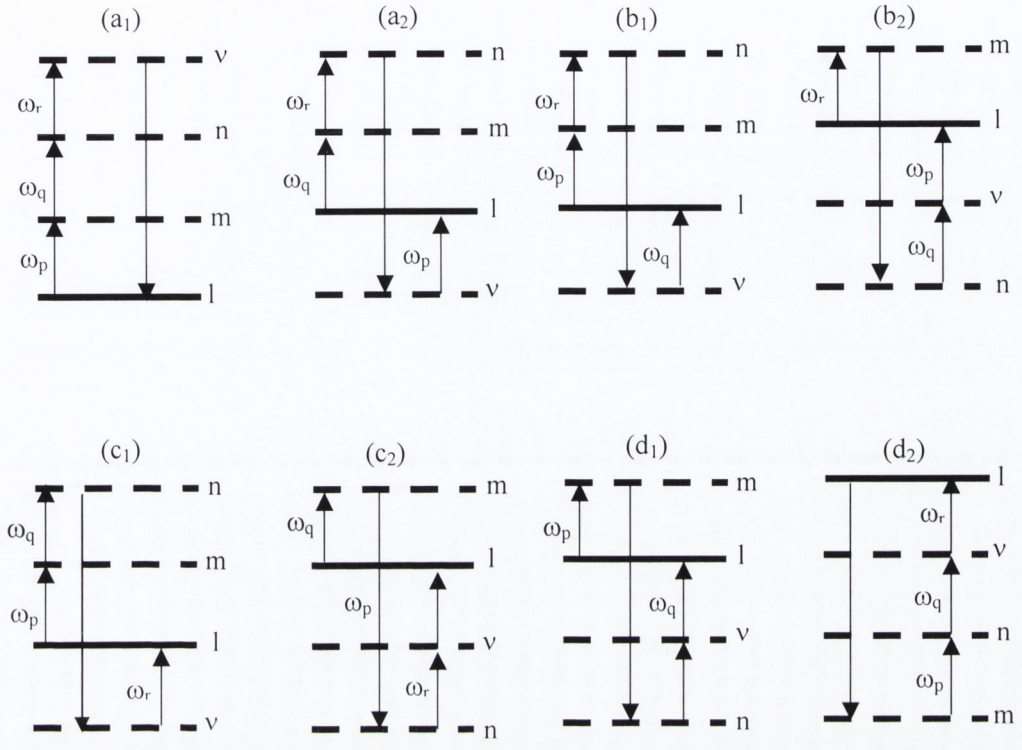

Figure 2.20 Resonance structure of the third order nonlinear optical susceptibility[20]

The energy level diagrams illustrated in figure 2.20 give a pictorial description of the various multiphoton transitions which can be involved in $\chi^{(3)}$ processes. They show the photon routes, and depict the different energy levels with which they interact denoting whether the interaction is virtual or real. This representation is useful as a means of reference and aids in the understanding and interpretation of the fundamentals of the nonlinear optical response of a material.

However some caution is necessary. Although the origin of material nonlinearities can be well described by time-independent and time-dependent perturbation theory, this is only strictly true in the off resonance regime. The materials examined here were generally measured in the on resonance regime and hence direct relation of their response using the theoretical treatment described here is not completely valid. Indeed a satisfactory theoretical treatment of the on resonance nonlinear optical response of a material is not as yet available. Albeit theoretical modelling of

nonlinear response of the materials is outside the scope of this thesis, nevertheless exploring the primary theoretical origin of nonlinear processes is worthwhile. The diagrammatic representation given in figure 2.20 illustrates possible states, types of transitions and the various interactions that are involved in the generation of third order nonlinear phenomena.

2.5 Organic Materials as Targets for Nonlinear Optics

Organic materials emerged in the late 1970s as a possible alternative to semiconductors and glasses for integrated photonic switching[21]. The merits of organic materials include a high capacity for multiphoton interactions and hence a large nonlinear optical response, an ultra fast nonlinear response, high optical damage thresholds, architectural flexibility and ease of fabrication[22]. Progress in the performance of organic materials lies in the design of new materials. A series of latest candidate organic materials for photonic applications are presented.

Phthalocyanines are among the most versatile of organic materials for nonlinear optics[2]. Their highly conjugated macrocycle is a structure known to give large optical nonlinearities. Their immense flexibility allows the manipulation of $\chi^{(3)}$ by chemical substitution and provides the possibility of tailoring the speed and magnitude of the multiphoton interactions to a target application. A metal atom adds low lying electronic states to a molecule and introduces new states into the absorption spectrum. These can contribute to the nonlinear response, either directly or via new resonance enhancements. The introduction of axial substitution, which can be carefully adjusted chemically, provides for the possibility of controlling the nonlinear optical response in these molecules

The endohedral metallofullerene La@C_{82} provides an exceptional molecular species for nonlinear optical investigations. It incorporates the particular attributes of the fullerene molecules and the added advantage of charge transfer effects provided by the encapsulated metal atom. An increase in nonlinear optical response with increasing fullerene size has been shown experimentally[23]. Also investigations on C_{60} have shown that chemical modifications to form charge transfer complexes can

increase the nonlinear optical response by up to two orders of magnitude[24]. La@C_{82} incorporates both these features and hence is a promising material.

Carbon nanotubes possess perhaps the most remarkable attributes for nonlinear optics. Considering the trend of increased nonlinear responses for higher fullerenes[25,26] carbon nanotubes take this advantage to the limit given that they are among the longest conjugated systems known. They therefore posses very extensive π-electron systems. In addition, the π-electrons are confined to one dimension, which is favourable for the production of a large nonlinear optical response. The presence of van Hove singularities in the DOS can be expected to greatly enhance resonant nonlinear optical transitions.

2.6 Conclusions

This chapter introduced the concept of organic materials for photonic applications. The background theory of organic materials and multiphoton processes responsible for nonlinear optical phenomena was presented. The general concepts of organic materials were applied to the materials used in this work; phthalocyanines, fullerenes and carbon nanotubes. The individual features of the materials were explained in view of how they can relate to their nonlinear optical properties. The evolution of the material properties with the dimension and topology of their structures provides further interest. The overall profile is of a progressive class of materials incorporating a range of supplementary mechanisms, which should greatly influence their capacity for multiphoton interactions and therefore their nonlinear optical performance.

References

1 N.B McKeown, *Phthalocyanine Materials, Synthesis, Structure and Function*. Cambridge University Press, 1998.

2 H.S. Nalwa and J.S. Shirk, *Phthalocyanines, Properties and Applications*. New York, 1996.

3 M. S. Dresselhaus and G. Dresselhaus, *Fullerenes and Carbon Nanotubes*.

4 R. Knupfer, Surface Science Reports **42** *1-2*, 1 (2001).

5 H.E. Kroto, J.R. Heath, S.C. O'Brien, R.F. Curl, and R.E. Smalley, Nature **318** *162* (1985).

6 M. S. Dresselhaus, G. Dresselhaus, A. M. Rao, and P. C. Eklund, Synthetic Metals **78** *3*, 313 (1996).

7 H. W. Kroto, Nature, (London), **329**, 529 (1987)

8 S. Nagase and K. Kobayashi, **228**, 106 (1994).

9 S. P. Solodovnikov, B. L. Tumanskii, V. V. Bashilov, V. I. Sokolov, S. Lebedkin, and W. Kratschmer, Fullerene Science and Technology **8** *1-2*, 1 (2000).

10 E. Nishibori, M. Sakata, M. Takata, M. Hasegawa, and H. Shinohara, Chem. Phys. Lett. **199,** (1996).

11 H. Shinohara, H. Sato, Y. Sato, M. Ohkohchi, and Y. Ando, J. Phys. Chem **96** *357* (1992).

12 S. Hino, H. Takahashi, K. Iwasaki, T. Miyamae, S. Hasegawa, K. Kikuchi, and Y. Achiba, Phys. Rev. Lett **71** *4261* (1993).

13 R. Saito, M. Fujita, G. Dresselhaus, and M. S. Dresselhaus, Applied Physics Letters **60** *18*, 2204 (1992).

14 M.S. Dresselhaus, G. Dresselhaus, and R. Saito, Solid State Commun. **84** *201* (1992).

15 A. M. Rao, E. Richter, S. Bandow, B. Chase, P. C. Eklund, K. A. Williams, S. Fang, K. R. Subbaswamy, M. Menon, A. Thess, R. E. Smalley, G. Dresselhaus, and M. S. Dresselhaus, Science **275** *5297*, 187 (1997).

16 A. Thess, R. Lee, P. Nikolaev, H. J. Dai, P. Petit, J. Robert, C. H. Xu, Y. H. Lee, S. G. Kim, A. G. Rinzler, D. T. Colbert, G. E. Scuseria, D. Tomanek, J. E. Fischer, and R. E. Smalley, Science **273** *5274*, 483 (1996).

17 H. Stahl, J. Appenzeller, R. Martel, P. Avouris, and B. Lengeler, Physical Review Letters **85** *24*, 5186 (2000).

[18] J. N. Coleman, Material Ireland Polymer Research Centre, Physics Department Trintiy College Dublin, Dublin 2, Ireland. Private communication.

[19] L. W. Tutt and T. F. Boggess, Progress in Quantum Electronics **17** *4*, 299 (1993).

[20] R.W. Boyd, *Nonlinear Optics*. Academic Press, Boston, 1992.

[21] C. Sauteret, J.P. Hermann, K. Frey, J. Ducuing, R.K. Chance, and R.H. Baughmann, Phys. Rev. Lett **36** *956* (1976).

[22] H.S Nalwa, Adv. Mater. **5** *341* (1993).

[23] H. J. Huang, G. Gu, S. H. Yang, J. S. Fu, P. Yu, G. K. L. Wong, and Y. W. Du, Journal of Physical Chemistry B **102** *1*, 61 (1998).

[24] J. Li, S. Wang, Hong Yang, Q. H. Gong, X. An, H. Chen, and D. Qiang, Chem. Phys Lett. **288** *175* (1988).

[25] S.R. Flom, R.G.S. Pong, F.J. Bartoli, and Z.H. Kafafi, Phys. Rev. B. **46** *15598* (1992).

[26] N. Matsuzawa and A.D. Dixon, J. Phys. Chem **96** *6241* (1992).

Chapter 3
Characterisation of Material Properties

The basic properties of materials including their physical and chemical structure, and most importantly their linear optical properties, have a profound influence on their nonlinear optical response. The behaviour of these material functions can serve to either greatly enhance or diminish the efficiency of their multiphoton interactions and hence their nonlinear optical response. Studies of the basic material properties can be conducted to in order develop a basic understanding and to build a profile of the material. This information can be used to give an insight into issues such as which spectral regions the material is likely to support nonlinear optical activity, whether the nonlinear response is likely to involve an absorptive response or just a purely parametric response. From this analysis, it is possible to forecast certain aspects of the nonlinear optical behaviour of a material.

The task of material characterisation involves using well-established techniques to determine properties such as the electronic and chemical structures and the material morphology. Two approaches are taken here; the first is to use spectroscopic techniques to measure parameters such as absorption, emission, and chemical bond vibrations. The second is to use microscopic techniques to directly image the material structure on the micrometer and nanometer scale.

3.1 Spectroscopic Techniques

Spectroscopy uses the interaction of radiation in a material to gather information on the electronic, molecular and physical structure of materials. Optical spectroscopies are used to gain understanding of materials from their interactions with photons

while vibrational spectroscopies give information concerning the interaction of phonons. When an optical wave interacts with a medium, the constituent atoms or molecules can react to the oscillating electric field in two different ways, depending on the incident frequency. If the photon energy matches that of an excited state, such as an electronic or vibrational state, a resonant interaction occurs and the molecule absorbs the photon. If the incident photon energy is nonresonant a scattering type interaction takes place.

3.1.1 Optical Spectroscopy

The two principal optical spectroscopic techniques used are the complementary techniques of absorption and fluorescence spectroscopy. These two techniques examine optical excitations and de-excitations of materials, and can give a great deal of information about the material and its local environment.

Absorption Spectroscopy

Absorption spectroscopy involves passing a monochromatic beam of light through a sample and measuring the absorption of the material at this wavelength. This absorption is measured as a function of wavelength over a range extending from the infrared to ultraviolet. The absorption is usually measured in reference to a blank sample in a double beam arrangement, to eliminate variations caused by the differences in lamp intensities at different frequencies. As the photons pass through a material, it is possible that photons of a suitable energy can interact with the material, resulting in an electron being excited to a higher energy state, and the photon being absorbed. By measuring the amount of light absorbed for a particular wavelength, it is possible to deduce information about the electronic structure of the material.

At room temperature molecules, which are in thermal equilibrium, generally reside in the lowest vibrational level of the ground state. The vast majority of the excitation transitions therefore occur from the S_{00} level in the ground state. Since excitation occurs from only one level in the ground state to the vibrational levels in the excited state, an absorption spectrum yields information on the vibrational energy distribution of the first excited state. The linear absorption spectrum of a

material hence yields information on the vibrational energy distribution of one photon excited states.

Fluorescence Spectroscopy

Fluorescence spectroscopy is a useful complementary technique to absorption spectroscopy. While absorption spectroscopy probes the energies of excitations to higher states, fluorescence spectroscopy probes the energies at which higher states relax radiatively back to the ground state. Usually a suitable fixed wavelength is used to excite the material, and the wavelength distribution of the emitted light is recorded

On excitation, an electron is promoted to a vibronic level of the first excited state, and subsequently falls rapidly through the vibrational manifold to the lowest energy level of that excited state. The emission then proceeds from the lowest vibrational level in the first excited state to the vibrational levels of the ground state. Since relaxation occurs from only one level in the excited state to the vibrational levels in the ground state, a fluorescence spectrum yields information on the vibrational energy level distribution of the ground state. Due to the thermal relaxation, which ensues after initial excitation, the molecule loses energy. This is manifested as a red shift in the emission spectrum compared to that of the absorption spectrum and is termed stokes shift

3.1.2 Vibrational Spectroscopy

The chemical bonds within a molecule and even the entire molecular structure itself oscillate and vibrate at frequencies in the infrared region. Measurement of these vibrational frequencies provides useful information on the molecular structure. Traditionally, two techniques are used to obtain a vibrational spectrum of a molecule; infrared spectroscopy and Raman spectroscopy.

Infrared Spectroscopy

Material absorption at energies in the infrared region corresponds to vibrations of the chemical bonds within the molecule. A range of molecular vibrations can occur, each of which oscillates at its own characteristic frequency. Absorption of infrared

radiation gives rise to transitions between these different vibrational states. Thus measuring the infrared absorption spectrum gives a series of absorptions corresponding to characteristic vibrations of particular bonds. Analysis of the location of the frequencies of these absorptions can aid in the identification of the material composition. In organic materials, the most common absorptions occur in the wavenumber range 4000 cm^{-1} – 650 cm^{-1}.

Raman Spectroscopy

Raman Spectroscopy also gives information about the vibrational frequencies of a material, and hence its structure. The oscillating electric field of an incident optical wave can induce an oscillating dipole moment in a material. The material then radiates at the same frequency as the incident field in familiar elastic scattering processes. However, if the oscillating electric field exchanges energy with the molecule, then the scattered radiation may have a higher or lower frequency than the incident electric field. This frequency difference corresponds to vibrational modes of the molecular structure and is referred to as Raman scattering. Inelastically scattered light is much weaker than elastically scattered light, and therefore a laser light source is used. Raman scattering measurements can identify characteristic vibrational modes in a material and so provide information on its structure.

3.1.3 Microscopy Techniques

Microscopy involves the direct imaging of samples. In the microscopy techniques employed here, electrons instead of photons are used to image samples as the shorter wavelength allows a much higher resolution than traditional optical microscopy

Transmission Electron Microscopy (TEM)

In TEM a beam of electrons is directed onto a sample. The incident electrons are absorbed or scattered at different rates depending on the local structure, giving rise to an image of the sample. The TEM used was a Hitachi H7000, and accelerating voltage of typically 100 keV was applied. The substrates consisted of copper grids, with holes 100 μm in size. These grids are covered in a thin layer of the electron transparent polymer, formvar. Samples were prepared by using a pipette to drop some of the solution onto the grids.

Scanning Electron Microscopy (SEM)

Scanning electron microscopy involves scanning an electron beam across the sample and line by line to build up an image of the sample.

3.2 Material Characterisation

The following is an account of the characterisation of the basic material properties. Techniques appropriate for the materials concerned are used. Spectroscopic measurements were carried out on all materials, while microscopy was only suited to the carbon nanotube samples due to their larger size.

3.2.1 Endohedral Metallofullerene La@C_{82}

The endohedral metallofullerene La@C_{82} samples were obtained from Lebedkin at the Max Planck Institute, Germany[1]. The samples were in solution with a concentration of 3×10^{-4} M in a solvent combination of 3:1 toluene:dichloromethane. The presence of the dichloromethane is as result of the chromatography used in the sample purification process and is not expected to have any significant influence on the properties investigated in this work. The colour of the La@C_{82} solution is a deep rusty brown which is typical of a larger fullerene species.

The linear absorption spectrum for La@C_{82} is shown in figure 3.1, and resembles that given in the literature[2]. Compared to C_{60} the absorption contains many new shoulders and is much broader extending out in to the near infrared region. These absorption changes result from two main factors; the reduced symmetry properties of the higher fullerenes and the presence of the metal. Symmetry reduction has the effect of relaxing the symmetry forbidden transitions and increasing the absorption in the visible region. The addition of the La metal and the consequential charge transfer to the fullerene cage produces absorption bands in the near infrared region. In particular, the presence of bands and a tail beyond 1000 nm is due to the presence of the La within the C_{82} cage. The La@C_{82} was found to be stable over a long period of time and the sample solution was of reasonably high spectroscopic quality with little residue forming in solution.

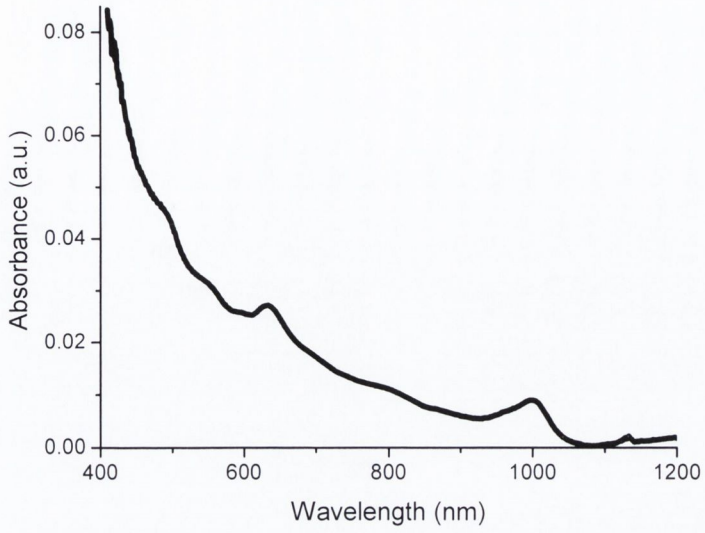

Figure 3.1 Linear absorption spectrum for metallofullerene endohedral La@C_{82}

Further characterisation was not carried out here, as a complete characterisation of La@C_{82} is available in the literature[3].

3.2.2 Axially Substituted Phthalocyanines

A set of axially substituted titanium(IV) phthalocyanines were obtained from Prof. Hanacks group in Teubingen[4]. Substitution was performed on the basic macrocycle (tert-butyl)$_4$PcTiO

Electron withdrawing substituents like cyano or aldehyde groups introduce a large dipole moment perpendicular to the macrocycle.

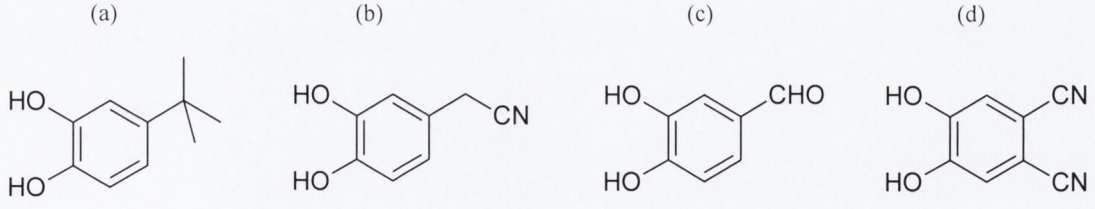

Figure 3.2 Axial ligands used for the substitution of (tert-butyl)$_4$PcTiO

Such large functionalised ligands, in particular those shown in figure 3.2 (a)-(d), introduce steric crowding helping to reduce the tendency of molecules to form

aggregates. Four axially substituted titanium phthalocyanines were produced using these ligands, labelled compound A-D as illustrated in figure 3.3.

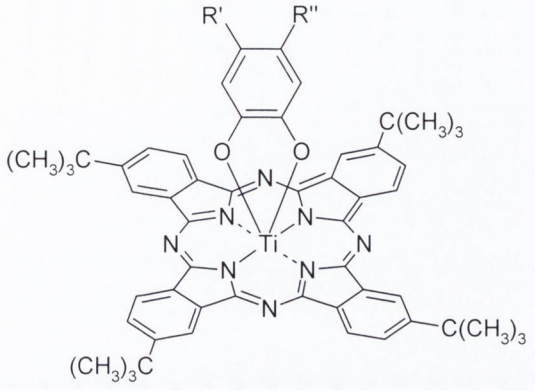

	R'	R''
A	H	CH_2CN
B	H	CHO
C	CN	CN
D	H	*tert.*-butyl

Figure 3.3 Structure of axially substituted titanium phthalocyanines

Optical absorption spectra of the freshly prepared samples show the typical absorption profile of a metallo phthalocyanine and are shown in figure 3.4.

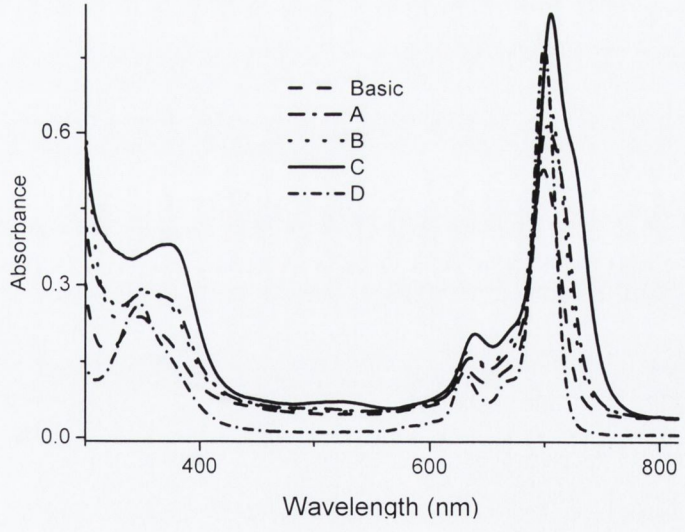

Figure 3.4 Linear absorption of unsubstituted & axially substituted Ti:phthalocyanines

The spectral absorption of the Q and B bands are shifted slightly in each case compared to the basic (tert-butyl)$_4$PcTiO

The influence of the axial groups is also seen in the formation of charge transfer bands in the optical window between the two main absorption bands. These are seen clearly in the absorption spectrum shown in figure 3.5.

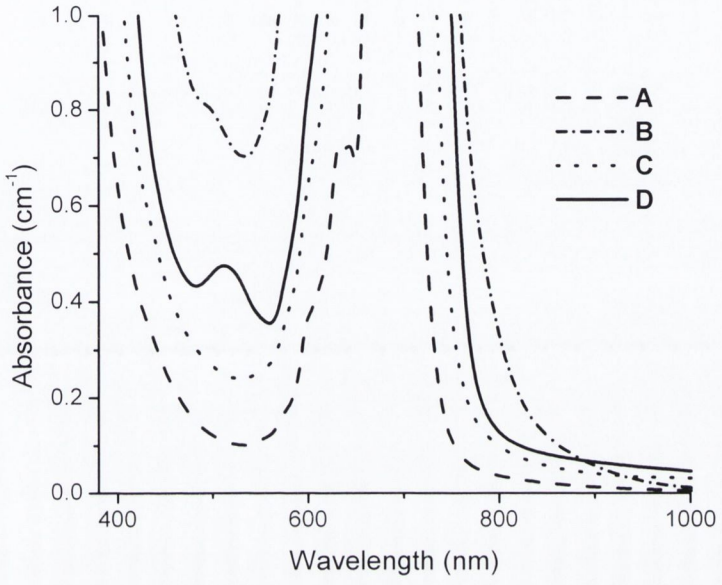

Figure 3.5 Window region absorption of axially substituted Ti:phthalocyanines which have been freshly prepared

However, these compounds were found to be relatively unstable in toluene solution as seen in the absorption spectra of aged sample shown in figure 3.6. Sample degradation occurred over a period of time with a residue forming in the bottom of the vessel. Absorption spectra for the aged sample, taken seven of days after sample preparation reveal a clear splitting of the Q-band absorption. This signifies the loss of the central titanium metal and therefore the axial substituents. The shelf life of these phthalocyanines is estimated to be about seven days.

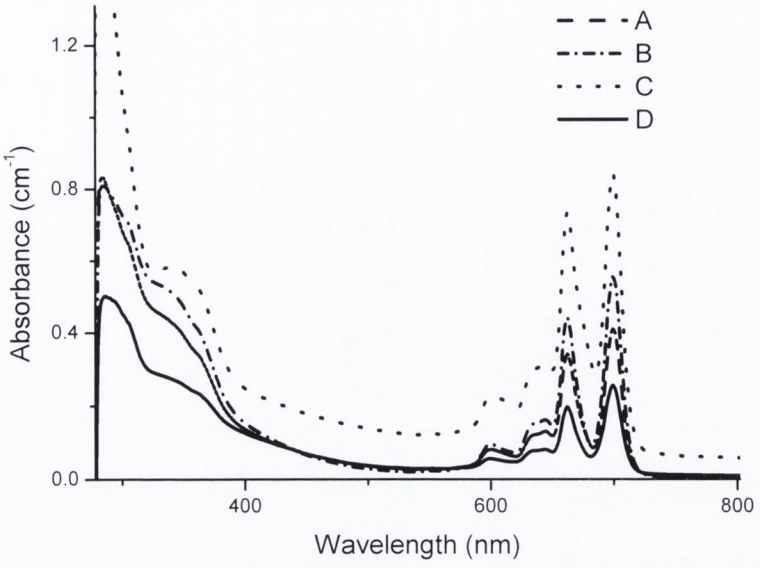

Figure 3.6 Absorption spectra of aged axially substituted Ti:phthalocyanines

As complete degradation was not immediate, nonlinear optical measurements on fresh solutions were carried out and useful information about these compounds could nevertheless be obtained.

3.2.3 Carbon Nanotubes

Both SWNT and MWNT are used in this work in addition to pure graphitic particles and residue particles from the carbon nanotube production process[5], which are used as reference materials. The reference materials served as a comparison material for the nanotubes properties as well as a method of verifying that behaviour observed in nanotubes originate from features of their unique structure.

Carbon Nanotube Samples

The nanotubes used in this work, both SWNT and MWNT were produced using the arc discharge method. Dr. Bernier's group in Montpellier[6] produced SWNT. SWNT require the presence of a metal catalyst for their synthesis. Using a Y/Ni mixture the Montpellier group achieved a SWNT yield in range 70-90 %. The average diameter was found to be 1.4 nm, and the nanotubes were arranged in crystalline bundles with a diameter in the range of 5 to 20 nm[7]. In a scanning electron microscope image, such as that shown on figure 3.7, the SWNT material produced by this method looks like a mat of carbon ropes.

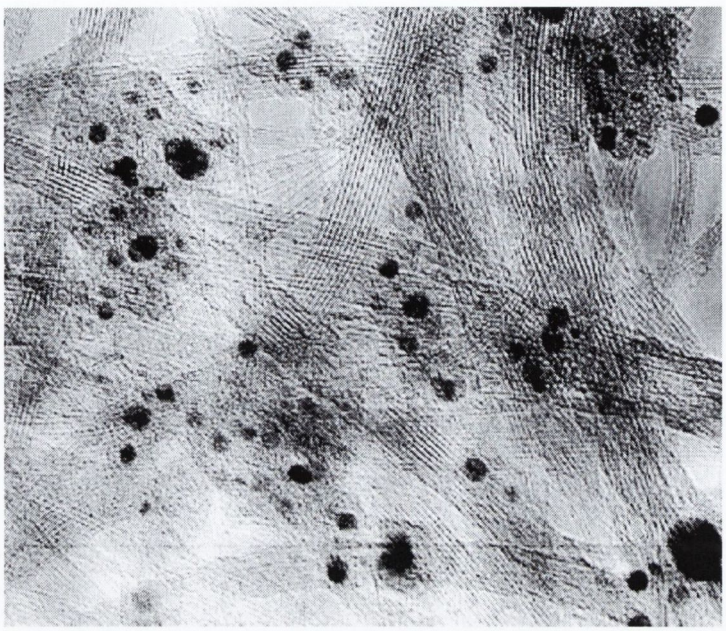

Figure 3.7 High-resolution micrograph of SWNT ropes produced by arc-discharge

Some carbonaceous impurities are present in addition to metal particles used as the catalyst for the SWNT production.

Multiwalled carbon nanotubes (MWNT) from two different sources were used in this study. The first sample, shown in the TEM micrograph in figure 3.8 was produced in Trinity ($MWNT_{Trinity}$) using a Krätschmer generator as described in previous works[8]. These MWNT samples have been well characterised and the raw nanotubes powder is known to contain between 30 % and 60 % of well graphitised nanotubes, the remainder being mainly graphitic impurities[9]. A large amount of nanotubes can be observed in TEM micrographs of the ($MWNT_{Trinity}$) samples along with much graphitic impurities which, accompany their production. The second MWNT sample was purchased from BuckyUSA[10] ($MWNT_{USA}$) and was estimated to contain 20-30 % nanotubes.

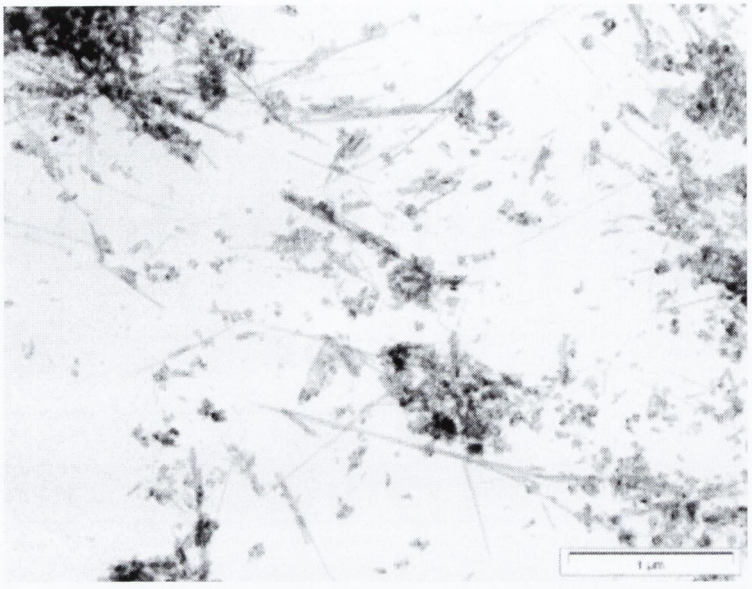

Figure 3.8 TEM of MWNT produced in Trinity College Dublin

A SEM micrograph of these MWNT is shown in figure 3.9.

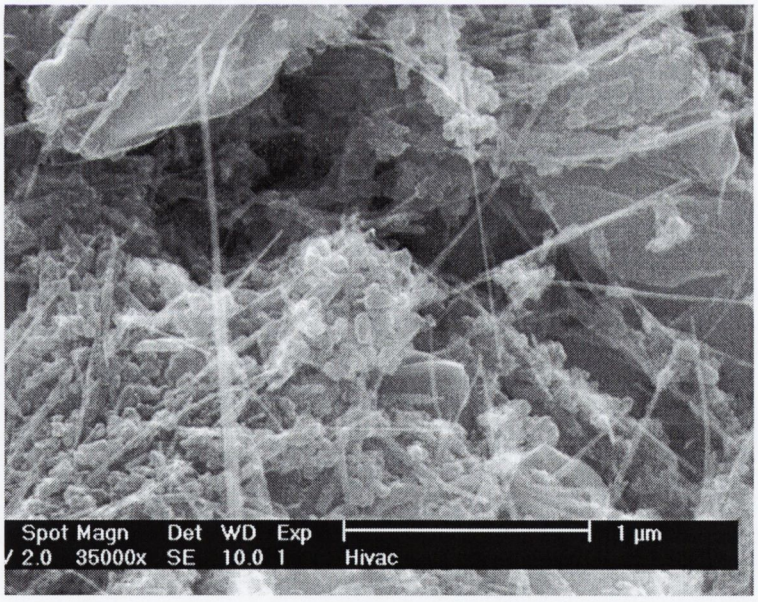

Figure 3.9 SEM of $MWNT_{USA}$

Similar to ($MWNT_{Trinity}$), large amount of nanotubes along with a lot of graphitic impurities can be observed in SEM pictures of the of the ($MWNT_{USA}$) samples.

Two graphitic particle (GP) samples were used. The first were graphite particles (GP), which were ground from 99.99 % pure graphite rod and the second sample was ground from the shell which surrounds the raw nanotubes when produced in the Krätschmer generator[11] (KGP). The GP samples contained pure graphite particles while the KGP contained many fullerene and carbon onion species, a small amount of carbon nanotubes and various turbostratic graphite particles. The TEM image in figure 3.10 shows the GP samples.

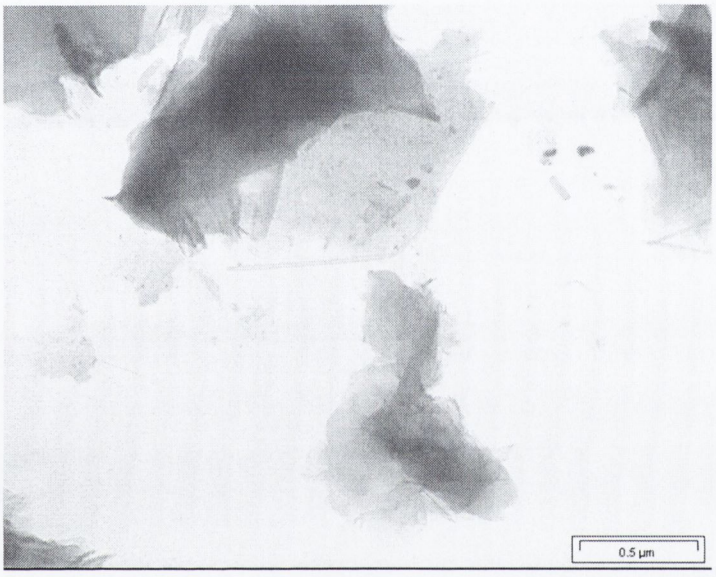

Figure 3.10 TEM of graphitic particles (GP)

These are found to consist of nanometer and micrometer uneven layered structures which are on the same length scale as the nanotubes samples.

KGP samples are expected to more closely represent the type of graphitic impurities contained in the MWNT samples. The TEM picture in figure 3.11 shows the KGP sample. These samples were found to consist of many bucky onions and fused graphitic particles.

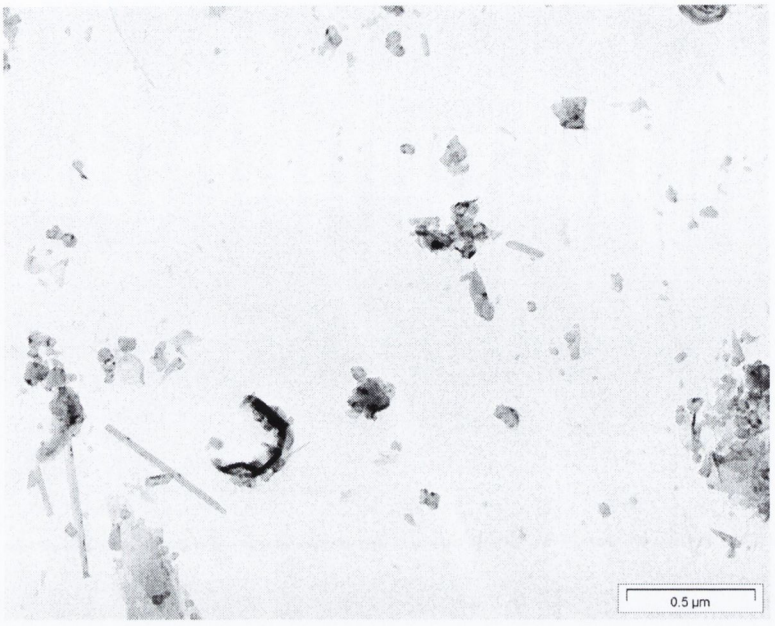

Figure 3.11 TEM of Kratschmer generator GP shell particles

The KGP samples therefore contain matter similar to that which is found in unpurified MWNT samples.

Carbon Nanotube Purity

The purity of carbon nanotube samples is a problem due to the difficulty in separating the nanotubes from the carbonaceous material that results in their production. Recent work here at Trinity College Dublin has shown that efficient purification of carbon nanotubes can be achieved through the incorporation of the nanotubes into a polymer matrix to form a polymer nanotube composite[5]. Mixing nanotube powder with a solution of the conjugated polymer, poly(m-phenylene-vinylene-co-2,5-dioctyloxy-p-phenylene-vinylene) (PmPV), results in the selective interaction of PmPV strands and nanotubes. These polymer-coated nanotubes remain in solution while graphitic impurities sediment out[12]. This impurity material can be removed by decantation yielding a composite solution containing 91 % nanotubes.

TEM images of the purified MWNT samples, shown in figure 3.12 show very clean nanotubes with few graphitic impurities present. The material to the top right of the TEM image is residue polymer used in the purification process.

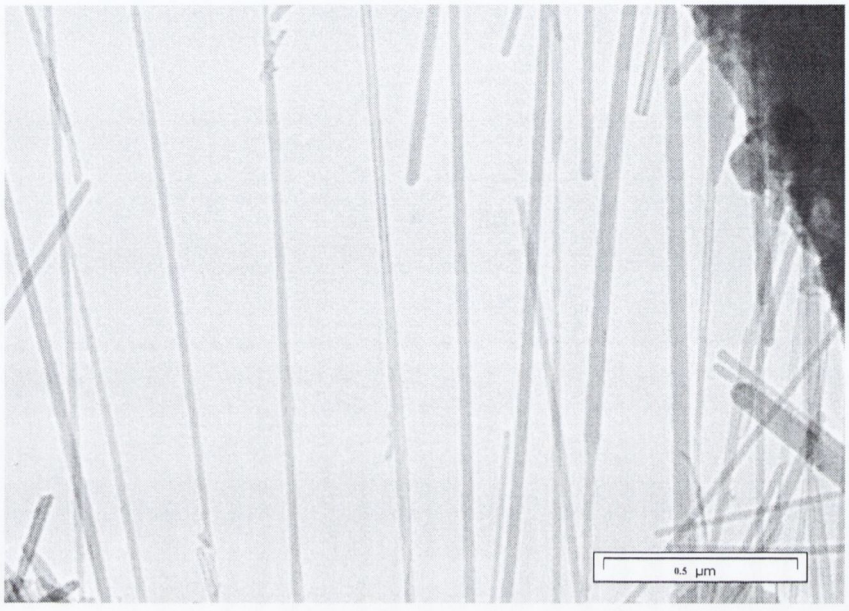

Figure 3.12 TEM of Purified $MWNT_{Trinity}$

In all cases, the production of the polymer nanotube composite results in a solution that is darker than the original polymer, almost black in the case of high concentration MWNT composites, but only slightly darker for SWNT composites. The maximum weight of nanotubes that can be held in stable solution by PmPV is highly concentration dependent, but for all cases, the mass of MWNT is orders of magnitude greater than the SWNT. SWNT themselves tend to aggregate substantially, the majority forming ropes. This hinders interaction with, and coating by, the PmPV, hence limiting the amount of SWNT that can be held in solution.

Sample Preparation

The method was similar for preparation of both MWNT-based and SWNT-based, samples differing mainly in concentration of sample used. Three different solutions were prepared. Two sample suspensions of SWNT, $MWNT_{Trinity}$, $MWNT_{USA}$, GP and KGP were prepared by sonicating the material powders in

naphthalene/dimethylformamid (NDMF) solutions and sodium dodecyl sulfate/deionised water (SDS) solutions. The NDMF is understood to solubilise the nanotubes through the wetting action of the naphthalene rings in a similar manner to the action of the PmPV polymer in the composite. SDS is a surfactant and acts to suspend the nanotubes through the interaction of the surfactant micelles. The third solution used the PmPV polymer nanotube composite, which has been shown in previous work to purify MWNT to a level of 91 %[12]. The composite solution was prepared by mixing $MWNT_{Trinity}$ with PmPV in toluene solution and sonicating. After a period of several hours, sediment formed in the bottom of the composite and MWNT NDMF solutions. Decantation was used to separate the sediment leaving stable solutions. In the case of GP and KGP NDMF solutions, after a period of several hours stable suspensions were produced, and the precipitate was removed by decantation. SDS solutions did not produce any separable precipitate but served to satisfactorily suspend the material powders in solution. Both solution and solid-state investigations were carried out. Solid-state samples were prepared by either drop casting or spinning.

Raman Spectroscopy

Raman spectroscopy has been shown to be an important tool for characterising SWNT. Two features dominate a typical SWNT spectrum. In the low-frequency region (~200 cm^{-1}), there is a mode characteristic of the radial breathing of the SWNT nanotube[11]. The frequency of this mode has been predicted to be essentially dependent on the tube diameter[13]. This feature is normally broad due to the poly-dispersivity of a typical SWNT sample. In the high-frequency region (~1600 cm^{-1}), there is a feature, which arises from the ordered graphitic lattice structure of the nanotubes known as the G line. There is also a feature at 1350 cm^{-1} (the so-called D line), which arises mainly from disordered graphitic carbon particles[14]. Thus, the relative intensities of these two peaks can be used to give some indication of the purity of a nanotube sample.

Raman spectroscopy was carried out on an Instruments S.A. Labram 1B in reflectance mode. Powdered samples were placed onto a glass microscope slide. Raman spectra of SWNT and MWNT powders are shown in figure 3.13 and figure 3.14 respectively.

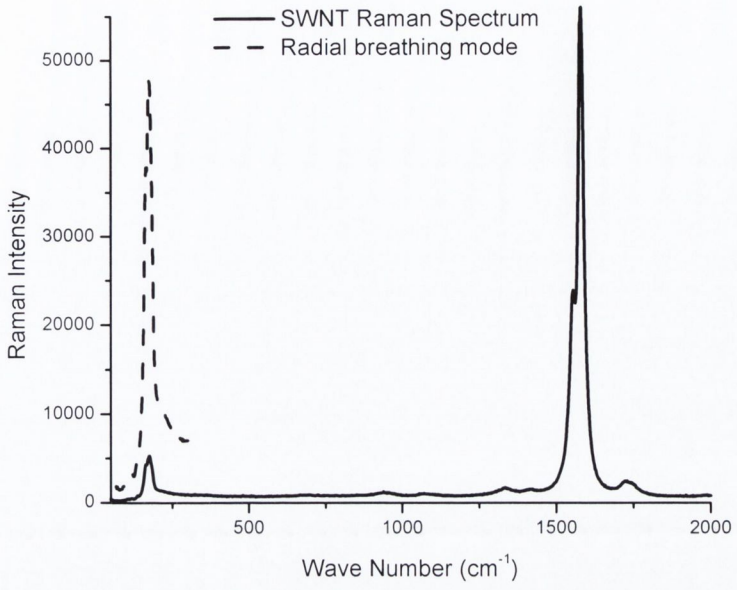

Figure 3.13 Raman spectrum of SWNT showing radial breathing mode

The Raman spectrum of the SWNT is typical with a strong breathing mode feature present. The feature at 1350 cm^{-1} is weak while the G-line is strong indicating a good quality samples. The MWNT Raman spectrum also shows a weak D line and strong G line.

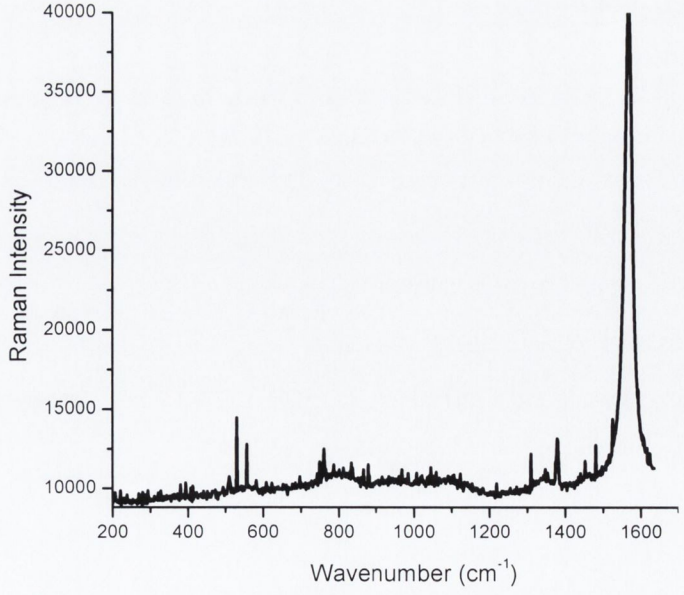

Figure 3.14 Raman spectrum of MWNT

The radial breathing modes are not observed in MWNT as the dispersion due to the multi shell nature causes it to be smeared out.

3.3 Detection of van Hove Singularities in Multiwalled Nanotubes

The absorption spectrum of carbon nanotubes shows, as expected, many of the feature of graphite. A large π-plasmon resonance is observed which peaks in the 5 eV to 6 eV region. This is due to the collective oscillation of the π-electrons and tails back into the near infrared region. However, quantisation effects in carbon nanotubes gives rise to regions of high concentration in the density states known as the van Hove singularities.

3.3.1 Van Hove Singularities in Singlewalled Nanotubes

A typical SWNT absorption spectrum is shown in figure 3.15. On closer examination weak peaks can be identified residing on the π-plasmon absorption. These correspond to van Hove singularities (VHS) in SWNT.

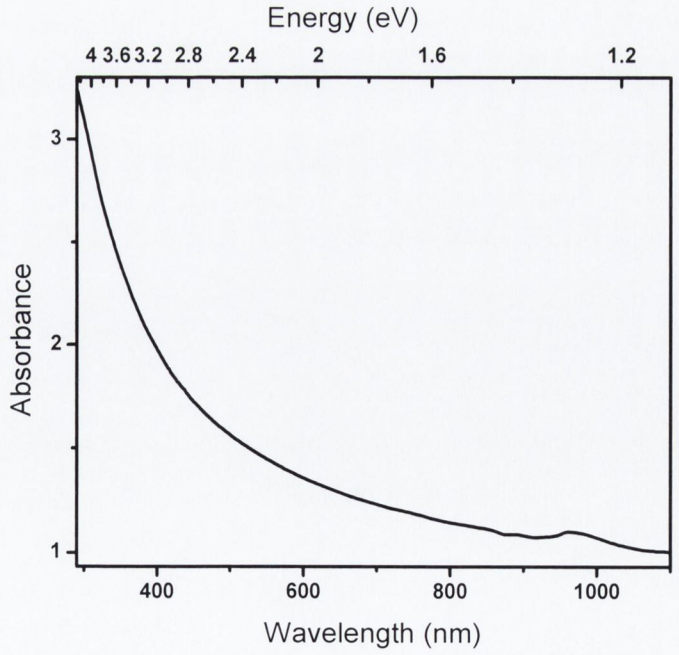

Figure 3.15 SWNT absorption showing π-plasmon & van Hove singularities

The peaks are revealed more clearly by subtraction of the π-plasmon background as shown in figure 3.16. This procedure follows the method used by Petit et al[15] and assumes that the plasmon approximates to a straight line in the region of the singularity hence allowing the subtraction of a straight line along the plasmon in order to expose the presence of the singularities.

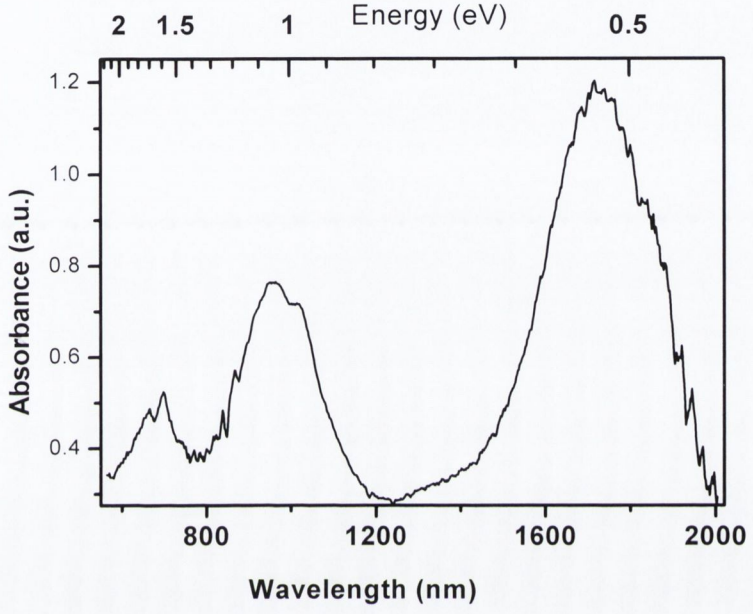

Figure 3.16 SWNT van Hove Singularities absorption bands

These VHS peaks are well known in SWNT and their positions have been assigned theoretically[16]. The VHS absorption bands are broad due to the dispersion of nanotube types within the sample. They are in fact a superposition of narrower absorption bands corresponding to the response of individual single-wall nanotubes of different chiral indices and/or of different diameters. The inverse relationship between the bandgap and diameter of SWNT allows the diameter distribution of the nanotubes to be estimated from the position of the van Hove singularity peaks in the absorption spectrum[17].

Figure 3.17 shows van Hove singularities in SWNT and their corresponding diameter distribution[13]. In accordance with the inverse relationship, larger diameter nanotubes have a smaller the band gap. On examining the peak positions of the van Hove singularities measured for the SWNT used in this work, as shown in figure

3.16, it can be concluded that these SWNT are somewhat larger than those depicted in figure 3.17.

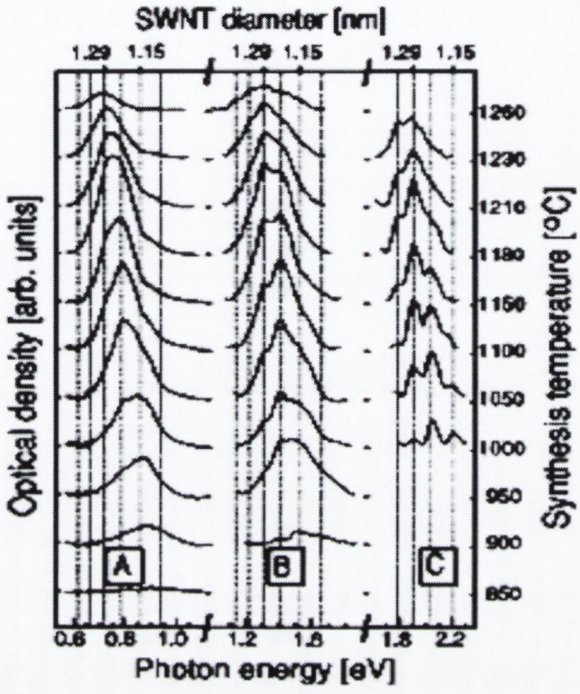

Figure 3.17 Diameter distributions of Van Hove singularities in SWNT[13]

It is estimated that the diameter range of the SWNT used here peaks between 1.3 nm and 1.6 nm.

3.3.2 Predictions for van Hove Singularities in Multiwalled Nanotubes

The position of van Hove singularities in the DOS of SWNT can be calculated theoretically shown in figure 3.18 and 3.19. Figure 3.18 shows the DOS calculations for an (8,8) SWNT and a bundle of SWNT[18]. A certain degree of damping and shifting of the van Hove singularity peaks is noticed in the case of the bundled SWNT.

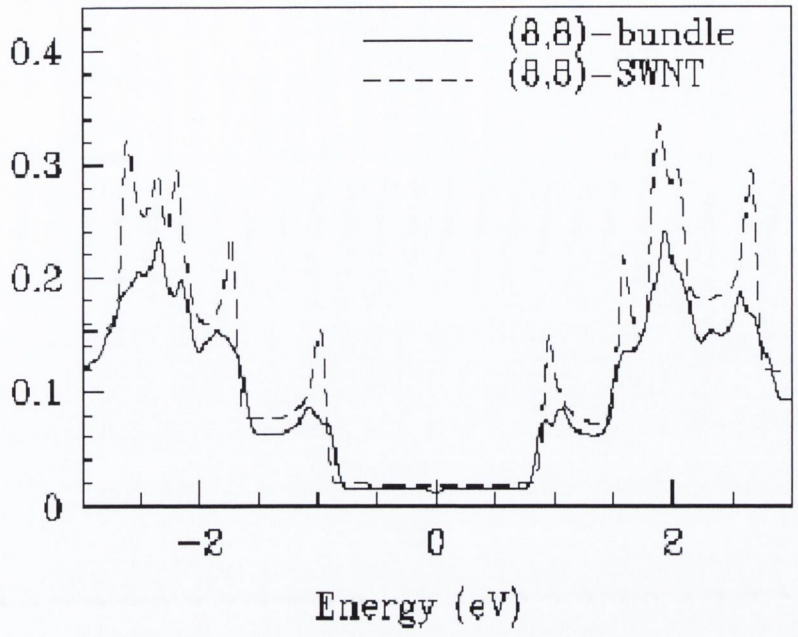

Figure 3.18 Calculations of van Hove Singularities in a SWNT & SWNT bundle

In figure 3.19 calculations for the DOS of a MWNT composed of three SWNT shells namely, (5,5), (10,10) and (15,15) is shown[18]. The MWNT is shown to exhibit distinct van Hove singularity peaks with little diminishment of peak sharpness occurring as a result of the intershell interactions.

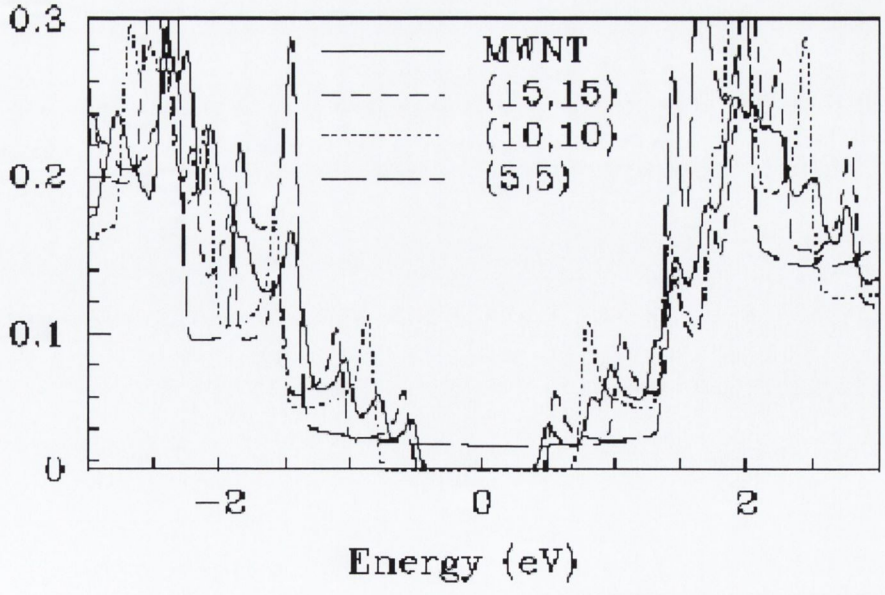

Figure 3.19 Calculations for a MWNT showing van Hove singularity peaks

It is intuitive therefore that van Hove singularities can be observed in the absorption spectra of MWNT. The inverse relationship between the nanotube bandgap and diameter enables predictions to be made about MWNT VHS spectra. In SWNT the band edge is found in the 0.5 eV region of the VHS spectrum. MWNT have several concentric shells, which are closely incremented and are larger. The VHS spectral edge can therefore be expected to be located further into the infrared region,and the singularity peaks can be expected to be distributed throughout the spectrum.

3.3.3 Optical Detection of van Hove Singularities in Multiwalled Nanotubes

Examination of absorption spectra of MWNT does indeed reveal the presence of van Hove singularity peaks. Measurements were performed in the solid state in order to avoid any contribution from solvent vibrations, which occur in the near infrared region. Films were produced by drop casting onto glass substrates in the case of UV-Vis measurements and KBr disks in the case of infrared measurements. Spectra were taken in the UV-Vis region from 300 nm to 1100 nm, in the near infrared region from 900 nm to 4000 nm and in the infrared region form 2500 nm to 30,000 nm, using three different instruments.

UV/Vis – NIR Detection

The UV-Vis-NIR absorption spectra of drop MWNT films are shown in figure 3.20 and figure 3.21. The spectra shown were taken using two different instruments, and background subtraction was carried. The raw data before background subtraction for the visible section of these spectra is shown in later in figure 3.28 and that for the NIR region is shown as an inset in figure 3.21.

In figure 3.20, an attempt at overlapping the common spectral regions of the two spectrometers between 1000 nm and 1150 nm has been made. Such overlapping region is omitted in figure 3.21. Joining spectra is generally unsatisfactory, as an artefact or jump in the absorbance magnitude due to an inherent feature of the excitation lamp and poor resolution in the overlap region, means joining the spectra is unreliable.

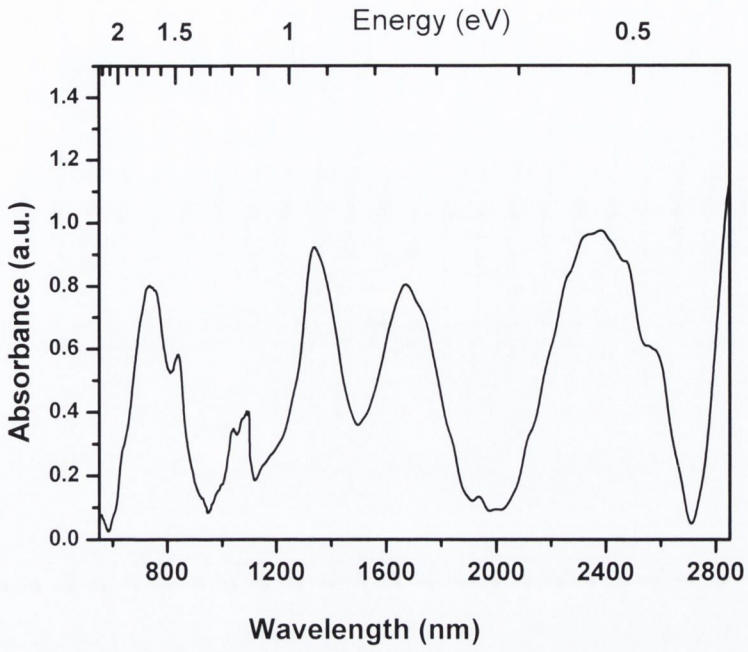

Figure 3.20 Joined MWNT absorption spectra showing van Hove singularity peaks

In both spectra a series of peaks are observed throughout the spectral range examined, beginning at 600 nm and continuing into the infrared region.

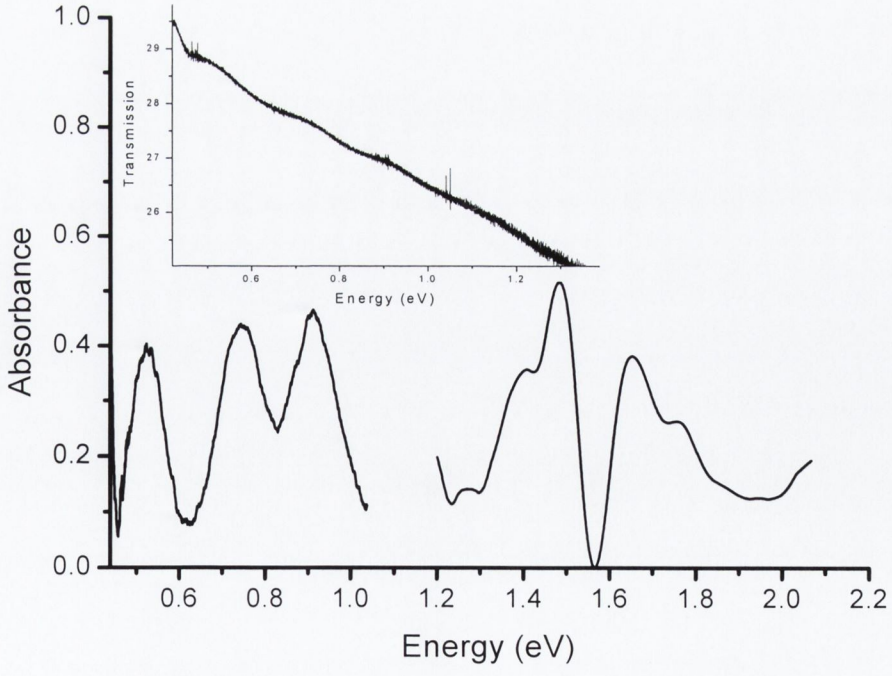

Figure 3.21 MWNT absorption showing van Hove singularity absorption Inset shows near infrared region prior to background subtraction.

The peaks are broad and contain some features. As anticipated for a multishell structure, the peaks are more numerous and lie closer together than those seen in SWNT.

Infrared Detection

Beyond the 3000 nm region vibrations due to bond stretchings shown in figure 3.22, dominate the spectrum and the presence of singularities cannot be easily elucidated in this region. Carbon nanotubes readily adsorb elements from its surrounding environment and hence water, oxygen and other contaminants are generally present. Typical bond stretches, including vibrations from 0H and C-H contaminants around the 3000 cm^{-1} and 8000 cm^{-1} respectively are apparent in figure 3.22.

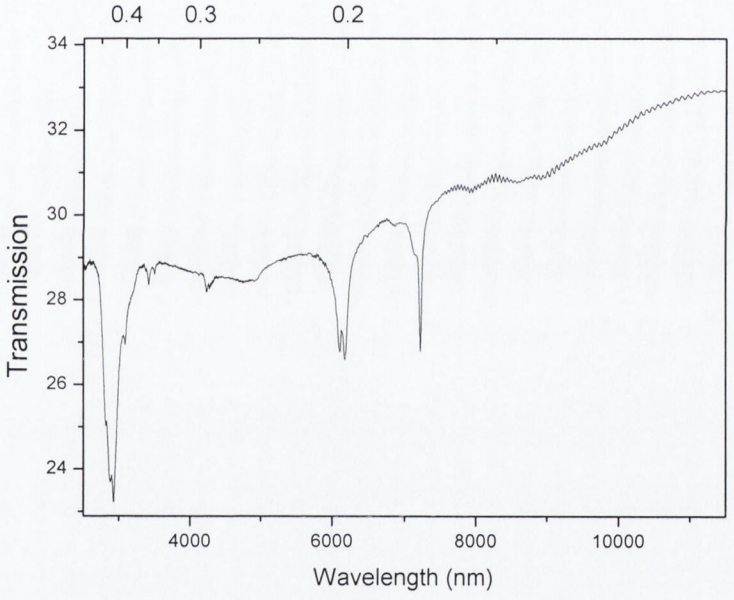

Figure 3.22 Bond Stretch absorption in MWNT

A spectrum of a MWNT Polymer composite, measured in reflectance mode using a film drop cast onto a gold plated microscope slide, is shown in figure 3.23. Typical bond stretches of the polymer dominate the spectrum[19], such as aryl peaks at 3020 cm^{-1}, and the various C-H stretches between 2925 cm^{-1} and 2850 cm^{-1}. However, features either side of the C-H stretches in the 4000 cm^{-1}-2000 cm^{-1}, cannot be associated with the polymer.

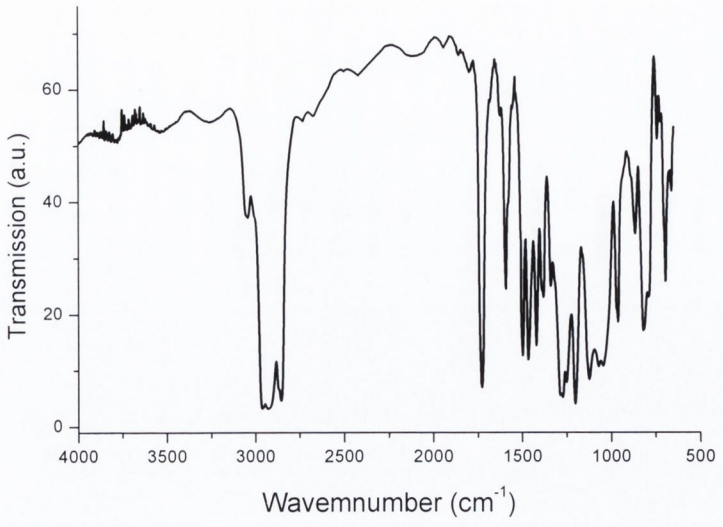

Figure 3.23 Infrared absorption from MWNT Polymer composite

This region of the spectrum is shown as a function of energy in figure 3.24.

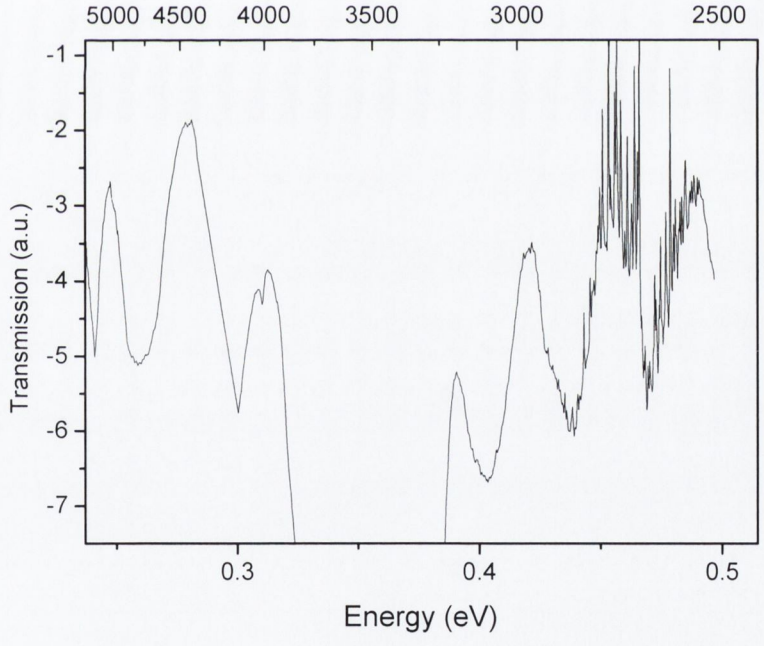

Figure 3.24 Van Hove singularity absorption features in MWNT-Polymer composite

Again peaks indicative of van Hove singularities are observed either side of the main polymer feature.

Far Infrared Detection

Further out in the infrared the presence of singularities are again observed. The spectrum in figure 3.25 and 3.26 is extended out to 30000 nm. Further peaks are clearly observed and extend to the limit of the FTIR spectrometer's range.

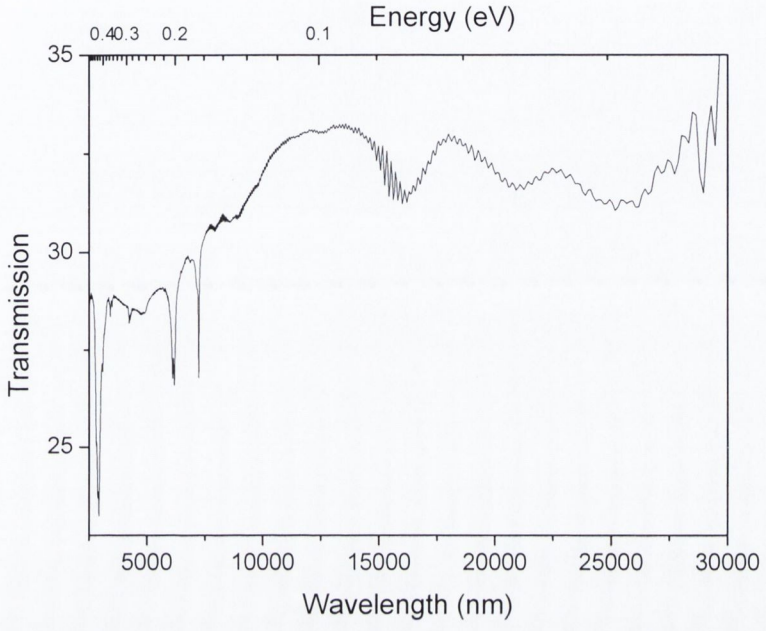

Figure 3.25 Absorption spectrum showing van Hove singularities in far infrared.

In figure 3.26 the far infrared region has been plotted in as a function of energy.

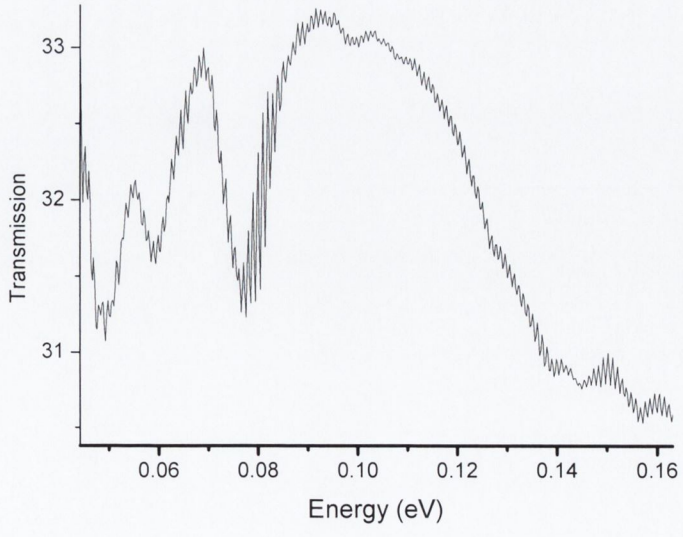

Figure 3.26 Far infrared MWNT van Hove singularities

The presence of singularities in this region of the spectrum is in keeping with the larger diameter of MWNT, and hence their lower energy bandgaps.

Oscillations suggestive of Fabry-Perot resonances are observed in some of the previous figures including figures 3.20, 3.23 and 3.25. Such resonances can occur as a result of the interference pattern produced by the surfaces of a thin film. The formula shown in equation (3.1) can be used to calculate the thickness of such a film.

$$b = \frac{n}{2(\nu_1 - \nu_2)} \tag{3.1}$$

where b is the thickness of the film, n is the number of fringes between ν_1 and ν_2, and ν_1 and ν_2 are the respective wavenumbers chosen for the limits of the range in which well defined fringes can be counted. It is useful to apply this analysis in order to ensure that any Fabry-Perot resonances present do not impede the resolution of van Hove singularity peaks. The drop cast films which were used are estimated to have thicknesses in the nanometer range. These were generally of poor quality, being highly inhomogeneous, which, though not a disadvantageous for the objective of measuring van Hove singularity absorption, is not expected to lend towards the generation of Fabry-Perot resonance fringes.

Applying equation (3.1) to the peaks to the data used in figures 3.20 and 3.23 gives thickness of 2.5μm and 50μm respectively. These thickness values do not correspond to anything near what the real thickness of the samples and hence it can be concluded that the observed peaks do not originate from Farby perot resonances. In the case of the data in figure 3.25, the small oscillations residing on the main data correspond to a thickness of 16μm. These features closely represent the typical appearance of Fabry Perot resonances, however again the thickness value is not correct. It is more likely that the features are due to factors such as the oscillatory behaviour of the lamp at these very long wavelengths which are at the edge of its range, or fluctuations in the environmental conditions.

Visible Detection

For purposes of the investigations carried here, the presence of van Hove singularities in the visible and near-infrared regions are of most interest. The absorption spectrum in figure 3.27 focuses on singularities in this region. It shows singularities in $MWNT_{USA}$, which are typical for this region. The spectrum consists of three well-resolved peaks and a number of shoulders in the visible and near-infrared regions. A background subtraction has been performed to remove the influence of the π-plasmon. The inset shows the raw date prior to background subtraction.

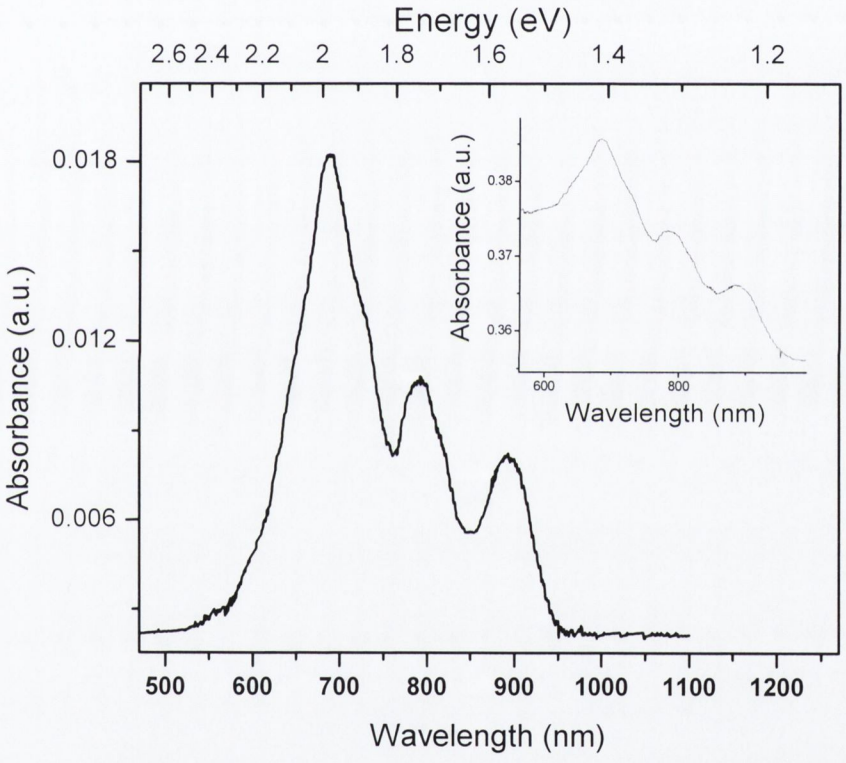

Figure 3.27 Van Hove singularity peaks for $MWNT_{USA}$ in the visible region Inset shows raw data

Luminescence, which is described in more detail in chapter 5, has been observed whose spectrum shows a sharp rise beginning at about 550 nm and falls sharply beyond 930 nm. Significant also is the fact that no further peaks were identified at energies greater than 2.4 eV. This is in keeping with the larger nature of MWNT, which given the inverse relationship between tube diameter and tube band gap, can be expected to have small band gaps with a weakening of VHS features at higher

energies. It is therefore possible that further singularities exist above 2.4 eV which do not contribute greatly to the nanotube's spectrum and hence are not apparent.

Other spectra, such as those shown in figure 3.28, have a similar profile in the same spectral range, though the resolution is often not as well defined. The swamping of the singularities by the π-plasmon resonance is significant, particularly in the visible region where the plasmon is stronger. Low film thickness with well separated nanotubes give the best spectra. The spectra shown in figure 3.28 are for three different drop cast films of purified $MWNT_{Trinity}$.

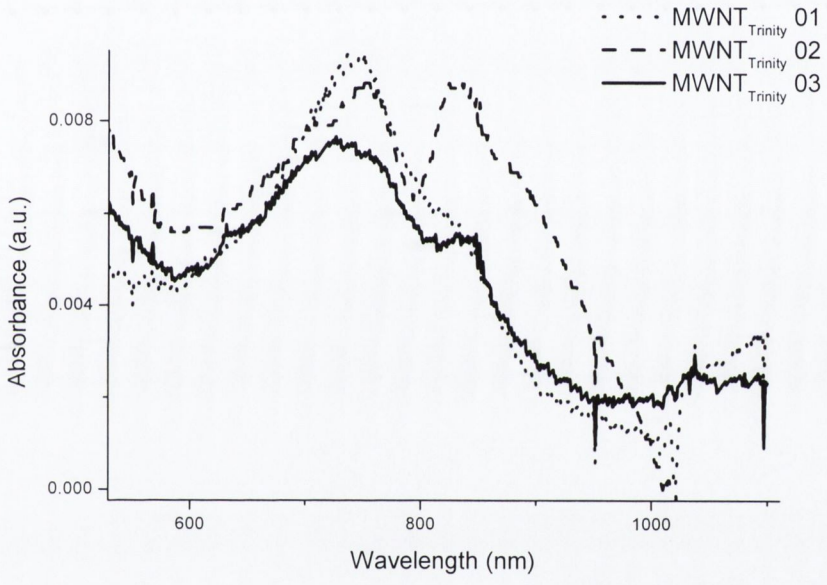

Figure 3.28 Van Hove singularity peaks for purified $MWNT_{Trinity}$ prior to background removal

Peaks are located in a similar region in the three spectra, though the definition of the peaks varies. The lack of clarity in the VHS absorption spectra of MWNT is to be expected given their complexity of their structures and the intershell and intertube interactions that can occur. Singularity features in SWNT can also vary, as can be seen from comparison with the spectra in figure 3.17, which shows the effect of the synthesis temperature on the SWNT diameter distribution.

3.4 Implications for Material Nonlinear Optical Properties

The linear optical properties of a material have a profound influence on their nonlinear optical properties. Expectations of the material nonlinear optical performance and the multiphoton processes, which they can support, as indicated by characteristics of their basic properties, are now explored.

3.4.1 Endohedral Metallofullerene La@C_{82}

The nonlinear properties of La@C_{82} are expected to follow the foundations set by C_{60}. Although it was not possible to obtain a sample of C_{82} for measurement here, the results for the endohedral fullerene can be compared with those in the literature for C_{60} and other higher order fullerenes. The nonlinear response of C_{60} is characterised by a considerable ultrafast nonlinearity as well as efficient reverse saturable absorption. An improved response is expected from La@C_{82} compared to C_{60}. Increase in the magnitude of the optical nonlinearity with fullerene size has been reported in the literature[20]. The presence of the La atom and the extra electrons it donates to the fullerene cage is anticipated to enhance this effect. In addition, the broader wavelength range of the linear absorption means that La@C_{82} will be able to support nonlinear optical activity over a much broader wavelength range.

3.4.2 Carbon Nanotubes

The full extent of the nonlinear optical behaviour of carbon nanotubes cannot be readily predicted. Carbon nanotubes possess many important attributes, which can be anticipated to contribute to a large, broadband and ultrafast response. However, issues such as the influence of the VHS cannot be completely foretold. It is intuitive to expect large resonant enhancement of multiphoton interactions and hence optical nonlinearities at energies coincident with the singularities. These expectations are supported by theoretical calculations given in the literature[21]. These calculations predict very large $\chi^{(3)}$ values in certain spectral regions due to multiphoton resonant enhancement processes in nanotubes.

3.4.3 Axially Substituted Phthalocyanines

Metallophthalocyanines are well known as reverse saturable absorbing materials. The linear absorption spectrum, with its weak absorption window, provides ideal conditions for reverse saturable absorption. The objective here is to investigate the influence of axial groups on the phthalocyanine reverse saturable absorption performance. These axial substituents depicted in figure 3.2 and 3.3 act as electron withdrawing groups, with compound A being the weakest, and compound D being the strongest due to the two cyano groups. Hence the double cyano electron withdrawing group in compound D is expected to have the greatest impact on the basic phthalocyanine structure. Empirically the reverse saturable absorption response can be expected to follow a similar pattern. This argument follows from previous investigations which have shown that alterations to the basic phthalocyanine such as the addition of peripheral groups can improve its optical limiting response[22]. Though no specific theory has been developed to explain these findings it is proposed that the alterations affect the electronic structure of the phthalocyanine and in particular improves the efficiency of electron crossing to the triplet state.

The sample degradation problems can be expected to reduce the full magnitude of the nonlinear absorption response. However, using freshly prepared samples and assuming that the degradation occurs at the same rate in all samples, as indicated by the absorption spectra in figures 3.4 and 3.6, the trend in the nonlinear behaviour should be preserved.

3.5 Conclusions

The scene has been set for material investigations of nonlinear optical response and the multiphoton interactions from which they originate. The basic material properties, most importantly including linear absorption and sample morphology have been characterised giving a portrait of the materials. Predictions for the nonlinear optical performance of the materials have been made, by taking account of the material characteristics and applying established criteria and precedent.

References

[1] S. Lebedkin, Max Planck Institute Kernphys, D-69029 Heidelberg, Germany.

[2] S. Lebedkin, B. Renker, R. Heid, H. Schober, and H. Rietschel, Applied Physics a-Materials Science & Processing **66** *3*, 273 (1998).

[3] H. Shinohara, Reports on Progress in Physics **63** *6*, 843 (2000).

[4] M. Hanack, University of Tubingen, Inst. Organic Chemistry, D-72076 Tubingen, Germany, Private communication.

[5] Jonathan N. Coleman, Alan B. Dalton, Seamus Curran, Angel Rubio, Andrew P. Davey, Anna Drury, Brendan McCarthy, Bernd Lahr, Pulickel M. Ajayan, Siegmar Roth, Robert C. Barklie, and Werner J. Blau, Advanced Materials **12** *3*, 213 (2000).

[6] P. Bernier, University of Montpellier 2, Dynamic Phases & Condenses Group, F-34095 Montpellier 05, France.

[7] C. Journet, W. K. Maser, P. Bernier, A. Loiseau, M. L. delaChapelle, S. Lefrant, P. Deniard, R. Lee, and J. E. Fischer, Nature **388** *6644*, 756 (1997).

[8] J. N. Coleman, D. F. O'Brien, B. McCarthy, R. C. Barklie, and W. J. Blau, Monatshefte Fur Chemie **132** *1*, 53 (2001).

[9] J. N. Coleman, D. F. O'Brien, A. B. Dalton, B. McCarthy, B. Lahr, A. Drury, R. C. Barklie, and W. J. Blau, Chemical Communications *20*, 2001 (2000).

[10] BuckyUSA 5933 Bellaire Blvd, Suite 113, Houston, TX 77081, USA.

[11] T. W. Ebbesen, Annual Review of Materials Science **24**, 235 (1994).

[12] B. McCarthy, J. N. Coleman, R. Czerw, A. B. Dalton, D. L. Carroll, and W. J. Blau, Synthetic Metals **121** *1-3*, 1225 (2001).

[13] A. M. Rao, E. Richter, S. Bandow, B. Chase, P. C. Eklund, K. A. Williams, S. Fang, K. R. Subbaswamy, M. Menon, A. Thess, R. E. Smalley, G. Dresselhaus, and M. S. Dresselhaus, Science **275** *5297*, 187 (1997).

[14] P. M. Ajayan and T. W. Ebbesen, *Nanometre-size tubes of carbon.* 1997.

[15] P. Petit, C. Mathis, C. Journet, and P. Bernier, Chemical Physics Letters **305** *5-6*, 370 (1999).

[16] J. W. G. Wildoer, L. C. Venema, A. G. Rinzler, R. E. Smalley, and C. Dekker, Nature **391** *6662*, 59 (1998).

[17] E. Richter and K. R. Subbaswamy, Physical Review Letters **79** *14*, 2738 (1997).

[18] A. Rubio, Applied Physics A **68**, 275 (1999).

[19] G. J. Lee, S. K. Yu, D. Kim, J. I. Lee, and H. K. Shim, Synthetic Metals **69** *1-3*, 431 (1995).

[20] H. J. Huang, G. Gu, S. H. Yang, J. S. Fu, P. Yu, G. K. L. Wong, and Y. W. Du, Chemical Physics Letters **272** *5-6*, 427 (1997).

[21] R. H. Xie, Nuovo Cimento Della Societa Italiana Di Fisica D. **19** *12*, 1867 (1997).

[22] F. Z. Henari, J Callaghan, W. J.Blau, P Haisch, M Hanack, Pure and Applied Optics **6** 6, 741 (1997)

Chapter 4
Nonlinear Optical Characterisation

Characterisation of the multiphoton processes and the corresponding nonlinear optical properties of the materials is presented. The various parameters of the material nonlinearities such as, magnitude, time response, and bandwidth are determined. The merits of the material performance and promising features are identified and recommendations of particular photonic tasks, for which the materials would be suited, are given. The material nonlinear response and the multiphoton interactions from which they originate, are analysed. It is found that many aspects of these processes can be related back to the material linear optical properties.

Third order nonlinear optical interactions give rise to a large number of phenomena. Various experimental techniques have been devised to study these phenomena and gain information on material third-order optical nonlinearities.

4.1 Experimental Techniques

Several experimental techniques are available to measure the various nonlinear optical parameters of materials. Here we use both a simple technique, known as Z-scan, and a more comprehensive technique, known as degenerate four wave mixing, to characterise the third order nonlinear optical properties of the materials. The Z-scan technique is an efficient method for examining third order nonlinearities, giving information on both the refractive and absorptive components and also on the sign of the nonlinearity. Degenerate Four-Wave Mixing (DFWM) is a more elaborate characterisation technique, but has the added benefit of measuring the time dependence of the nonlinearity.

The approach taken here has been to carry out general investigations using the more flexible Z-scan technique and to perform a more extensive characterisation using DFWM. The methodology of both techniques is described.

4.1.1 Z-scan Technique

The Z-scan technique was first published by Sheik-bahae et al[1] and has since become a standard tool for the determination of both real and imaginary third order susceptibility coefficients and the sign of the nonlinearity. Its strength derives from an ability to translate changes in beam curvature, induced by the nonlinear response of the sample under study, into detectable transmittance changes. The Z-scan principle involves traversing the sample under study along the path of a tightly focused Gaussian beam thereby subjecting it to a large range of intensities.

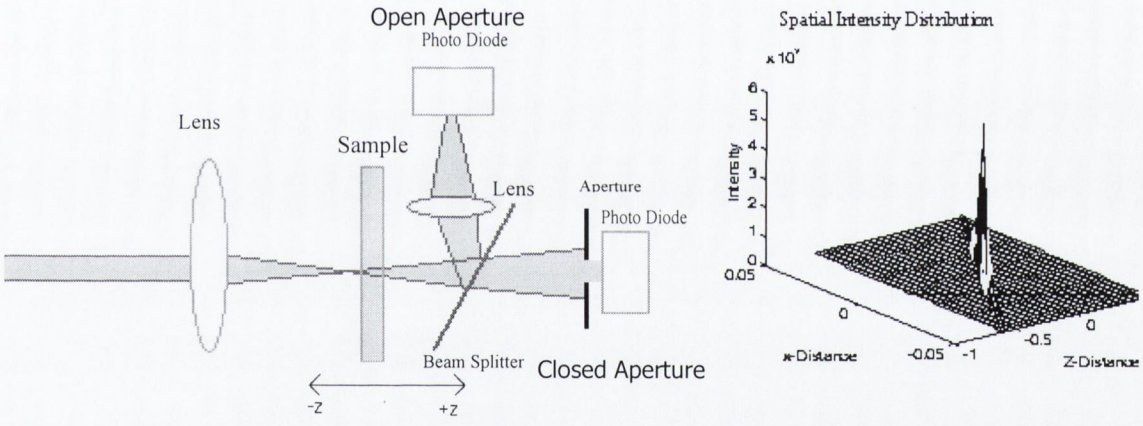

Figure 4.1 Schematic of Z-scan set up & spatial distribution of the beam intensity

A schematic of the arrangement used in Z-scan is shown in figure 4.1, also shown is a plot of how the intensity varies with position. Nonlinear behaviour can be induced above a threshold incident intensity. The transmitted power is measured as a function of sample position in the far field, using two detectors, one apertured and one unperturbed. The sensitivity of the experiment to the nonlinear refractive index, a real $\chi^{(3)}$ response, is due to the presence of the apertured detector, referred to as 'closed z-scan'. The unapertured detector detects transmittance changes due only to nonlinear absorption and is referred to as 'open z-scan'. The principles of the closed

and open z-scan measurements are best illustrated by example as given in the following sections.

Closed Z-scan Measurement of Refractive Nonlinearities

Consider the case of a material possessing a negative nonlinear refractive index and no absorptive nonlinearities, as it traverses the path of a tightly focused Gaussian beam, depicted in figure 4.2.

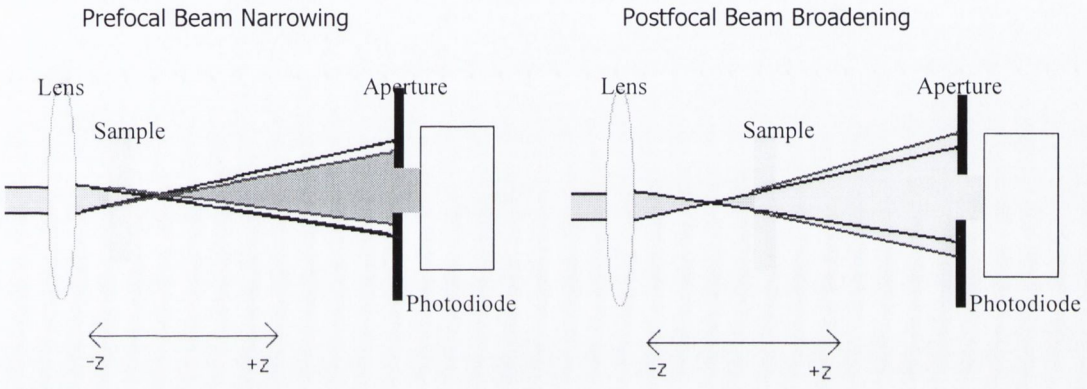

Figure 4.2 Schematic of induced beam narrowing and broadening during Z-scan

Far from the focal position (negative z), incident intensities are low and negligible nonlinear behaviour results. Closer to the focus, the increased power densities are sufficient to induce nonlinear refraction or self-lensing in the sample. Negative self-lensing will tend to collimate the beam in the far field and consequently increase the power transmitted through the aperture. After the focal plane (positive z) the same self-defocusing nonlinearity causes increased beam divergence leading to beam broadening at the aperture and a corresponding decrease in transmittance. Hence a prefocal transmittance maximum followed by a post focal transmission minimum is the typical Z-scan signature for a negative refractive nonlinearity. Following a similar argument, positive nonlinear refraction gives rise to the opposite valley-peak configuration.

Open Z-scan Measurement of Absorptive Nonlinearities

The open Z-scan corresponds to the measurement of the total transmittance through

the sample, i.e. with no aperture in front of the detector. It only sees the nonlinear absorption that is the imaginary component of the nonlinearity. The nonlinear absorption can either be of the saturable or reverse saturable type depending on the sign of β in the material.

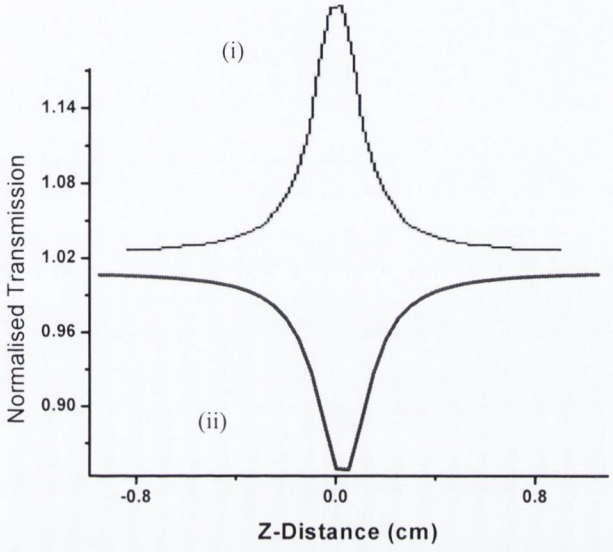

Figure 4.3 Z-scan measurement of (i) saturable and (ii) reverse saturable absorption

Both cases are shown in figure 4.3 as they would appear when measured using Z-scan. A peak about the focal point signifies saturable absorption, while a dip signifies reverse saturable or multiphoton absorption.

Theory of Z-scan Technique

The original formulation for z-scan is the treatment of the propagation of a Gaussian beam in a nonlinear medium[1]. A TEM_{00} Gaussian beam of waist radius (w_0) travelling in the +z direction is assumed. E can be written as

$$E(z,r,t) = E_0(t)\frac{w_0}{w(z)}.\exp\left(-\frac{r^2}{w^2(z)} - \frac{ikr^2}{2R(z)}\right)e^{-i\phi(z,t)} \qquad (4.1)$$

where $w^2(z) = w_0^2(1+z^2/z_0^2)$ is the beam radius, $R(z) = z(1+z_0^2/z^2)$ is the radius of curvature of the wavefront at z, $z_0 = kw_0^2/2$ is the diffraction length of the beam,

$k = 2\pi / \lambda$ is the wave vector, and λ is the laser wavelength. $E_0(t)$ denotes the electric field at the focus and contains the temporal envelope of the laser pulse. The $e^{-i\phi(z,t)}$ term contains all the radially uniform phase variations. Only the radial phase variations, $\Delta\phi(r)$, are calculated here and all other phase changes that are uniform in r are ignored. The slowly varying envelope approximation (SVEA), can be applied. A thin medium is assumed, meaning that changes in the beam diameter within the sample are small enough to be neglected. This requires that $L < z_0$, where L is the sample length. The amplitude and $\sqrt{I}$ and phase ϕ of the electric field as a function of z' are now governed in the SVEA by the following two equations:

$$\frac{d\Delta\phi}{dz'} = \Delta n(I)k \tag{4.2}$$

$$\frac{dI}{dz'} = -\alpha(I)I \tag{4.3}$$

where z' is the propagation depth in the sample and α(I), includes the linear and nonlinear absorption terms. In the case of a cubic nonlinearity and negligible nonlinear absorption (4.2) and (4.3) are solved to give the phase shift $\Delta\phi$ at the exit surface of the sample which simply follows the radial variation of the incident radiation at a given position z. Thus,

$$\Delta\phi(z,r,t) = \Delta\phi_0(z,t)\exp\left(-\frac{2r^2}{w^2(z)}\right) \tag{4.4}$$

with

$$\Delta\phi_0(z,t) = \frac{\Delta\phi_0(t)}{1 + z^2 / z_0^2} \tag{4.5}$$

$\Delta\phi_0(t)$, the on-axis phase shift at the focus, is defined as

$$\Delta\phi_0(t) = k\Delta n_0(T)L_{eff} \tag{4.6}$$

where $L_{eff} = (1 - e^{-\alpha L})/\alpha$ and here α is the linear absorption coefficient.

The electric field exiting the sample Ee now contains the nonlinear phase distortion

$$E_e(r,z,t) = E(r,z,t)e^{-\alpha L/2}e^{i\Delta\phi(z,r,t)} \tag{4.7}$$

A treatment method known as Gaussian Decomposition[1] can now be applied. This involves the decomposition of the electric field at the exit plane of the sample into a summation of Gaussian beams through a Taylor series expansion of the nonlinear phase term $e^{i\Delta\phi(z,r,t)}$. That is,

$$e^{i\Delta\phi(z,r,t)} = \sum \frac{[i\Delta\phi_0(z,t)]^m}{m!} e^{-2mr^2/w^2(z)} \tag{4.8}$$

Each Gaussian beam can now be propagated to the aperture plane and there be re-summed to reconstruct the beam. The resultant electric field pattern at the aperture becomes

$$E_a(r,t) = E(z,r=0,t)e^{-\alpha L/2}\sum_{m=0}^{\infty}\frac{[i\Delta\phi_0(z,t)]^m}{m!}\frac{w_{m0}}{wm}\exp\left(-\frac{r^2}{w_m^2}-\frac{ikr^2}{2R_m}+i\theta_m\right) \tag{4.9}$$

Defining d as the propagation distance in free space from the sample to the aperture plane and g=1+d/R(z), the remaining parameters in (4.9) are expressed as

$$w_{m0}^2 = \frac{w^2(z)}{2m+1},\quad d_m = \frac{kw_{m0}^2}{2},\quad w_m^2 = w_{m0}^2\left[g^2+\frac{d^2}{d_m^2}\right],\quad R_m = d\left[1-\frac{g}{g^2+d^2/d_m^2}\right]^{-1} \text{ and}$$

$$\theta_m = \tan^{-1}\left[\frac{d/d_m}{g}\right].$$

The transmitted power through the aperture is obtained by spatially integrating Ea(r,t) up to the aperture radius ra, giving

$$P_T(\Delta\Phi_0(t)) = c\varepsilon_0 n_0 \pi \int_0^{r_a} |E_a(r,t)|^2 r dr \tag{4.10}$$

where ε_0 is the permittivity of free space. Including the pulse temporal variation, the normalised Z-scan transmittance T(z) can be calculated as

$$T(z) = \frac{\int_{-\infty}^{\infty} P_T(\Delta\Phi_0(t))dt}{S\int_{-\infty}^{\infty} P_i(t)dt} \tag{4.11}$$

where $P_i(t) = \pi w_0^2 I_0(t)/2$ is the instantaneous input power within the sample and $S = 1 - \exp(-2r_a^2 / w_a^2)$ is the aperture of linear transmittance with wa denoting the beam radius at the aperture in the linear regime.

Again considering equation (4.9) the normalised Z-scan transmittance can be simplified as

$$T(z, \Delta\Phi_0) = \frac{\left|E_a(z, r=0, \Delta\phi_0)\right|^2}{\left|E_a(z, r=0, \Delta\phi_0 = 0)\right|^2}$$

$$= \frac{\left|(g + id/d_0)^{-1} + i\Delta\phi_0 (g + id/d_0)^{-1}\right|^2}{\left|(g + id/d_0)^{-1}\right|^2} \qquad (4.12)$$

The far-field condition d >> z0 can be used to further simplify equation (4.12) to give a geometry-independent normalised transmittance as

$$T(z, \Delta\Phi_0) \approx 1 - \frac{4\Delta\Phi_0 x}{(x^2 + 9)(x^2 + 1)} \qquad (4.13)$$

Equation (4.13) is the theoretical fit which is applied to the closed aperture z-scan data. A satisfactory fit of this equation to the data confirms a real $\chi^{(3)}$ response in the material and enables a values for $\Delta\Phi_0$ be determined. The $\Delta\Phi_0$ can then be used to calculate the magnitude of the real $\chi^{(3)}$ response.

Calculation of Nonlinear Refractive Index

In the limit of a small nonlinear phase change ($|\Delta\Phi_0| << 1$) and employing the far field condition the Gaussian Decomposition method enables the normalised Z-scan transmission to be expressed as in equation (4.13).

The calculation of the real $\chi^{(3)}$ value involves computing the n_2 values which are given by

$$n_2 = \frac{\sqrt{2}\Delta\phi_0}{L_{eff} k I_0} \qquad (4.14)$$

where $\Delta\phi_0$ is obtained from fitting (4.14) to each of the Z-scan signatures. Real $\chi^{(3)}$, ($\Re e\chi^{(3)}$) is then obtained in the traditional Gaussian units by

$$\Re e\chi^{(3)}(esu) = \frac{10^{-6}}{480\pi^2} cn_0^2 n_2 \qquad (4.15)$$

where c is the speed of light in cm/s and n_2 is in cm^2/W. For the case where nonlinearities are composed of opposite signs within a sample, a simple addition of the parameters was performed.

Calculation of Nonlinear Absorption Coefficient

The open Z-scan corresponds to the measurement of the total transmittance through the sample, i.e. with no aperture in front of the detector. It only sees the nonlinear imaginary component of the material, i.e. nonlinear absorption. In the case of two-photon absorption, which is described by equation (4.6) with β positive, the energy transmittance as a function of position z, $T_{op}(z)$ has been calculated and is equal to

$$T_{op}(z) = T_0 \sum_{m=0}^{\infty} [-q_0(z,0)]^m / (m+1)^{3/2} \qquad (4.16)$$

where T_0 is the linear transmittance at low intensity and is equal to $e^{-\alpha_0 L}$, and

$$q_0(z,0) = \beta I_0(t=0) L_{eff} / (1+z^2/z_0^2) \qquad (4.17)$$

where, $L_{eff} = (1 - e^{-\alpha_0 L}) / \alpha_0$.

Equation (4.16) is the theoretical fit which is applied to the open aperture z-scan data. A suitable fit of this equation confirms an imaginary $\chi^{(3)}$ response in the material. However, equation (4.16) is only true as long as

$$| q_0(z=0,0) | < 1. \qquad (4.18)$$

The calculation of the $Im\chi^{(3)}$ value involved computing the β values which are calculated from the fitting of (4.16) to the open Z-scan curves. Imaginary $\chi^{(3)}$ ($Im\chi^{(3)}$) is then given by

$$\Im m\chi^{(3)}(esu) = \frac{10^{-6}}{480\pi^2} cn_0^2 \beta \qquad (4.19)$$

Z-scan Experiment

Measurements were taken on three different laser systems; namely a ps Nd:YAG, a wavelength tunable Nitrogen-Dye system producing 500 ps pulses and a nanosecond

Nd:YAG. The shorter pulsed lasers are the most useful as they provide a better examination of the faster nonlinear optical processes. The ps Nd:YAG is an active/passive mode-locked laser of the Continuum PY60 Series. It is operated at 1064 nm and at the frequency doubled 532 nm and delivering pulses at 10 Hz with a pulsewidth of 25 ps at 532 nm and 35 ps at 1064 nm. The Nitrogen–Dye laser system was used to take measurements at a number of wavelengths in the visible region and had a repetition rate of 3 Hz. The third laser system is a Q-switched Nd:YAG laser delivering 6ns pulses at a rate of 10 Hz.

These lasers are well suited to giving a good characterisation of the nonlinear optical properties of materials. They are capable of delivering high peak powers, necessary to observe nonlinear phenomena in materials. The wide wavelength range through out the visible region and the availability of 1064 nm in the near infrared region allows a large bandwidth to be tested. These lasers all operate at slow repetition rates, which helps to minimise thermal effects. As an illustration of the technicalities of a Z-scan experiment, one set up, where the ps Nd:YAG is detailed.

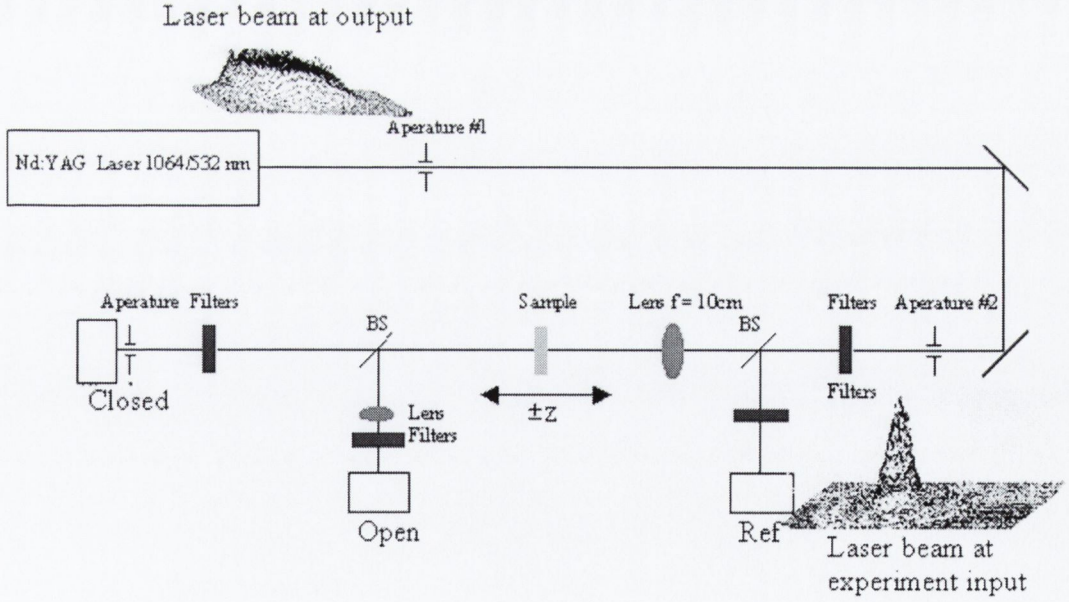

Figure 4.4 Z-scan set-up. Inserts show beam profile at output & after aperture #2.

The typical beam profile at the output of the laser is depicted in the first inset in figure 4.4, is clearly not a perfect Gaussian. The experimental set up in figure 4.4

included a means of up grading the beam profile to that shown in the second inset. In the ideal case, the fundamental TEM_{00} mode of a laser is a Gaussian wave. However, this set-up deals with the deviation of the laser beam profile from that of a Gaussian, which is required for Z-scan theoretical analysis. A clipped $somb^2$ beam profile is used to replace the defective Gaussian beam. Such a beam closely approaches a Gaussian profile and can be considered to satisfy the theoretical requirements. The laser beam departs from this theoretical function due to imperfections in the laser leading to fluctuations in the laser beam and the creation of higher spatial frequencies in addition to the fundamental one. An aperture is used to spatially smooth the laser beam and attain a more Gaussian like profile. The beam is first directed through an aperture and is subsequentially diffracted. In the far-field, the beam profile becomes a $somb^2$ function, $somb^2(x) = 4 J_1 2(\pi x) / (\pi x)^2$, where $J_1(x)$ is the first order Bessel function. The central part of this diffraction pattern approaches a Gaussian profile and can be selected by using a second aperture to "clip" the wings.

Experimental Considerations

The Z-scan experiments carried out here travel from the right to the left, unless other wise stated. A positive refractive nonlinearity will therefore have a 'dip-peak' signature and a negative refractive nonlinearity will have a 'peak-dip' signature. In cases where there is an absorptive nonlinearity, the influence of the absorption can be removed from the refractive signature by dividing the normalised closed scan by the normalised open scan.

Curve fitting the Z-scan signatures using the equations described in sections 4.1 enables the calculation of the various nonlinear optical parameters. However, as previously specified, conditions apply to these equations since they include assumptions, which mean that the mathematics involved in their derivation are only applicable to Z-scan signatures whose normalised values deviate within ± 20 % in the case of both the refractive and absorptive nonlinearities. Fitting Z-scan signatures, which deviate by a higher percentage, is possible by increasing the number of fitting iterations. However the values which result are no longer accurate though they may still contain some indicative information about the nonlinearities.

4.1.2 Degenerate Four Wave Mixing Technique

Degenerate Four Wave Mixing (DFWM) is the general description given to the interaction of three waves in a medium to produce a fourth wave via a third order nonlinear optical process. The excitation waves comprise of two antiparallel pump beams, the forward and backward beams, and a probe beam entering at an angle. The intensity of the generated beam is dependent on the coupling coefficient in the material, which is a function of the third order optical susceptibility. This can be used as a method of determining the magnitude of $\chi^{(3)}$ in materials.

A backward reflection geometry was used here, as it has the advantages of being automatically phase matched and the generated wave has the property that it is everywhere the time reversed wavefront of the input probe wave. Essentially, the forward and probe beams form a transient index grating in the material from which the backward beam diffracts into the phase conjugate wave.

Theory of Degenerate Four Wave Mixing

The generation of a phase conjugate beam can be explained by considering the third order polarisation. Assuming input waves of the form

$$E_i(\vec{r},t) = \frac{1}{2}[A_1(r)e^{i(k\cdot r-\omega t)} + A_i^*(r)e^{-i(k\cdot r-\omega t)}] \tag{4.20}$$

then the polarisation will have, as well as several other terms one of the form

$$P^{(3)} = \frac{3}{4}\varepsilon_0\chi^{(3)}A_1A_2A_3^*e^{i(k_1+k_2-k_3)\cdot r} \tag{4.21}$$

Because the pump waves are counter propagating $k_1+k_2 = 0$ and the polarisation now becomes

$$P^{(3)} = \frac{3}{4}\varepsilon_0\chi^{(3)}A_1A_2A_3^*e^{-ik_3\cdot r} \tag{4.22}$$

This component of the polarisation can act as a source term for the wave, which is the conjugate of the probe beam and propagates opposite to it.

The interaction may also be understood in terms of grating formation in the medium as depicted in figure 4.5.

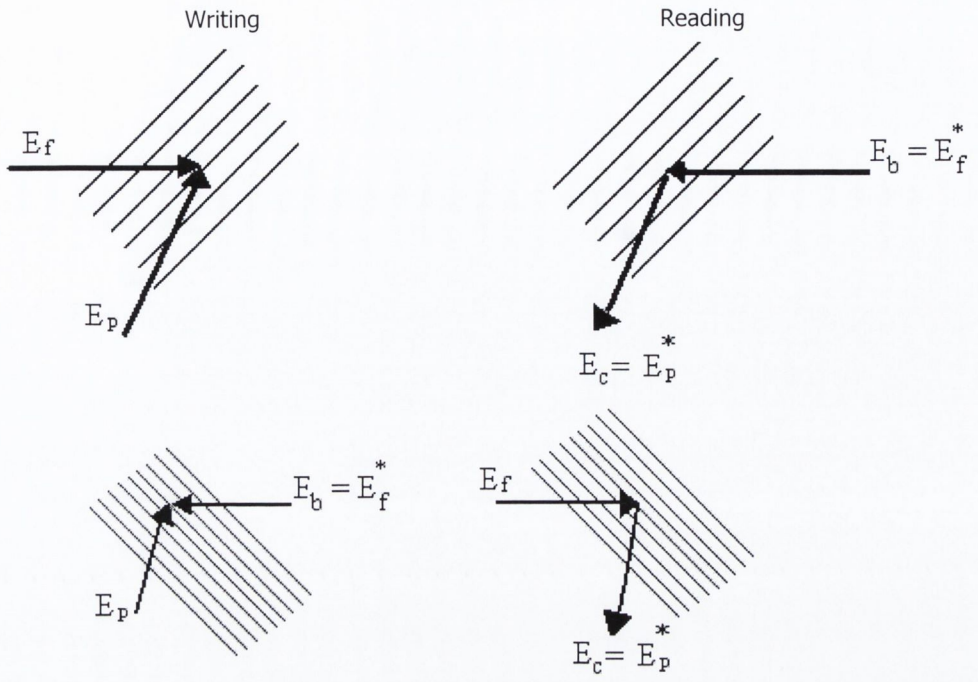

Figure 4.5 Grating formation in phase conjugate geometry. Subscripts f, b, p and c refer to the forward pump, backward pump, probe and conjugate beams

Interference of two of the beams forms a spatially varying intensity distribution, which then couples to the medium through the optical nonlinearity. This leads to a spatially varying refractive index and acts as a grating from which the remaining beam may Bragg diffract into the probe direction.

Two important gratings are formed. One of coarse pitch, formed by the forward pump and probe beams, $\lambda/2\sin(\theta/2)$, and the other formed between the backward pump and probe beams of fine pitch, $\lambda/2\cos(\theta/2)$ where θ is the angle between the forward pump and probe beams. In the case of the coarse grating the backward pump scatters into the direction of the probe beam providing the phase conjugate signal while in the fine grating situation the forward beam does so.

Degenerate Four Wave Mixing Experiment

A backward phase geometry is used as this has the advantage of being automatically phase matched and does not have the temporal range limits of other geometries. Automatic phase matching occurs when the counter propagating pump waves exactly retrace each other and have the same intensity. Under this condition the

probe wave may be aligned at any angle to the pump directions and a signal beam will be observed. An account of the set-up is now given in reference to the outline diagram shown in figure 4.6.

The Phase Conjugation experiments were carried out using the ps Nd:YAG laser. It is capable of producing pulses of energy in the region of 33 mJ at 1064 nm. The initial part of the set up cleans up the laser beam profile using an aperture in a similar manner to the Z-scan setup. The power is adjusted using neutral density filters and the polarisation is verified to be horizontal by passing it through a polariser. The beam is then directed through a half waveplate/polariser combination, which is used to control the intensity for intensity dependent measurements. In order to increase the power a telescoping arrangement of lenses are used to reduce the beam diameter and ensure the beam is well collimated. A beam splitter then divides the beam in two; one part of which becomes the backward pump beam is directed through a delay line, which enables time dependent studies. The second beam is directed around to enter the sample in the opposite direction and becomes the forward pump beam. Part of the forward pump beam is split off to become the probe beam. The probe beam is directed through a delay line, which allows for the temporal alignment and enters the sample at an angle through a cube beamsplitter. The purpose of the cube beam splitter is to maximise the intensity of the phase conjugation beam and so make the detection easier. The phase conjugate beam propagates in the opposite direction to the probe and the cubic beam splitter directs 50 % of it towards a photodiode for detection. This photodiode is placed around a 90^{o} turn and far away from the main beams. This distance and the presence of a polariser reduce the possibility of scattering interfering with the detection of the phase conjugate signal.

Alignment of the experiment involves steering the two pump beams through a series of apertures until they overlap and retrace each other's path. A perfect overlap and

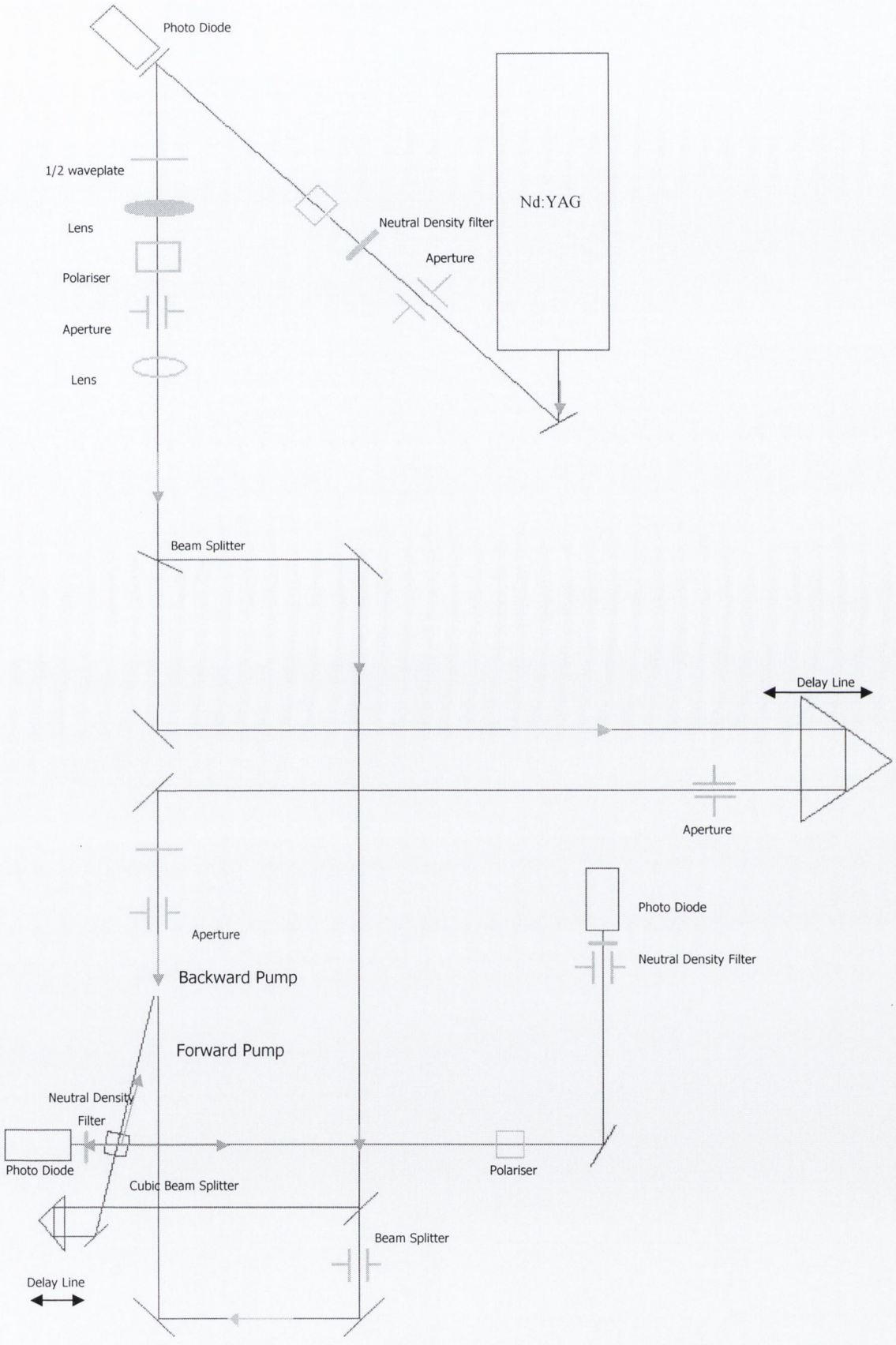

Figure 4.6 Schematic representation of phase conjugate experimental setup

counter propagation along the entire pathway of the experiment is not possible, as the beams would re-enter the laser and disrupt the lasing in the cavity. Fluorescent paper and Rhodamine 6G are useful alignment aids. In particular, the Rhodamine 6G is important in achieving temporal alignment as it two-photon fluoresces efficiently at 1064 nm. A bright green glow can be seen in a cuvette of Rhodamine 6G in ethanol and enables accurate overlap of the beams at the sample position. On moving the temporal delay a sudden increase in the brightness of fluorescence can be seen when the two pump beams are spatially and temporally aligned. This is due to the two photon fluorescence power law dependence of exponent 2. A similar procedure can be carried out for the alignment of the probe beam. As the probe beam is weaker, neutral density filters are placed in front of one of the pumps until it has a similar intensity and the other pump is blocked. The probe beam has its own delay and careful spatially and temporal adjustment, completes the input beam alignment.

In order to test for a phase conjugate signal a laser dye, A9740 (Kodak Q-Switch 1) is used, which gives a large signal. This is the same dye which is used to mode lock the laser and is an efficient saturable absorber at 1064nm. A cuvette of the Q-Switch 1 dye is placed at the sample position and a screen of white paper is placed where the output phase conjugate is expected and an Infrared Viewer is used to search for the signal. The signal usually appears as an intermittent spot among the scatter. Its presence can be verified by blocking the three beams in turn and ensuring it disappears. Also, mis-adjusting the temporal delay has the same effect. The signal is then directed into the photodiode, which is connected to an oscilloscope, for detection. The alignment can be readjusted at this point to maximise the signal output.

Measurements begin by using toluene as the sample. Toluene is the standard used in the experiment as it is the solvent used for the samples. It has a low nonlinearity and the detection of an adequate signal is difficult. Preliminary measurements involve intensity dependence measurements. A power law of exponent 3 is required to confirm that the signal is indeed third order and that scattering is not providing too much interference. Both intensity and time dependent arrangements are

computer controlled and the set-up is now ready for measurements, as long as the alignment holds.

Calculation of $\chi^{(3)}$

The magnitude of $\chi^{(3)}$ may be determined from a measurement of the reflectivity (R), (the ratio of the intensity of the phase conjugate beam I_4 to the intensity of the probe beam). In practice the determination of the reflectivity and intensities of each beam can be difficult given the many parameters such as beam quality, which need to be accurately characterised. The response of a well characterised reference material is used instead. Here we use the solvent toluene as the calibration standard which is the same reference used for the Z-scan experiments. The value of $\chi^{(3)}$ for toluene at 1064nm is taken to be $3.8\times10^{-14}\,esu$.

$\chi^{(3)}$ can be calculated by comparison using the following expression:

$$\left|\chi^{(3)}_{samp}\right|^2 = \frac{I_{Samp} n^4_{ref} L_{ref}}{I_{ref} n^4_{Samp} L_{sig}} \left|\chi^{(3)}_{ref}\right|^2 \tag{4.23}$$

where the subscripts samp and ref refer to the sample material under test and the reference material respectively.

4.2 Nonlinear Optical Characterisation of Materials

The Z-scan and DFWM techniques are employed to characterise the materials third order nonlinear optical properties. Parameters including, magnitude of $\chi^{(3)}$, nonlinear refractive index (n_2), nonlinear absorption coefficient (β), the temporal behaviour and bandwidth of the nonlinearities are determined. The objective is to establish representative parameters and general trends of the material nonlinearities to within the limits of error, rather than to carry out very precise measurements. This approach is more realistic both due to the nature of the materials involved and for the requirements of the studies undertaken in this thesis.

On considering the materials for study it becomes clear that certain aspects of their structure and the lack of an accurate knowledge of key parameters, make the precise evaluation of their nonlinearities extremely difficult. This situation is particularly

evident in the case of the nanotubes. Parameters, which are routinely used in calculations such as concentration and absorption coefficients, are not readily applicable to nanotube samples. This is due to both to the high percentages of impurities present and to the dispersion of many tube types within a typical sample. The situation is even more complex in the case of MWNT, which contain several concentric SWNT shells, which cannot be easily characterised. Here the approach taken is to calculate the volume fraction occupied by the nanotubes rather than to estimate concentration values. In the case of the set of axially substituted phthalocyanines, degradation of the samples occurs as previously detailed in chapter 3. This means that absorption coefficients and concentrations cannot be precisely specified for all the phthalocyanine materials. Material impurities are also present in the La@C_{82} sample, as a result of to the production process. These factors decrease the accuracy at which the nonlinearities of the materials can be measured. Nevertheless, on taking errors into account, values which are adequately representative for the material in question can be found.

Calculations of nonlinear optical parameters for the most part, tend to be somewhat inaccurate, unless very meticulous procedures are adopted. The variance of the literature values quoted for the same material is testimony to this[2]. There are several reasons for these discrepancies, such as use of different laser sources, techniques and sample qualities, as well as an inability to accurately determine experimental parameters. Despite the inconsistencies, the values of the nonlinear optical parameters provide sufficient information for the purpose of identifying promising materials characteristics. Hence the information given by the nonlinear optical measurements carried out here gives indicative values of the material nonlinearities and is adequate for analysis of the material attributes and the merits of their performance.

4.2.1 Review of Nonlinear Optical Properties of Organic Materials

Nonlinear optical effects have been investigated in a wide range of organic materials. Polymers were the among the first materials tested, and showed high resonant values, in the region of 10^{-9} esu and as large are 10^{-7} esu, as well as large off resonant refractive nonlinearities in the region of 10^{-11} and 10^{-12} esu[3-6]. Polymer

materials were favoured due to their good processablity, meaning that thin films and waveguides can readily be constructed, as well as their chemical flexibility which enables the incorporation of additional species such as side chains or metal atoms[7-9]. Strategies and rules for the enhancement of the nonlinear optical response in polymer systems, such as the scaling laws, have been developed. These rules predict that the linear polarisability scales with the third power of the π-conjugation length, and the second hyperpolarizability scales with the fifth power of this length. The nonlinear properties of porphyrins, phthalocyaines and squarines continue to receive attention[10,11]. These molecules are highly chemically flexible and provide model systems for the study of nonlinear optical effects[12,13].

Fullerenes, in particular C_{60}, have been extensively studied showing reasonably high nonlinearities which are in the region of 10^{-11} esu at off resonant wavelengths[14,-17]. While polymeric materials possess hydrogen atoms and are therefore characterised by residual infrared absorption due to overtones of C-H stretching vibrations, fullerenes on the other hand, while also possessing a large number of conjugated π electrons, are uniquely composed of carbon atoms and therefore do not have any residual infrared absorption. Similar to the trends found in polymers, increased cage size has been shown to enhance fullerene nonlinearities[18,19]. Endohedral doping and has also been successful in increasing the fullerene response, with increases upto three orders of magnitude found in the case of $Er_2@C_{82}$[20-22]. Scaling up even further, the nanotubes present as ideal nonlinear materials, with theoretical calculations predicting very high nonlinearities[23-25]. Initial measurements show promising results[26,27].

4.2.2 Endohedral Metallofullerene La@C_{82}

La@C_{82} is examined over a broad wavelength range using the shorter pulse width lasers. In the case of picosecond Z-scans, the laser power used was of the order of 22μJ and the beam waist was between 15μm and 25μm. For longer pulsed measurements, slightly higher input powers were used. Both the Z-scan and DFWM techniques were used and measurements were performed in solution using a highest concentration of 3×10^{-4} M. DFWM investigations were carried out at 1064 nm with the main objective being to study the temporal behaviour of the nonlinearity.

Z-scan

Z-scan results for $La@C_{82}$ taken at 532 nm using 25 ps pulses is shown in figure 4.7. The theoretical fit used has been described in detail in section 4.11. These fits confirm the third order nature of the induced nonlinear response in the case of both absorption and refraction.

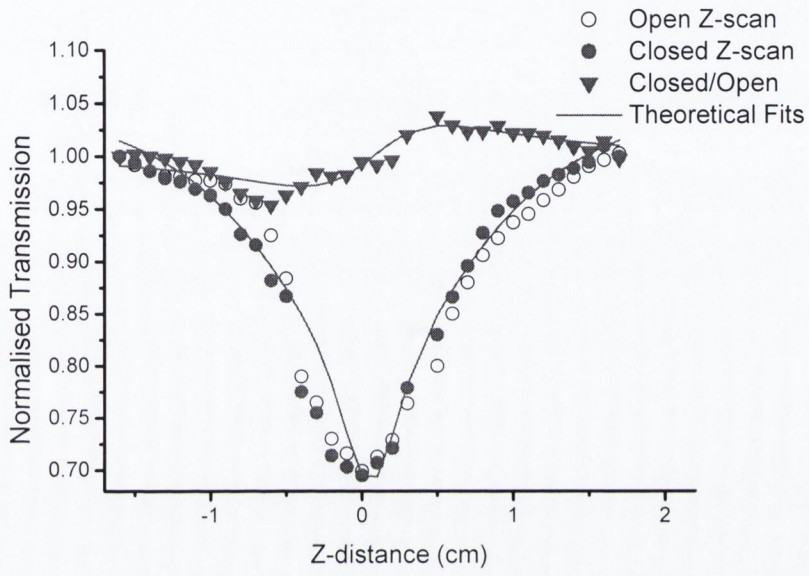

Figure 4.7 Z-scan of $La@C_{82}$ using 25 ps pulses at 532 nm

The Z-scan is dominated by a strong reverse saturable nonlinear absorption signal while only a weak nonlinear refractive signal is observed. The signal for the refractive nonlinearity is found by dividing of the closed signal by the open to remove the influence of the nonlinear absorption. The refractive signature appears to be a dip followed by a peak, which is the same sign as that of the solvent. Noise in the data is due to the instability of the laser, however the signals are sufficiently clear. The theoretical fits can be improved be increasing the number of data points measured. The weak nature of the refractive nonlinearity is expected from the Kramer Kronig relations, which describe the transfer relationship between the real and imaginary components of the optical susceptibilities. This implies that in the case of a strong imaginary response the corresponding refractive response will be weak. Further insight into the sign of the refractive nonlinearity can be gained from concentration dependent studies taken on the same laser system at 1064 nm.

Examples of the refractive Z-scan signature for different concentrations are shown in figure 4.8.

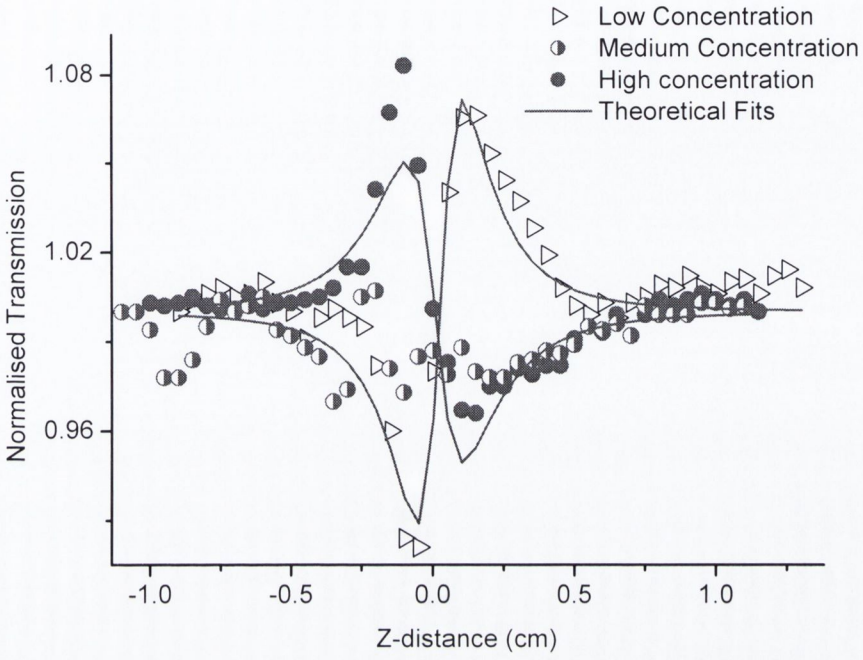

Figure 4.8 Refractive Z-scan dependence of $La@C_{82}$ on concentration at 1064 nm

At low concentrations a positive signature results, indicating that the solvent dominates the signal. On increasing the concentration of the $La@C_{82}$ the refractive nonlinearity of the solution disappears, indicated as the half open circles on the graph. A further increase in concentration gives rise to a negative refractive nonlinearity. This pattern suggests that the refractive nonlinearity of $La@C_{82}$ is negative, which is in keeping with the trend for fullerenes.

Considerable reverse saturable absorption behaviour is also observed in $La@C_{82}$ at 1064 nm as can be seen from the plot in figure 4.9. This plot shows the open Z-scan behaviour for a range of concentrations. The nonlinear absorption shows a clear dependence on concentration with the strongest absorption occurring at high concentrations and the weakest at low concentrations as indicated by the arrow.

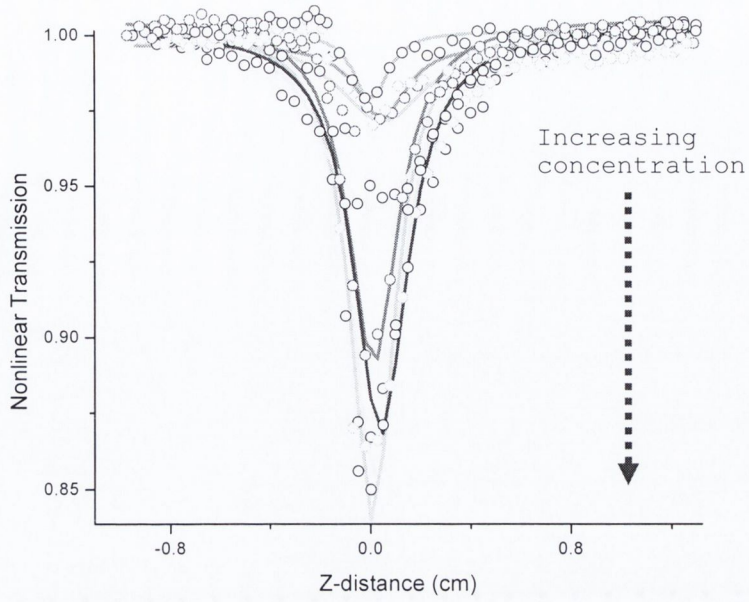

Figure 4.9 Concentration dependence of La@C_{82} nonlinear absorption at 1064 nm

Z-scan results using the 500 ps wavelength tunable laser system are now presented. Measurements taken at 524 nm are shown in figure 4.10. A negative nonlinear refractive index is observed in addition to reverse saturable absorption. At this wavelength the refractive response is relatively large while the reverse saturable absorption is notably weaker.

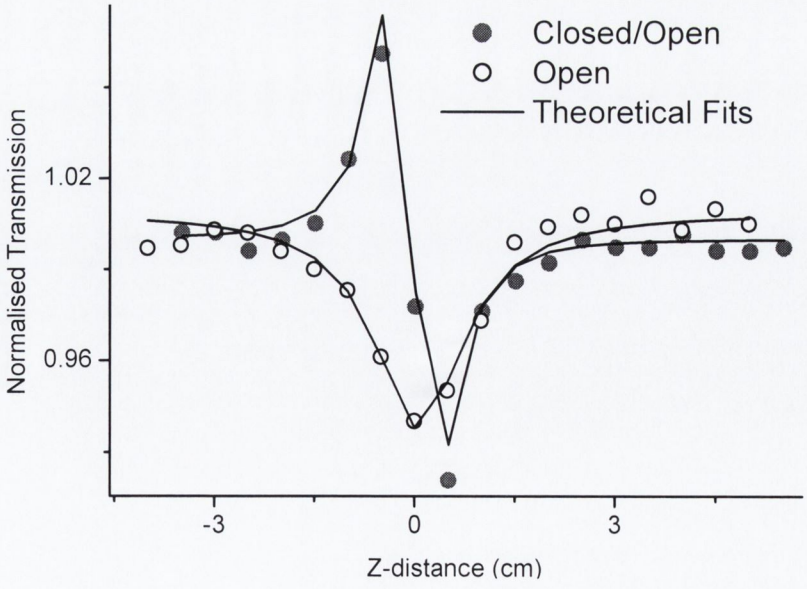

Figure 4.10 Open and Closed Z-scan results for La@C_{82} at 524 nm

The pattern continues at 563nm as seen in figure 4.11. Z-scan results show the reverse saturable absorption becomes more dominant at this wavelength.

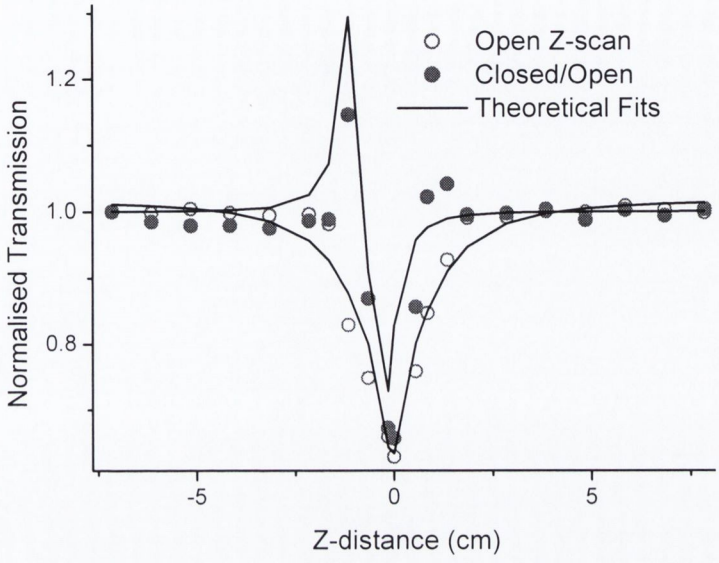

Figure 4.11 Z-scan results for La@C_{82} at 563 nm

Reasons for the variation of the nonlinear response of La@C_{82} with wavelength, can be found by examining its linear absorption spectrum, given in figure 3.1, and also shown in an adapted form in figure 4.12. The basic profile of the absorption spectrum consists of strong absorption bands at shorter wavelengths up to about 550 nm and a broad tail that continues out into the near infrared. Many shoulders, dips and peaks exist throughout. In regions of strong linear absorption, saturable nonlinear absorption tends to influence the material response. This behaviour can counteract the reverse saturable absorption behaviour of a material.

A summary of the results obtained for La@C_{82} are shown in figure 4.12. This shows the wavelength dependence of the real and imaginary $\chi^{(3)}$ values against the linear absorption background. A B-spline function has been fitted which is intended just as a guide to the eye. The spectral region has been adjusted to highlight the wavelength range of interest. The strongest reverse saturable absorption for La@C_{82} was measured at a wavelength of 563 nm, which lies within a dip in the tail region of its linear absorption. The weakest reverse saturable absorption was measured at a wavelength of 524 nm, which has the highest linear absorption

coefficient of the wavelengths at which measurements were taken. Further out towards the end of the absorption tail at 1064 nm, reverse saturable absorption of reasonable strength is measured. At such a low absorption coefficient, there can be no involvement of saturable absorption behaviour.

This interpretation is supported by nonlinear absorption measurements taken on both $La@C_{82}$ and C_{60} at 634 nm, also using 500 ps pulses. The wavelength of 634 nm lies towards the edge of the forbidden HOMO-LUMO transition of C_{60} shown in figure 2.6. In $La@C_{82}$ this wavelength lies directly within one of the distinctive peaks of the linear absorption spectrum and therefore a strong saturable absorption influence can be expected.

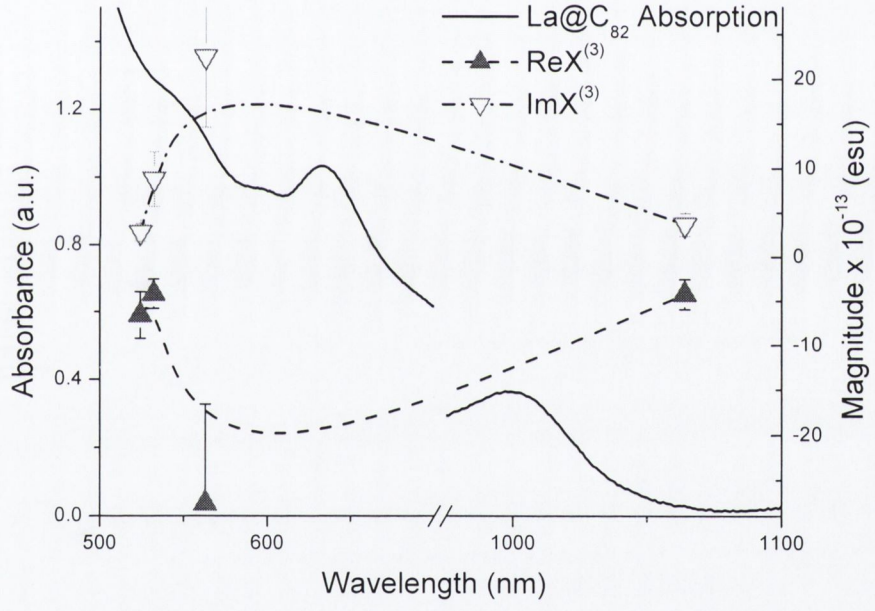

Figure 4.12 Wavelength dependence of $La@C_{82}$ nonlinearities

The results of investigations of nonlinear absorption in $La@C_{82}$ at 643 nm are shown in figure 4.13.

C_{60} is well known to exhibit reverse saturable absorption in this region of the spectrum as is seen in figure 4.13. The response of the $La@C_{82}$, however is negligible indicating that at 634 nm the saturable and reverse saturable absorption behaviour effectively cancel each other out.

The linear absorption spectrum also has implications for the refractive nonlinearity.

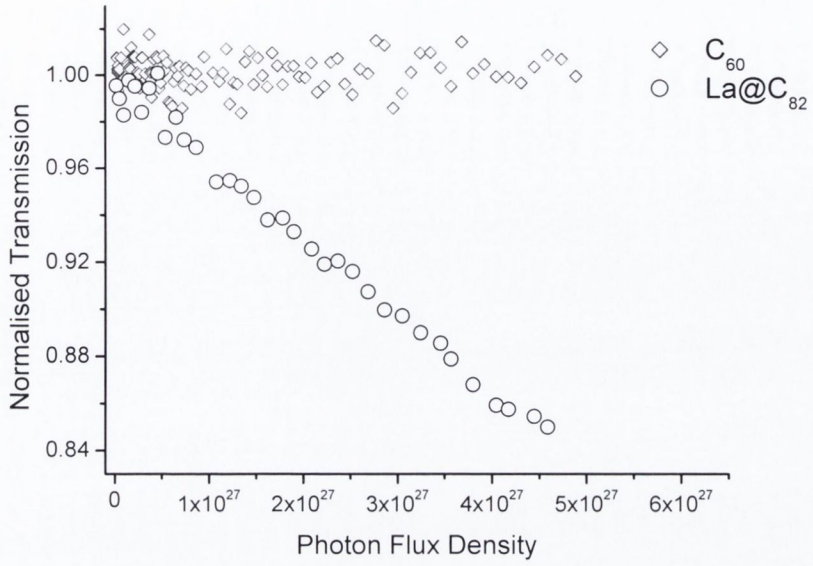

Figure 4.13 Nonlinear absorption of $La@C_{82}$ and C_{60} at 634 nm

A pattern is observed where in the case of wavelengths where reverse saturable absorption is very dominant, the entire energy of the nonlinearity is channelled into the absorptive response, where as wavelengths at which the nonlinear absorption is less dominant, a negative refractive nonlinearity can be observed.

Degenerate Four Wave Mixing Results

The third order nature of a DFWM signal is verified by a power law dependence of exponent 3 on the signal intensity. The logged intensity dependence of $La@C_{82}$ shown in figure 4.14, has a slope of 3.06 ±0.22, confirming the authenticity of the signal. The temporal behaviour of the nonlinearity is investigated by delaying the backward pump beam and recording response of the phase conjugate signal.

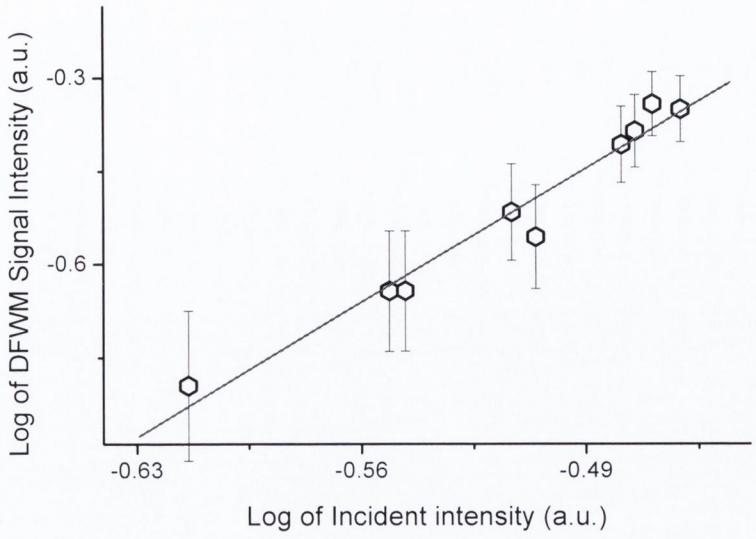

Figure 4.14 Logarithmic plot of $La@C_{82}$ phase conjugate signal with intensity

The typical evolution of the phase conjugate signal as a function of backward pump beam delay is shown in figure 4.15. A sharp peak occurs about the zero delay position, which corresponds, to an ultrafast nonlinear response.

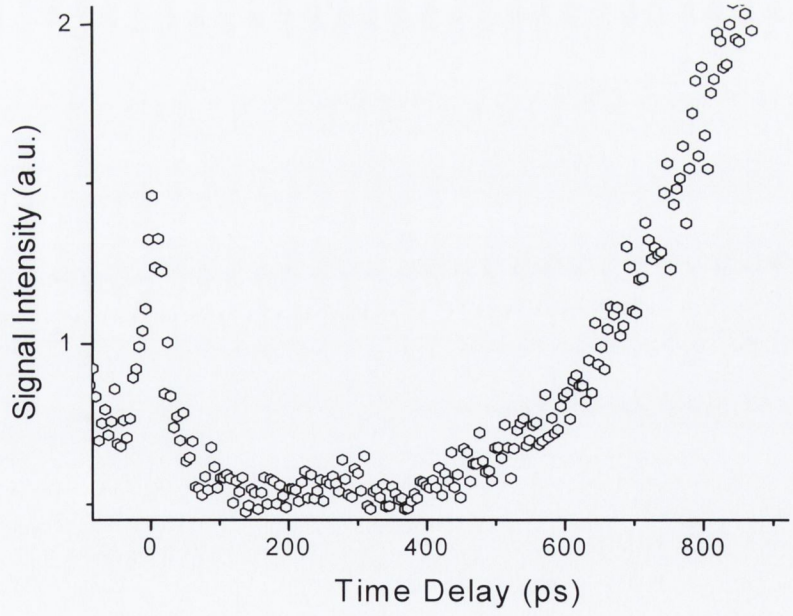

Figure 4.15 Temporal evolution of $La@C_{82}$ phase conjugate signal as a function of backward pump delay.

At larger time delays, the signal starts to build up again. This second part of the signal is likely to be thermal in origin, arising from sample absorption. The ultrafast

nature of the initial phase conjugate response is confirmed by fitting a Gaussian to the response in the region of the zero time delay position. The Gaussian fit, shown in figure 4.16, has a temporal width of 31 ps, which within experimental error corresponds to the pulse width of the laser. Therefore, the response time of this contribution to the nonlinearity is shorter than that which can be resolved by the pulse width of the laser used.

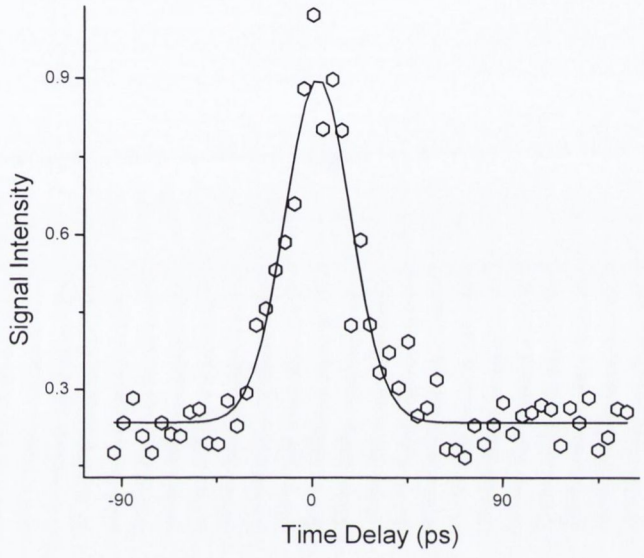

Figure 4.16 Gaussian fit to La@C_{82} phase conjugate signal at zero temporal delay

Notably only one decay component can be resolved within temporal resolution of the experiment, substantiating the ultrafast nature of the response.

Assessment of Nonlinear Optical Performance

The values of the nonlinear parameters for La@C_{82} as determined from Z-scan measurements are summarised in table 4.1. A negative real $\chi^{(3)}$ response and a positive imaginary $\chi^{(3)}$ response are seen throughout the wavelength range. The real $\chi^{(3)}$ values, (which have been corrected for the influence of the solvent) are of the order of -10^{-12} esu, which although not considerably high, is in keeping with the literature values recorded for such endohedral fullerenes[21]. The most notable feature of the nonlinear optical investigations is the observance of large positive imaginary $\chi^{(3)}$ values throughout the visible spectrum and into the near infra red

region. The large $\chi^{(3)}$ values, facilitate reverse saturable absorption which makes $La@C_{82}$ a potential optical limiting material.

Wavelength (nm)	I_0 (GW/cm^2)	$n_2 \times 10^{-6}$ (cm^2/GW)	$\Re e\chi^{(3)} \times 10^{-13}$ (esu)	Beta (cm/GW)	$\Im m\chi^{(3)} \times 10^{-13}$ (esu)
524	3.3±1.0	-0.8±0.2	-6.6±1.7	0.5±0.2	2.7±1.0
532	5.2±1.0	-4.1±0.7	-4.2±0.7	2.3±0.4	8.8±1.5
563	2.8±1.0	-1.7±0.6	-27.6±9.4	6.1±2.2	22.5±8.1
1064	10.4±1.0	-0.42±0.1	-4.3±1.0	0.9±0.1	3.6±0.4

Table 4.1 Third order nonlinear optical parameters of $La@C_{82}$

The endohedral fullerene therefore exhibits a nonlinear response which has the merits of being ultrafast, broadband and its nonlinear absorption response has potential for optical limiting purposes.

4.2.3 Carbon Nanotubes

Measurements were performed both in solution and in the solid state using the polymer nanotube composite films with a thickness in the region of 700 nm. Ideally both film and solution measurements should have been carried out at all wavelengths, however this work was carried out during the very early stages of the development of the PmPV polymer nanotube composite and hence lack of sample availability prevented this. Z-scan measurements were carried out at three different wavelengths, 524 nm, 549 nm and 639 nm from the 500 ps laser system and at 532 nm and 1064 nm using 25 ps and 35 ps pulses respectively. DFWM was carried out a 1064 nm.

Z-scan

Z-scan results taken at 524 nm for MWNT in a composite solution are shown in figure 4.17. The open Z-scan shows reverse saturable absorption with a positive refractive nonlinearity which is the dominant feature.

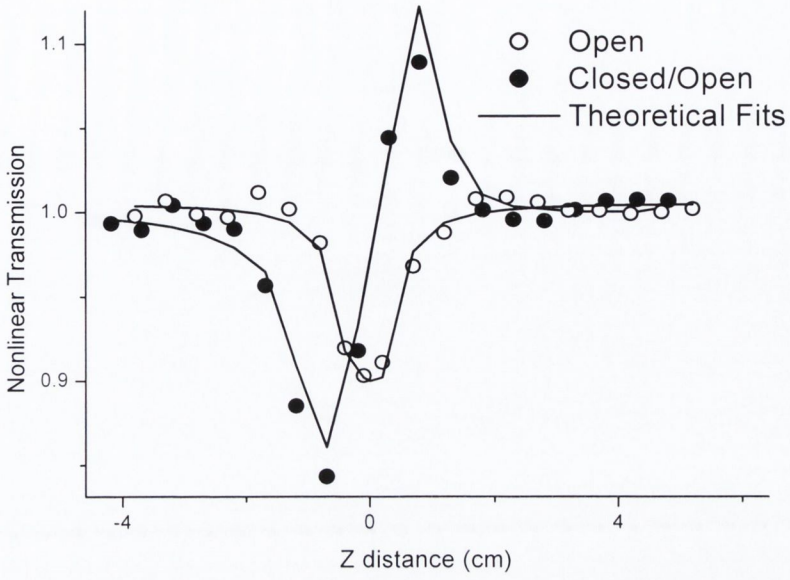

Figure 4.17 Z-scan results for MWNT composite solution at 524 nm

Z-scan results at the longer wavelength of 549 nm for a MWNT film are shown in figure 4.18. The open Z-scan shows the nonlinear absorption response to have mainly disappeared, though a hint of saturable absorption is now present. The refractive nonlinearity has now turned negative and is considerably larger.

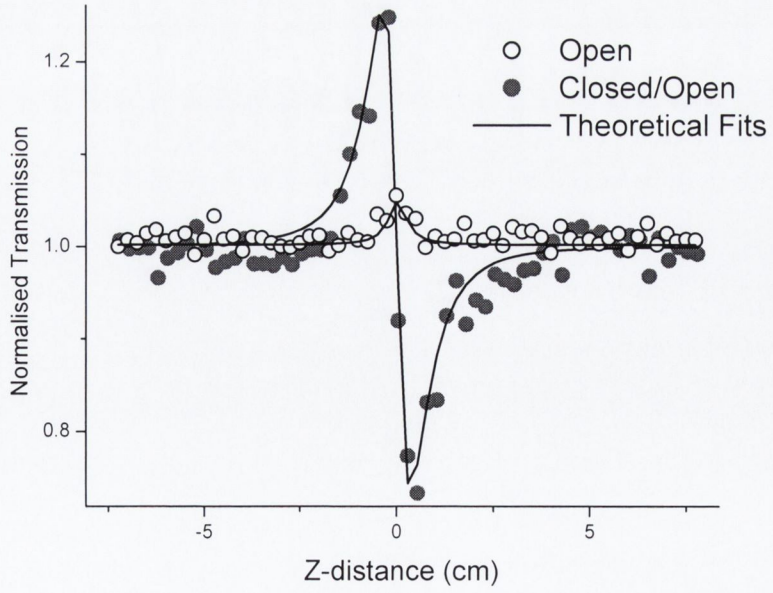

Figure 4.18 Z-scan results for MWNT composite film at 549 nm

This trend continues at 639 nm. Z-scan results at this wavelength, given in figure 4.19, show the absorptive nonlinearity to exhibit saturable absorption behaviour. The refractive nonlinearity is again negative, however it is somewhat weaker.

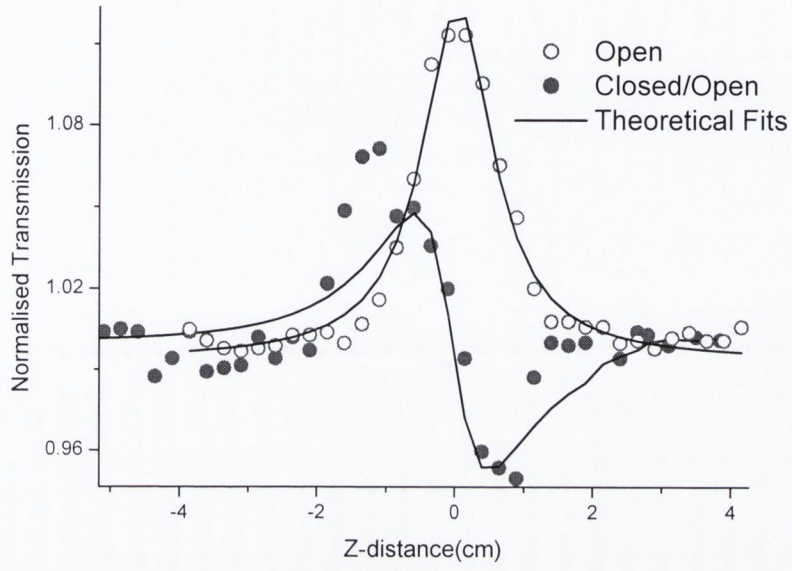

Figure 4.19 Z-scan results for MWNT composite solution at 639 nm

Z-scan measurements using the shorter pulse laser are now given. Z-scan results on a thick MWNT film (thickness ~ 1.5 μm) using 25ps pulses at 532 nm shown in figure 4.20.

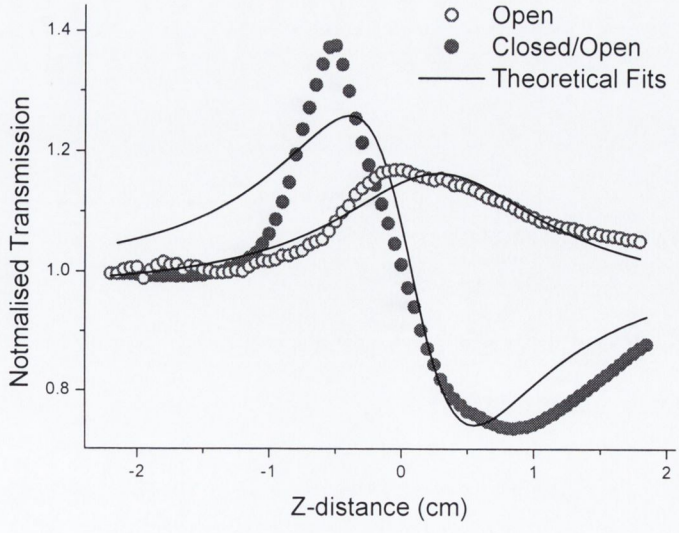

Figure 4.20 Z-scan results for 1.5 μm MWNT composite film at 532 nm

The refractive nonlinearity is negative and dominant. The open Z-scan shows clear saturable absorption of significant strength.

On comparing the very weak saturable absorption shown at 549 nm, it is important to consider the differences between solution and film measurements, and in particular given the high concentration of nanotubes present in a film of 1.5 μm. Therefore, nonlinear effects can be expected to be more pronounced in films.

Results measured at the near infrared wavelength of 1064 nm, for a MWNT film of normal thickness, are shown in figure 4.21.

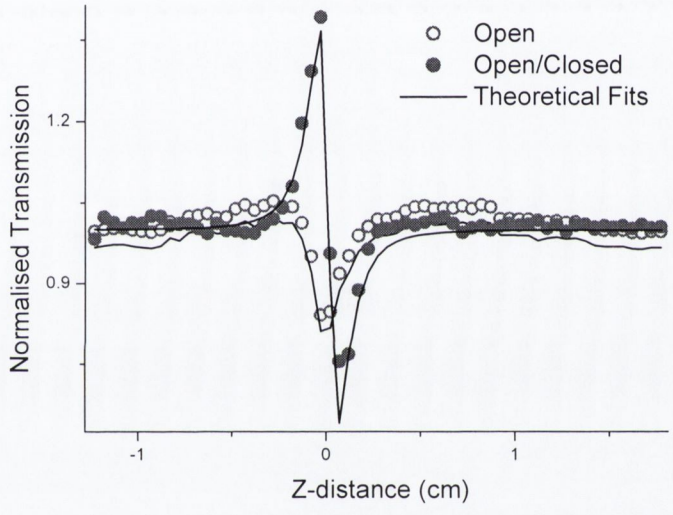

Figure 4.21 Z-scan results for MWNT composite film at 1064 nm

At this wavelength, the absorptive nonlinearity reverts back to reverse saturable absorption, which also occurrs at the shorter wavelength of 524 nm. The reverse saturable absorption is weak, and the refractive nonlinearity remains negative and is dominant.

In order to find an explanation for the trends observed in the behaviour of the MWNT nonlinearities it is useful to examine SWNT. Figure 4.22 shows Z-scan results for SWNT in SDS solution, taken at 1064 nm. Saturable absorption and a positive refractive index are observed.

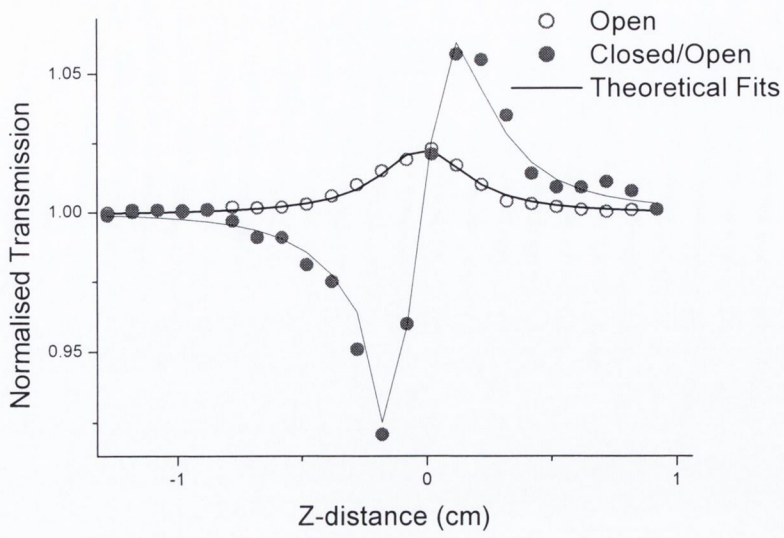

Figure 4.22 Z-scan results for SWNT in SDS solution at 1064 nm

The positive refractive index is in this case due entirely to the presence of the nanotubes as SDS solution gives no measurable signal.

The explanation of the SWNT nonlinear behaviour can be found by referring to its linear absorption spectrum, in particular the van Hove Singularity (VHS) absorption. A spectrum for VHS in SWNT is given in figure 3.16 and notably the 1064 nm wavelength lies within one of the singularity absorption peaks. The presence of appreciable linear absorption inevitably results in saturation of the absorption in the nonlinear regime and therefore accounts for saturable absorption in SWNT at this wavelength.

Using this interpretation in the case of MWNT, means that at wavelengths corresponding to strong saturable absorption, linear absorption coefficient must be larger than at wavelengths where saturable absorption is absent or reverse saturable absorption becomes evident. Linear absorption spectra in figure 3.27 and figure 3.28, show the presence of VHS in MWNT in the visible region. The position of the singularity absorption coincides very well with the nonlinear absorption pattern. When minimal singularity absorption is observed, such as at 524 nm, reverse saturable absorption occurs. Large saturable absorption occurred at 639 nm, which has by far the largest linear absorption of all the measure wavelengths.

Degenerate Four Wave Mixing

A third order response was confirmed from slopes of 3.1±0.2 obtained from logarithmic plots of the phase conjugate signal as a function of the incident laser intensity. The magnitude of $\chi^{(3)}$ was calculated with respect to the reference material toluene and using a volume fraction factor of 1.85×10^{-3}, which represents the volume of the solution occupied by the nanotubes. This approach is taken due to the difficulty in determining factor ssuch as the absorption coefficients and the type of MWNT present. Using the volume fraction estimation, a $\chi^{(3)}$ value of 1.2×10^{-10} esu was found.

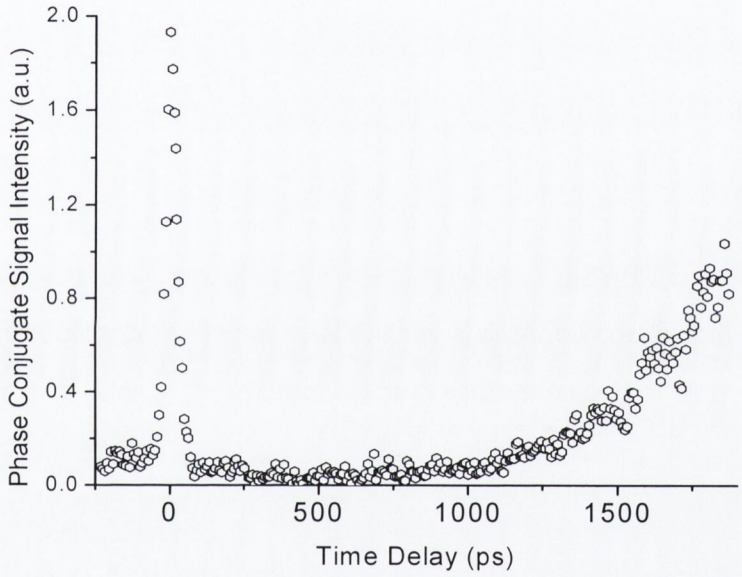

Figure 4.23 Temporal evolution of MWNT phase conjugate signal as a function of backward pump delay.

Typical temporal evolution of the phase conjugate signal, which shows an effectively instantaneous response about the zero delay position is depicted in figure 4.23. A Gaussian fit around the zero time delay position, shown in figure 4.24 has a FWHM of 38 ±3 ps, which is within the temporal resolution of the experiment given that the laser pulse width is 35 ps. Therefore, MWNT exhibit a considerable ultrafast component characteristic of an electronic contribution to the nonlinear response.

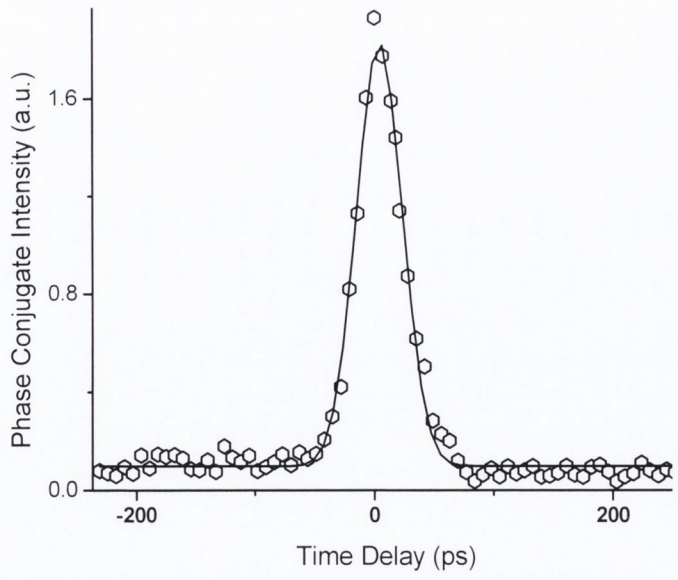

Figure 4.24 Gaussian fit to MWNT phase conjugate signal at zero temporal delay

The presence of just one component in the decay of the ultrafast contribution to the nonlinearity is confirmed by fitting a single exponential decay

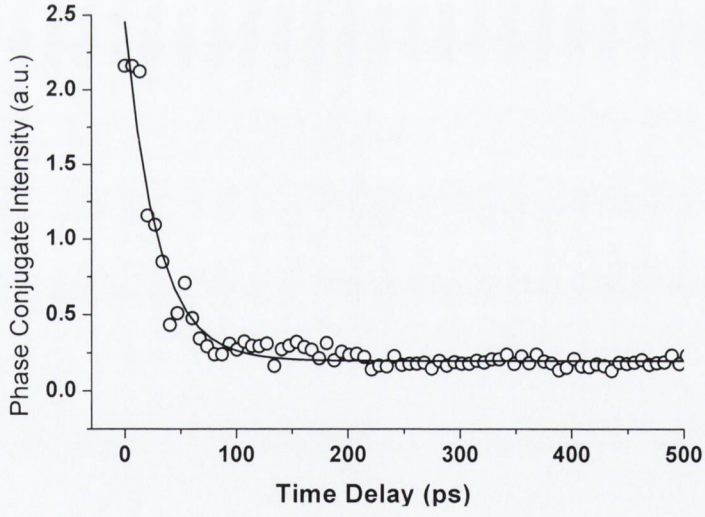

Figure 4.25 Single exponential fit to MWNT phaseconjugate decay

At longer time delays, the signal increases again to higher magnitudes as can be seen in figure 4.23. This corresponding to a large slower component. A 1 ns delay occurs before the signal begins to rise, which is significantly slower that observed in the case of La@C_{82}. However, since the time delay at which the thermal response of the phase conjugate signal arises is dependent on the angle at which the probe

beam enters the sample, no further information about the temporal properties of the material thermal response can be obtained in this case.

No measurable phase conjugate signal was observed for GP. Contributions from the polymer are not expected due to the broken conjugation from the meta linkages in PmPV. Measurements of the polymer in toluene showed signal levels of the same intensity determined for the toluene on its own.

Assessment of Nonlinear Optical Performance

The values of the nonlinear parameters for carbon nanotubes as determined from Z-scan measurements are summarised in Table 4.2. The magnitudes of both the real and imaginary $\chi^{(3)}$ values for MWNT are large, particularly in the case of solid state samples. The real $\chi^{(3)}$ values are of particular interest given the large corresponding nonlinear refractive index.

Sample	Wavelength (nm)	I_0 (GW/cm^2)	$n^2 \times 10^{-6}$ (cm^2/GW)	$\Re e\chi^{(3)} \times 10^{-12}$ (esu)	Beta (cm/GW)	$\Im m\chi^{(3)} \times 10^{-12}$ (esu)
MWNT Solution	524	5.9±1.0	$1.1\pm0.2\times10^{-1}$	2.52±0.5	1.0±0.2	0.3±0.1
MWNT film	532	6.7±1.0	$-1.5\pm0.2\times10^{4}$	$-2.2\pm0.3\times10^{2}$	$-4.3\pm0.6\times10^{2}$	$-1.6\pm0.2\times10^{2}$
MWNT film	549	2.4±1.0	-9.2×10^{4}	-1.2×10^{3}	$-6.8\pm2.8\times10^{2}$	$-2.7\pm1.1\times10^{2}$
MWNT Solution	639	5.3±1.0	-7.13±1.3	$-1.0\pm0.2\times10^{-1}$	$-4.9\pm0.9\times10^{-1}$	-0.2±0.1
MWNT Film	1064	21.8±1.0	$-3.9\pm0.2\times10^{4}$	$-6.1\pm0.3\times10^{2}$	$6.2\pm0.3\times10^{2}$	$5.3\pm1.6\times10^{2}$
SWNT Solution	1064	19.8±1.0	4.16±0.2	-5.9×10^{-2}	$-4.8\pm0.2\times10^{-1}$	-0.3±0.1

Table 4.2 Third order nonlinear optical parameters of carbon nanotubes

DFWM measurements also confirm a large ultrafast response with calculations giving values in the region of 1.2×10^{-10} esu. Values of $\chi^{(3)}$ in the region of 10^{-10} to 10^{-9} esu which arise from an ultrafast process have potential for optical switching.

In order to gain an insight into the wavelength dependence of the nonlinearity, the response of absorptive nonlinearity is analysed. In figure 4.26, β is plotted as a function of wavelength against the background of a MWNT linear absorption spectrum. The particular MWNT absorption spectrum chosen is not significant, but rather its general profile, especially the wavelengths at which the onset of absorption begins and those at which it diminishes, which are of importance. These aspects are common to all such absorption spectra, more examples of which are given in figure 3.28. The magnitude of β is not a significant feature of this plot as values for film and solution measurements vary dramatically. The point of interest is the wavelengths at which β is negative and where it becomes positive giving rise to reverse saturable absorption.

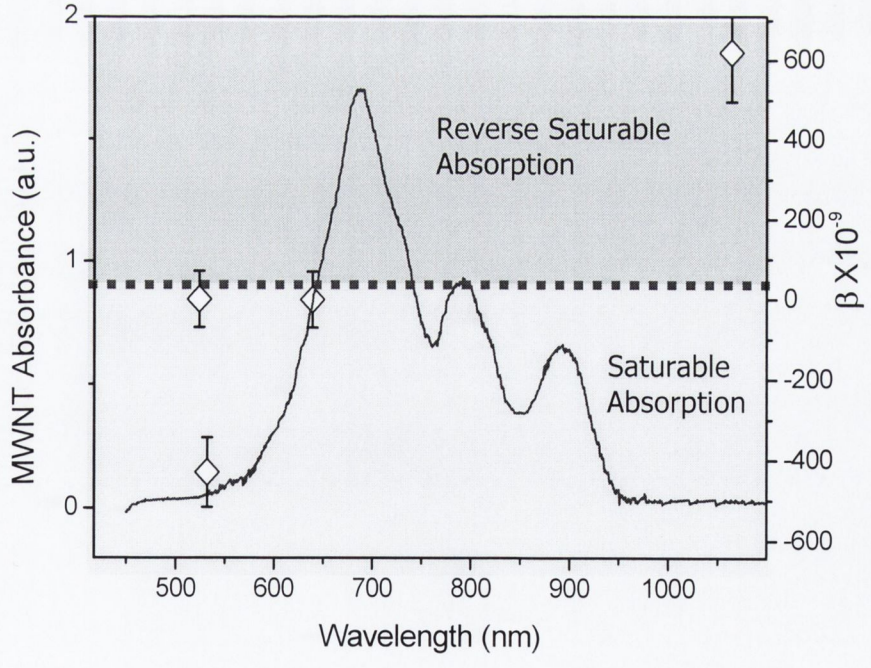

Figure 4.26 Wavelength dependence of MWNT absorptive nonlinearity

The Z-scan measurements were performed along the tail region of these MWNT van Hove Singularity (VHS). At 1064 nm which is far from the main peak, reverse

saturable absorption behaviour occurs. This is also the case for 524 nm, which is the wavelength furthest from the main peak in the short wavelength side.

In between these wavelengths saturable absorption behaviour of varying degrees is observed. These trends suggest that the absorptive nonlinear response of MWNT is dominated by its linear absorption, in particular that due to the presence of VHS.

4.2.4 Axially Substituted Phthalocyanines

Studies of the axially substituted phthalocyanines focused mainly on their reverse saturable absorption behaviour. The chemical structure and details of the linear optical properties of these molecules are given in chapter 3. The ns Nd:Yag laser was used at 532 nm was used as it is suitable since this wavelength falls within the residual absorption window. These measurements were carried out at high power in order to induce the maximum optical limiting behaviour. This means that the materials may in some cases be driven beyond a the $\chi^{(3)}$ regime in the $\chi^{(5)}$ or some other higher order nonlinear regime. The operation of a material in the $\chi^{(3)}$ regime can be confirmed by fitting with the theoretical fits described in 4.1.1.

Z-scan Results

Open z-scan results for phthalocyanine compound A are shown in figure 4.27.

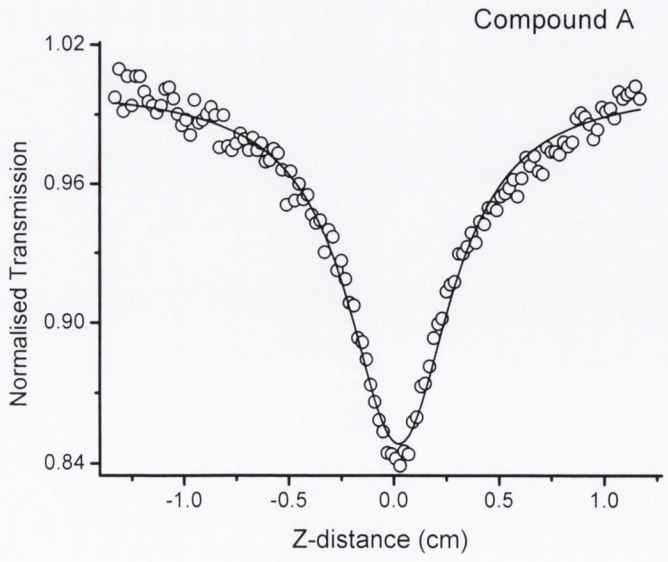

Figure 4.27 Open Z-scan results for phthalocyanine compound A

As anticipated, strong reverse saturable absorption is observed. In fact phthalocyanine compound A shows the weakest nonlinear absorption of the axially substituted compounds and is actually the only one for which the nonlinear absorption lies within the range required to satisfy the fitting conditions of the equations used to calculate imaginary $\chi^{(3)}$.

Z-scan results for phthalocyanine compound D are shown in figure 4.28.

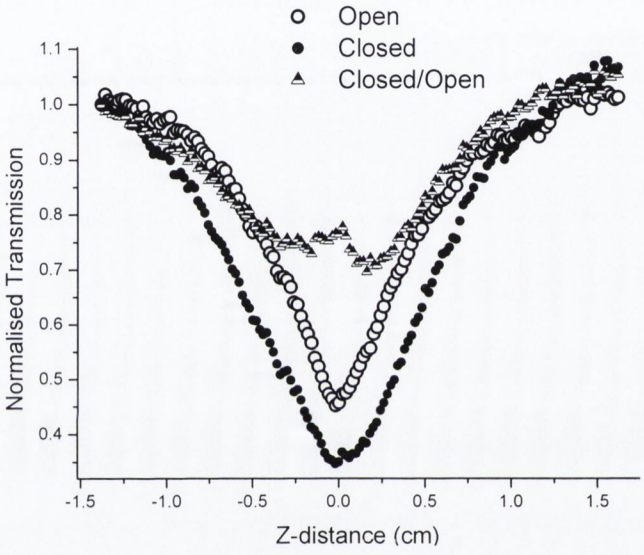

Figure 4.28 Open Z-scan results for phthalocyanine compound D

This shows both open and closed scans and the closed divided by the open to give the refractive nonlinearity. The refractive nonlinearity as expected is rather weak and the distortion is possibly due to the induction of nonlinearities of higher order that $\chi^{(3)}$. The reverse saturable absorption behaviour is, however very strong.

The open Z-scan for each of the compounds A, B C and D have been fitted as shown in figure 4.29 in order to get an indicative value for the magnitude of the imaginary third order optical susceptibility. As can been seen from the plot, a systematic increase of reverse saturable absorption occurs from compound A through to D.

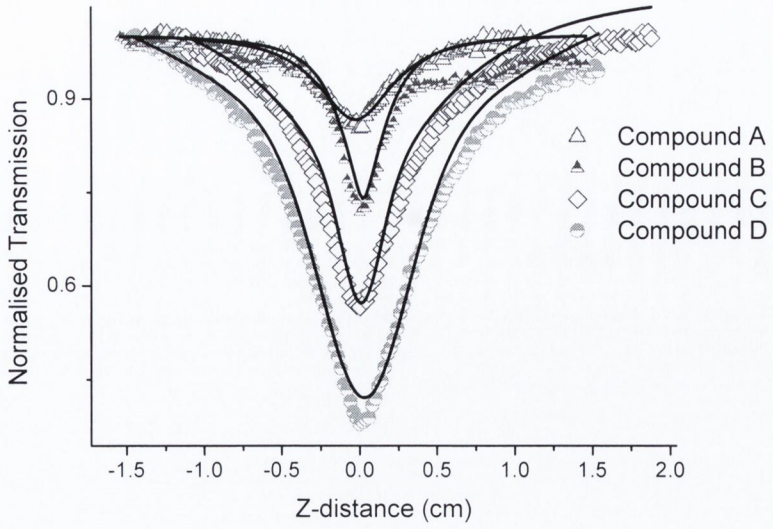

Figure 4.29 Open Z-scan fit for phthalocyanine compounds A,B,C and D

This trend is in keeping with the intentions of the molecular design.

Assessment of Nonlinear Optical Performance

Values of the nonlinear parameters obtained from the fits are given in table 4.3. These calculations are only accurate for nonlinear absorption which deviates with 20 % of the normalised values. At greater deviations the fits tend to under estimate the magnitude of the nonlinear response and hence the value of compound D in particular cannot be found using this treatment.

Sample	I_0 (GW/cm^2)	Beta (cm/GW)	$\Im m\chi(3) \times 10^{-12}$ (esu)
Compound A	0.8±0.3	5.7±2.1	2.2±0.8
Compound B	0.7±0.2	14.7±4.2	5.1±1.5
Compound C	0.8±0.3	16.6±6.22	6.3±2.4
Compound D	1.0±0.3	n/a	n/a

Table 4.3 Calculated nonlinear parameters of axially substituted phthalocyanines.

Imaginary $\chi^{(3)}$ values of the order of 10^{-12} esu are found which increase from compound A through to C, as expected from the trend seen in figure 4.29.

However, the fits fail in the calculation of values for compound D. Nevertheless, since the magnitude of the imaginary $\chi^{(3)}$ scales with the depth of the open aperture curve, and as seen from the graph in figure 4.29, compound D gives the curve of greatest depth. This may indicate that compound D has the largest magnitude and that it may be greater than 6.3×10^{-12}(esu).

Despite the fitting difficulties and the degradation problems mentioned previously, large reverse saturable absorption behaviour which is suitable for optical limiting is observed. Additionally the different magnitudes of the imaginary $\chi^{(3)}$ values observed in the molecules, suggests that the axial substituents certainly effect the material reverse saturable response. The largest response appears to be for compound D which is expected to have the largest electron withdrawing axial subsistent and correspondingly the weakest response is found in compound A which has the weakest electron withdrawing group. This trend indicates that axial substitution, using strong electron withdrawing groups can dramatically increase reverse saturable absorption in phthalocyanines.

Further investigation of the reverse saturable absorption behaviour of the phthalocyanine compounds is detailed in chapter 6 which is dedicated to the subject of optical limiting.

4.3 Designation of Material Nonlinear Optical Functions

Examination of the nonlinear optical parameters of the materials, obtained from the characterisation enables potential applications to be identified. The suitability of the materials for certain nonlinear functions is discussed.

4.3.1 Optical Limiting

The axially substituted phthalocyanines show the required reverse saturable absorption behaviour for optical limiting purposes. A variation in the degree of reverse saturable absorption between the different molecules suggests that, the axial substituents have a significant influence on the nonlinear response of the phthalocyanines in the manner intended in the molecular design. Modulation of the optical limiting performance of phthalocyanines via the incorporation of different

electron withdrawing substituents would be a very useful attribute for an optical limiting material. This is investigated in chapter 6, by examining the strength of dipole moment of the electron withdrawing groups and the efficiency of the corresponding reverse saturable absorption behaviour.

The endohedral fullerene La@C_{82}, shows a number of attributes that warrant its investigation as an optical limiting material. Temporal dependence measurements from the DFWM studies show that the nonlinear response contains an ultrafast component. The ultrafast response is further confirmed by the observance of significant reverse saturable absorption at both shorter and longer pulses. Such a fast response is desired for optical limiting materials. Another property required for optical limiting materials is a broadband response. La@C_{82}, suitably fulfils this criterion with reverse saturable absorption observed throughout the spectrum. This is a marked improvement on the performance of C_{60}, in which any significant reverse saturable absorption ceases beyond 650 nm. The spectrally broad nature of the electronic structure of the larger fullerene, and the incorporation of the heavy metal atom internal to the fullerene cage, act effectively to accomplish a broadband response. This is an important finding as in previous studies of larger fullerene molecules, reverse saturable absorption efficiencies have been found to decrease as a result of a loss of the very efficient intersystem crossing behaviour that occurs in C_{60}. Incorporation of metal atoms exohederally, were found to only marginally improve the response[28].

4.3.2 Optical Switching

Carbon nanotubes, in particular MWNT as investigated here show promise as a materials for optical switching. They exhibit large real $\chi^{(3)}$ values, with an ultra fast response time, which are key requirements for optical switching purposes. An important factor, which remains to be further investigated is the role of VHS absorption in the nonlinear refractive index of MWNT. The nature of VHS absorptions could hold the potential for the dramatic enhancement of the nonlinear response at certain wavelengths through either resonant or partially resonant multiphoton processes. Such interaction could provide very large real $\chi^{(3)}$ magnitudes, while still retaining an ultrafast response time.

4.4 Conclusions

The axially substituted phthalocyanines showed strong reverse saturable absorption at 532nm. The magnitude of the reverse saturable absorption was found to vary with the phthalocyanine axial substituent, demonstrating a definite influence of the axial substituents on the nonlinear response of the phthalocyanines. The endohedral fullerene La@C_{82} showed a negative real nonlinear component and a reverse saturable type imaginary component, which were broadband. The linear absorption was found to greatly influence the reverse saturable response with the magnitude significantly decreased at wavelengths which corresponded to a strong linear absorption feature. The carbon nanotubes showed large negative refractive nonlinearities which were as high as 10^{-9} esu in film samples. A wavelength dependent variation in the nonlinear absorption, switching from reverse saturable to saturable behaviour, was attributed to the presence of linear absorption associated with the van Hove singularities.

References

[1] M. Sheik-Bahae, A.A. Said, D.J. Hagan, T.H. Wei, and E.W. Van Stryland, IEEE J. Quantum Electron **26** *760* (1990).

[2] H. S. Nalwa, Handbook of Advanced Electronic and Photonic Materials and Devices. Academic Press, Incorporated, San Diego, 2000.

[3] R. Quinterotorres and M. Thakur, Applied Physics Letters **61** *26*, 3086 (1992).

[4] M. B. Marques, G. Assanto, G. I. Stegeman, G. R. Mohlmann, E. W. P. Erdhuisen, and W. H. G. Horsthuis, Applied Physics Letters **58** *23*, 2613 (1991).

[5] H. J. Byrne, R. Macruairi, and W. Blau, Synthetic Metals **43** *1-2*, 3217 (1991).

[6] B. LutherDavies and M. Samoc, Current Opinion in Solid State & Materials Science **2** *2*, 213 (1997).

[7] D. Y. Kim, M. Sundheimer, A. Otomo, G. Stegeman, W. H. G. Horsthuis, and G. R. Mohlmann, Applied Physics Letters **63** *3*, 290 (1993).

[8] A. P. Davey, H. Page, W. Blau, H. J. Byrne, and D. J. Cardin, Synthetic Metals **57** *1*, 3980 (1993).

[9] G. Kranzelbinder, H. J. Byrne, S. Hallstein, S. Roth, G. Leising, and U. Scherf, Physical Review B-Condensed Matter **56** *3*, 1632 (1997).

[10] H. S. Nalwa, M. Hanack, G. Pawlowski, and M. K. Engel, Chemical Physics **245** *1-3*, 17 (1999).

[11] G. de la Torre, P. Vazquez, F. Agullo-Lopez, and T. Torres, Journal of Materials Chemistry **8** *8*, 1671 (1998).

[12] G. H. Ma, L. J. Guo, J. Mi, Y. Liu, S. X. Qian, D. C. Pan, and Y. Huang, Solid State Communications **118** *12*, 633 (2001).

[13] J. S. Shirk, R. G. S. Pong, S. R. Flom, H. Heckmann, and M. Hanack, Journal of Physical Chemistry A **104** *7*, 1438 (2000).

[14] P. A. Fleitz, D. M. Brandelik, D. G. McLean, and R. L. Sutherland, Abstracts of Papers of the American Chemical Society **206**, 150 (1993).

[15] S. Couris, E. Koudoumas, A. A. Ruth, and S. Leach, Journal of Physics B-Atomic Molecular and Optical Physics **28** *20*, 4537 (1995).

[16] E. Koudoumas, F. Dong, S. Couris, and S. Leach, Optics Communications **138** *4-6*, 301 (1997).

[17] F. Kajzar, C. Taliani, R. Zamboni, S. Rossini, and R. Danieli, Synthetic Metals **77** *1-3*, 257 (1996).

[18] H. J. Huang, G. Gu, S. H. Yang, J. S. Fu, P. Yu, G. K. L. Wong, and Y. W. Du, Chemical Physics Letters **272** *5-6*, 427 (1997).

[19] H. J. Huang, G. Gu, S. H. Yang, J. S. Fu, P. Yu, G. K. L. Wong, and Y. W. Du, Journal of Physical Chemistry B **102** *1*, 61 (1998).

[20] E. E. B. Campbell, S. Couris, M. Fanti, E. Koudoumas, N. Krawez, and F. Zerbetto, Advanced Materials **11** *5*, 405 (1999).

[21] G. Gu, H. J. Huang, S. H. Yang, P. Yu, J. S. Fu, G. K. Wong, X. G. Wan, J. M. Dong, and Y. W. Du, Chemical Physics Letters **289** *1-2*, 167 (1998).

[22] J. R. Heflin, D. Marciu, C. Figura, S. Wang, P. Burbank, S. Stevenson, and H. C. Dom, Applied Physics Letters **72** *22*, 2788 (1998).

[23] Vl.A. Margulis and T.A. Sizikova, Physica B: Condensed Matter **245** *2*, 173 (1998).

[24] Rui-Hua Xie and Jiang Jie, Chemical Physics Letters **280** *1-2*, 66 (1997).

[25] R. H. Xie, Journal of Chemical Physics **108** *9*, 3626 (1998).

[26] Zhaoxia Jin, Xuan Sun, Guoqin Xu, Suat Hong Goh, and Wei Ji, Chemical Physics Letters **318** *6*, 505 (2000).

[27] M. E. Brennan, J. N. Coleman, M. in het Panhuis, L. Marty, H. J. Byrne, and W. J. Blau, Synthetic Metals **119** *1-3*, 641 (2001).

[28] J. Callaghan and W. J. Blau, Journal of Nonlinear Optical Physics & Materials **9** *4*, 505 (2000).

Chapter 5
Multiphoton Excited Luminescence from Multiwalled Carbon Nanotubes

Unexpected photoluminescence from multiwalled carbon nanotubes (MWNT) which was observed here for the first time is presented. The luminescence is believed to originate from optical transitions between van Hove singularities (VHS) in the MWNT density of states. Excitation at a wavelength of 1064 nm produced luminescence in the visible spectral region, signifying that a multiphoton process is involved. A mechanism describing the underlying processes is presented. This entails a multiphoton absorption process followed by upconversion photoluminescence, which are resonantly enhanced by VHS interactions.

Graphitic particles (GP) are used as a reference material. Comparison of the two materials serves to highlight the properties of MWNT and verify that they occur due to the nanotube structure. Carbon nanotubes are shown to possess increased nonlinear behaviour and reduced thermal response compared with graphite.

The thermal response of both MWNT and graphitic particles to the laser radiation involves the production of Planck blackbody radiation. This was observed in the near infrared region in both materials. Significantly, the MWNT exhibit lower blackbody temperatures than the graphitic particles and show a smaller temperature dependence on the radiation intensity.

5.1 Multiphoton Spectroscopy

Multiphoton spectroscopy serves to probe molecular states, which are not accessible by conventional spectroscopies and can therefore provide new information on materials. It involves populating molecular excited states by the absorption of more than one photon in any one event. Different selection rules apply than for one photon processes. For example in the case where two photons are absorbed, the excited state has the same parity as the initial state. Such a transition is forbidden for single quantum processes.

Multiphoton events can proceed by either simultaneous or stepwise absorption of photons. Simultaneous multiphoton absorption is an inherently instantaneous process, whereas a stepwise process involves a timing factor. Both processes can give rise to counter intuitive phenomena such as upconversion luminescence. Here, investigations of multiphoton processes in MWNT and GP are presented. The background to such processes in these materials is reviewed, and the affect of multiphoton excitation is discussed. The new information on MWNT revealed from these investigations is interpreted and a mechanism describing the multiphoton processes involved is proposed.

5.1.1 Luminescence Activity in Carbon Materials

Luminescence is generally not expected in carbon materials. The semi metallic nature of graphitic materials means that any induced excitations, given the absence of a band gap, decay nonradiatively through the vibrational manifold of the material. In the case of carbon nanotubes similar pseudo-metallic properties mean that luminescence activity is unexpected. One third of carbon nanotubes are metallic by nature and the small bandgap of semiconducting MWNT leaves little opportunity for luminescence.

Luminescence activity in fullerenes, in particular C_{60}, is also known to be weak. In C_{60}, optical transitions between the lowest lying electronic states are symmetry forbidden. These become partially allowed by either solid-state effects or interactions between C_{60} and the surrounding solvent molecules. The very efficient

intersystem crossing to the triplet states also strongly reduces the fluorescence quantum yield, making fluorescence virtually undetectable at room temperature.

Visible luminescence has however been reported in amorphous carbon materials[1,2]. These materials lack a defined structure and contain many deviations from the sp^2 configuration of graphite[3]. Localized states are generated as a result, introducing a bandgap into the material and enabling broadband photoluminescence to be readily induced. Carbon nanotubes are generally well graphitised and though defects may be present, these are generally few and not enough to provide a source for any significant optical activity. However, potential for optical activity in carbon nanotubes is provided by the presence of van Hove singularities in the density of states (DOS).

Optical Transitions in van Hove Singularities

Van Hove singularities are regions where the electronic states are highly concentrated. These electronic states can support optical activity. Transitions between mirror-image van Hove singularities are optically allowed[4] and create excited electronic states as indicated in figure 5.1.

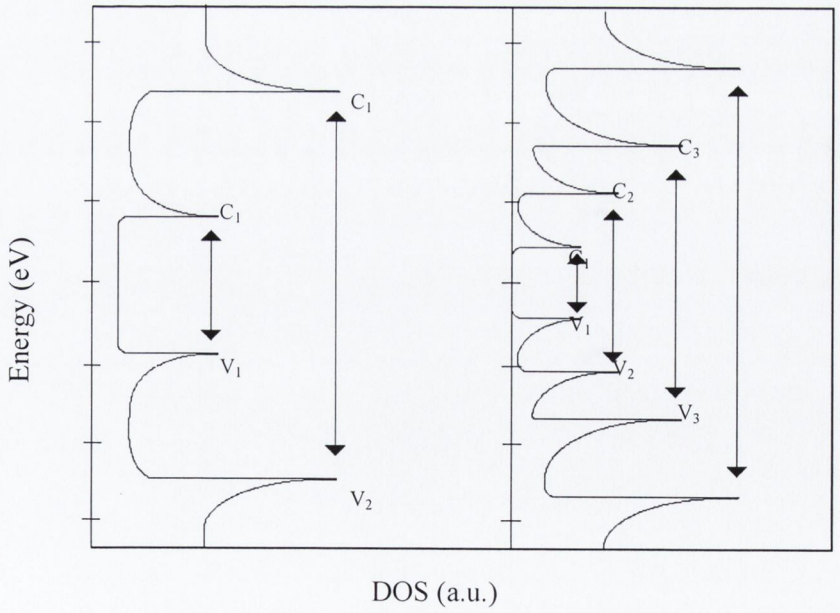

Figure 5.1 Schematic diagram of electronic density of states for (a) metallic and (b) semiconducting carbon nanotubes. Arrows indicate the optically allowed interband transitions

The interband transition energies are inversely dependent on diameter of the nanotubes and also on their chirality.

Due to the very high density of the electronic states in the region of a singularity, resonant optical transitions are expected to be greatly enhanced. This arises from Fermi's Golden Rule, given in equation 5.14, which governs the probability of an optical transition. It consists of two components, the dipole transition matrix and a factor that depends on the number of available electronic states. Given the large density of states in the region of a van Hove singularity, the transition probability will be dramatically large in the case of resonant transitions.

5.1.2 Experimental

Sample preparation and experimental procedures were performed in order to give a complete investigation of the observed phenomena. Photoluminescence spectra were recorded and intensity dependent measurements taken. The time dependence of the photoluminescence decay was also measured.

Samples

The samples used in these investigations have been described extensively in chapter 3. The main consideration in selecting samples lies in enabling the differentiation between photoluminescence originating from graphitic defect sites in the graphitic impurities that accompany MWNT, and that originating from MWNT. In order to do this, unpurified MWNT, purified MWNT and graphitic particle (GP) samples are prepared. A comparison of the photoluminescence spectra for each material will allow the influence of the graphitic impurities to be resolved.

Two types of MWNT were used; $MWNT_{Trinity}$ and $MWNT_{USA}$ as well as two types of graphitic particles, GP and KG. Also, any solvent dependence can be revealed by measurement of samples using the three different solvents; SDS, N/DMF and the PmPV polymer in toluene to form a composite. Investigations are also carried out on SWNT, however given the presence of metal particle impurities in these samples, which remain from their production process, luminescence cannot be readily observed in SWNT.

Experimental Set up

Photoluminescence (PL) measurements were performed using a focused Gaussian beam from a Nd:YAG laser operating at 1064 nm. The pulse-width was 35 ps and the repetition rate was low at just 10 Hz, which helped to minimize thermal effects. The input intensities were varied using a half waveplate and polarizer combination and intensity values were recorded using a reference photodiode. The emission was collected at right angles to the sample and directed into an Oriel 77400 spectrometer connected to an Andor B401-UV CCD detector. An incident intensity range of 0.1-10 GW/cm^2 peak power was examined. A schematic diagram of the set up is shown in figure 5.2.

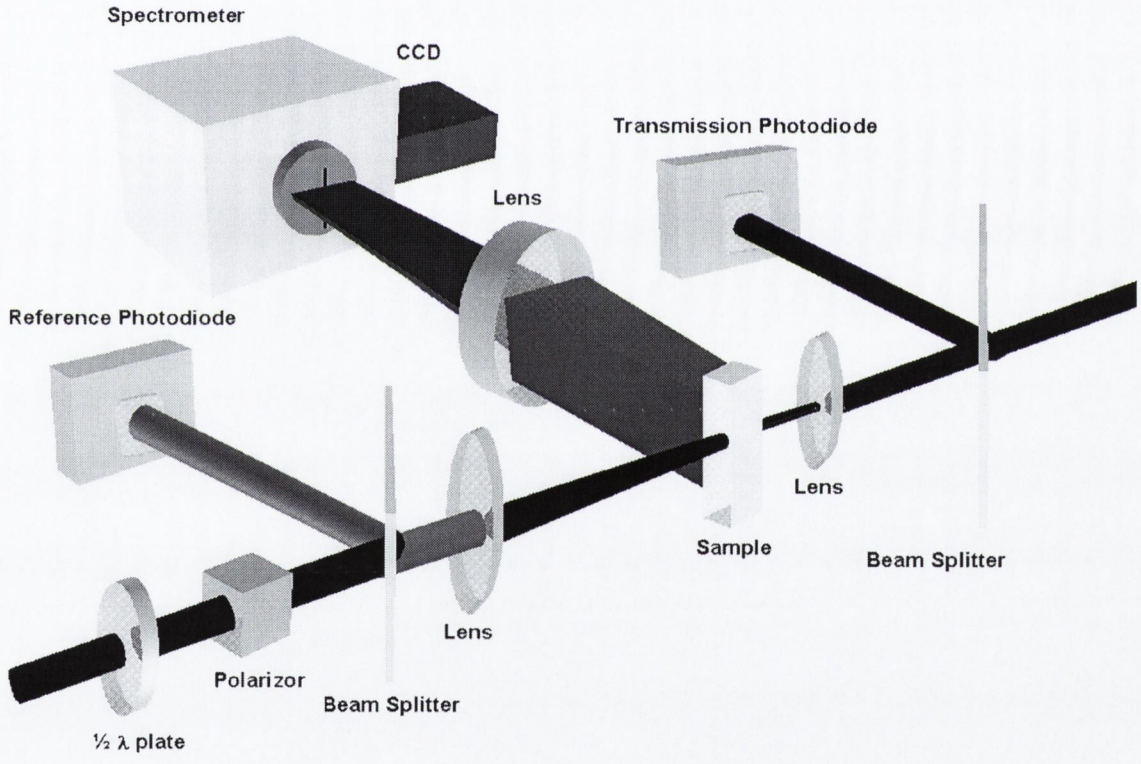

Figure 5.2 Schematic of multiphoton spectroscopic set-up

The temporal response of the photoluminescence was measured using a BPX 65 fast photodiode, which had a rise time of 4 ns. The temporal profile of the laser pulse measured using this fast photodiode is shown in figure 5.3. The temporal measurement of the pulse shows a non ideal pulse profile with ringing before and

particularly after the pulse duration. This is mainly due to the action of the diode and may cause some difficulty in the interpretation of the temporal measurements of the sample. In the case of the samples, a filter was used to remove wavelengths longer than 750 nm ensuring that blackbody radiation was removed.

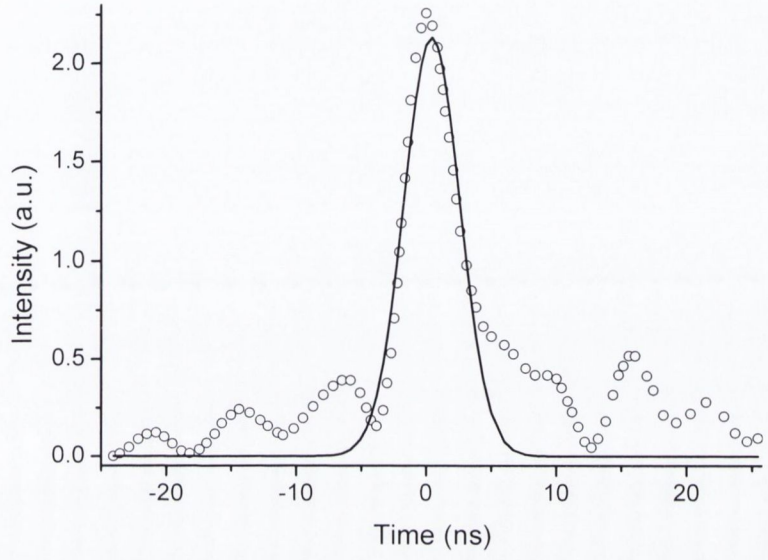

Figure 5.3 Temporal profile of laser pulse using BPX 65 fast photodiode Straight line shows a Gaussian fit with a FWHM of 4.3 ns

Rhodamine 6G was used as a reference material to verify the set up. Two absorption and upconversion fluorescence of the Rhodamine 6G dye is well known at 1064nm[5]. Intensity dependent studies showed a power law dependence of exponent 2, confirming the accurate operation of the setup and subsequent calculations. Also, the temporal decay of the up converted photoluminescence is known to be in the region of 4 ns.

5.1.3 Multiphoton Excitation of Multiwalled Nanotubes

The response of the various MWNT to intense laser irradiation at 1064 nm is detailed.

Photoluminescence

Stable visible photoluminescence was observed from all MWNT samples as shown in figure 5.4. The photoluminescence spectrum, consists of a single broad

shouldered feature, which peaks in the 780 nm region. Gaussian deconvolution reveals several distinct peaks at 621 nm, 665 nm, 757 nm, 814 nm, 849 nm and 901 nm.

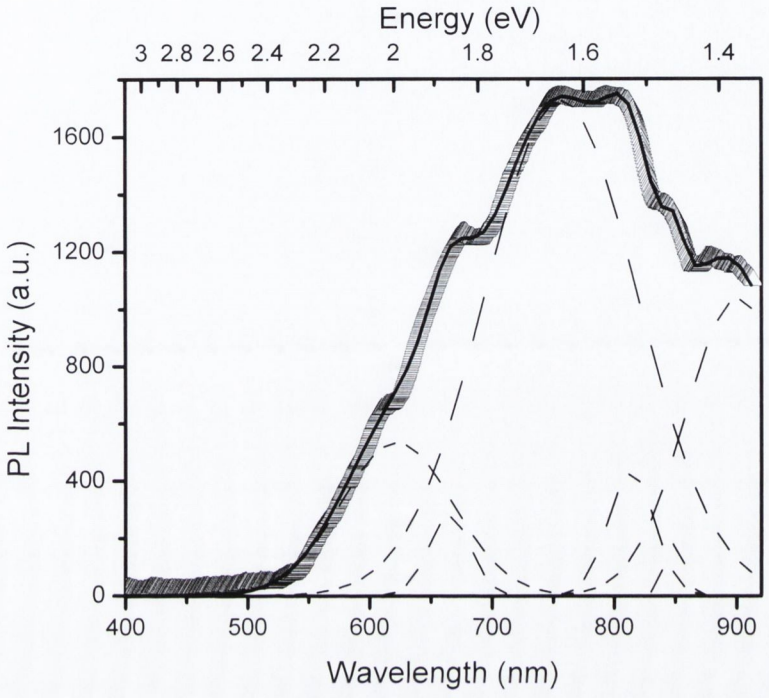

Figure 5.4 Photoluminescence spectrum of MWNT excited at 1064 nm. Dashed lines show Gaussian deconvolution of spectrum

Both $MWNT_{Trinity}$ and $MWNT_{USA}$ samples gave the same spectrum and were found to be independent of the solvent used. Significantly, both the purified and non-purified MWNT solutions showed the same features. This indicates that the graphitic impurities have a negligible contribution to the observed photoluminescence.

Nonlinear Response of Photoluminescence

Photoluminescence of energy higher than the incident photon energy typically results from a multiphoton absorption excitation process. Power law dependence studies can reveal if this is the case. Photoluminescence spectra were take over a range of intensities and integrated over the visible range, excluding wavelengths longer than 850nm. This is to ensure that the thermal, blackbody emission is not

included. The results were plotted on a logarithmic scale and an example plot is shown in figure 5.5.

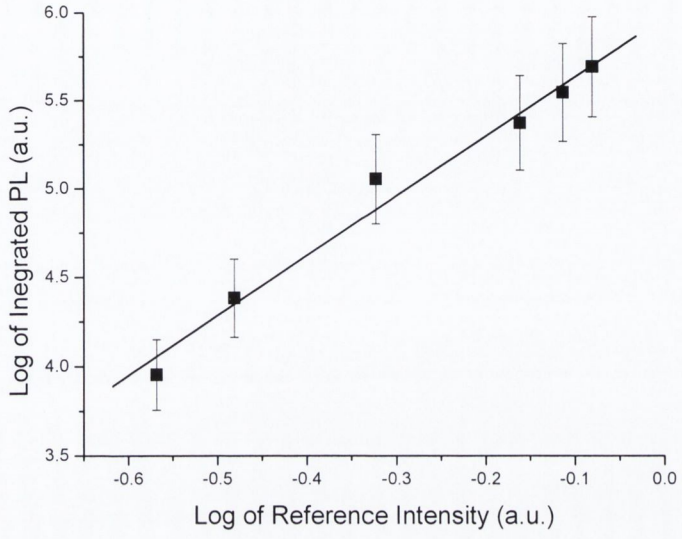

Figure 5.5 Logarithmic plot of MWNT photoluminescence as a function of intensity

These plots had a slope of 3.07±0.25 corresponding to a power law dependence of exponent 3 on intensity. This is characteristic of three-photon excitation.

Temporal Response

Temporal measurements are made with reference to Rhodamine 6G due to the peculiarities in the decay profile measured by the fast photodiode. A typical profile of the Rhodamine 6G photoluminescence decay is shown in figure 5.6. An accurate decay measurement is not possible using the information provided in figure 5.6, however it may be useful for comparison purposes. The exponential decay fits to the photoluminescence decay have decay time of the order of 8.5±0.5.

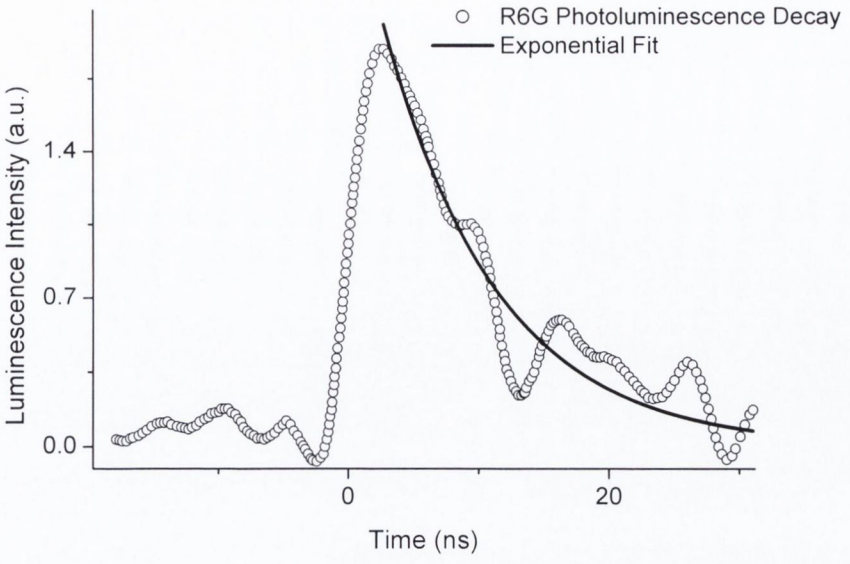

Figure 5.6 Rhodamine 6G photoluminescence decay
Straight line shows exponential decay fit with decay time of 8.5±0.5 ns

A similar temporal measurement for MWNT photoluminescence is shown in figure.5.7.

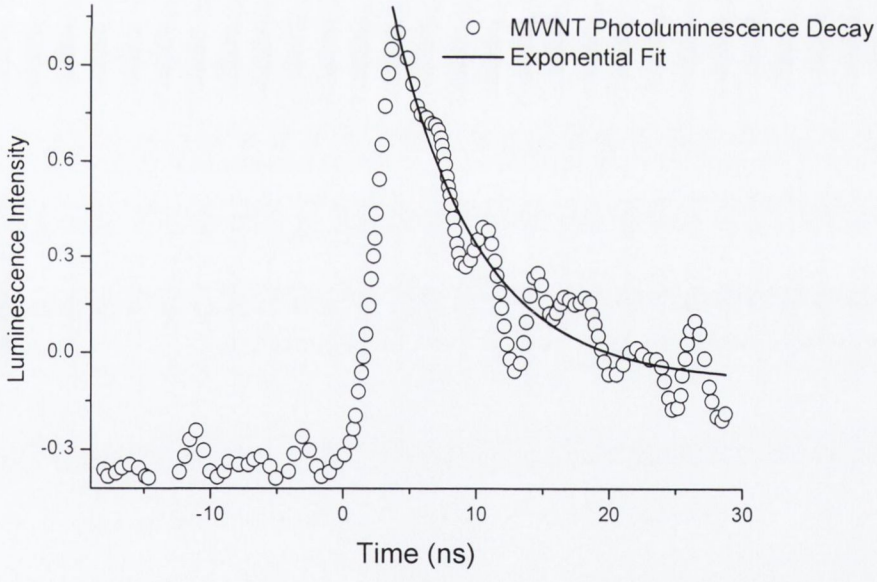

Figure 5.7 Temporal decay of MWNT photoluminescence
Straight line shows exponential decay fit with decay time of 6.3±0.5 ns

In the case of the MWNT photoluminescence decay the exponential fits the have a decay time of 6.3±0.5 ns. This is shorter that found in the case of Rhodamine 6G. These results suggest that the temporal decay of the MWNT visible

photoluminescence is somewhat faster than that of the Rhodamine 6G. This is significant since the Rhodamine 6G photoluminescence is known to result from a two photon absorption process and the similar timescale observed in the case of the MWNT photoluminescence suggest it also to be electronic in origin rather than a thermal or burning type process.

Blackbody Radiation

At the high end of the intensity range, it was noticed that the MWNT photoluminescence spectrum began to rise instead of dip in the near infrared region. This is attributed to the onset of Planck blackbody radiation. MWNT photoluminescence spectra taken at both the high and low ends of the intensity range are shown in figure 5.8.

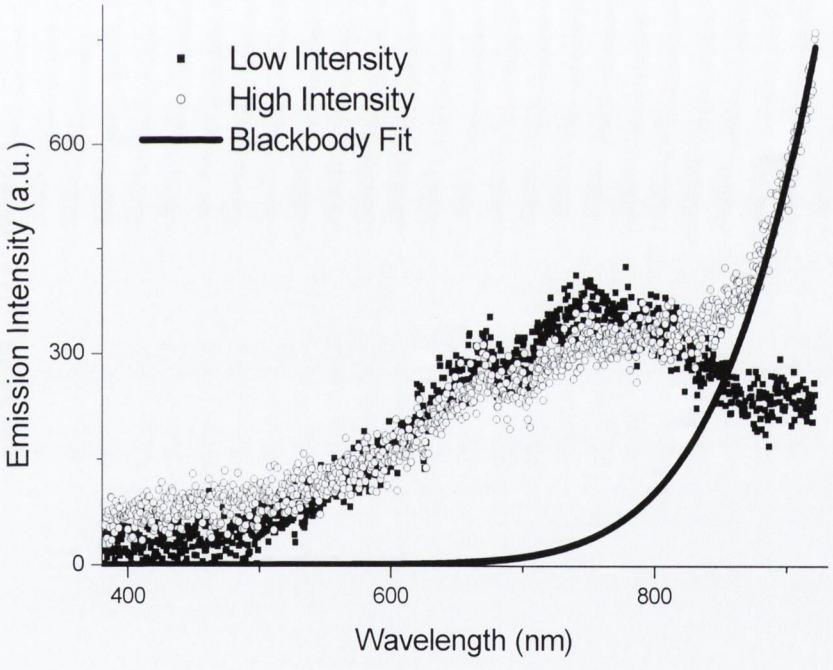

Figure 5.8 Photoluminescence spectrum of MWNT excited high and low intensity. Straight line shows the superposition of a Plank Blackbody

Note that the Planck's blackbody curve approaches the high intensity spectrum in the near-infrared region. Fitting Planck's blackbody radiation formula to the data can be used to calculate the sample temperature. Importantly the onset of

blackbody emission is the only change that occurs in the profile of the spectrum as intensity is increased.

5.1.4 Multiphoton Excitation of Graphitic Particles

The response of the various graphitic particle samples to intense laser irradiation at 1064nm is detailed.

Photoluminescence

Visible photoluminescence was also observed from GP and KGP under the same irradiation conditions. Figure 5.9 shows a typical photoluminescence spectrum, which is characterised by a broad peak at 660 nm followed by a plateau beyond 730 nm. In the near infrared region, the spectrum rises again due to the onset of blackbody emission.

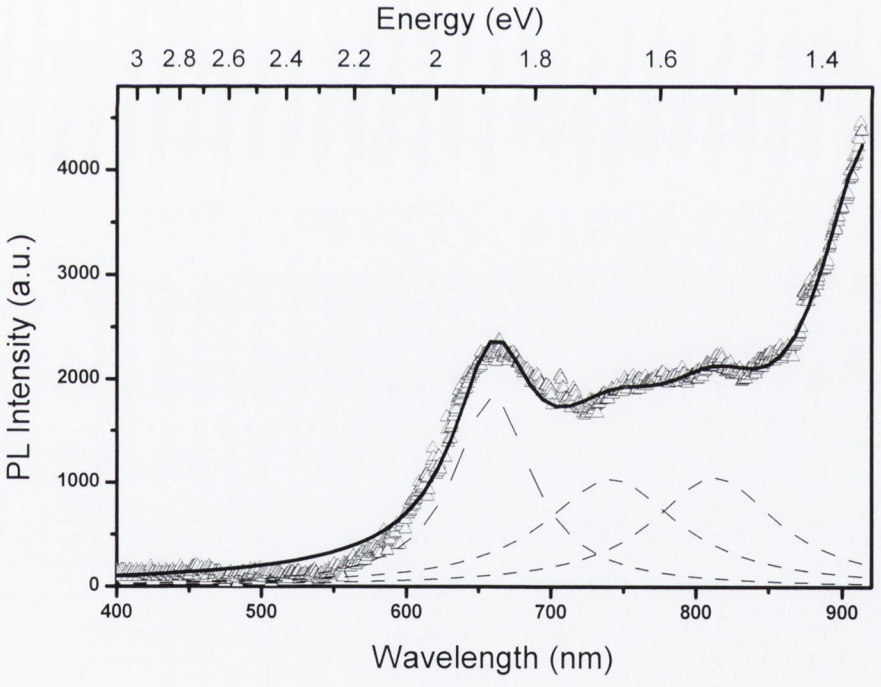

Figure 5.9 Photoluminescence spectrum of GP excited at 1064 nm. Dashed lines show Gaussian deconvolution of spectrum

Gaussian deconvolution of the spectrum shows the presence of peaks at 660 nm, 742 nm and 813 nm. No discernible differences were observed between the GP and KGP PL spectra and they were also found to be independent of the solvent used.

Nonlinear Response of Photoluminescence

Integration of the spectra is again only performed over the visible region, up to 780 nm in order to remove any significant contribution from blackbody emission. GP and KGP show an initial linear dependence with a slope of 0.98. A change to a power law dependence of exponent 2 occurs at higher intensities with a slope of 2.08±0.22 as observed in the logarithmic plot shown in figure 5.10. A linear dependence is characteristic of a thermal process while the change to a power law dependence corresponds to the induction of nonlinear behaviour in GP at a higher incident intensity.

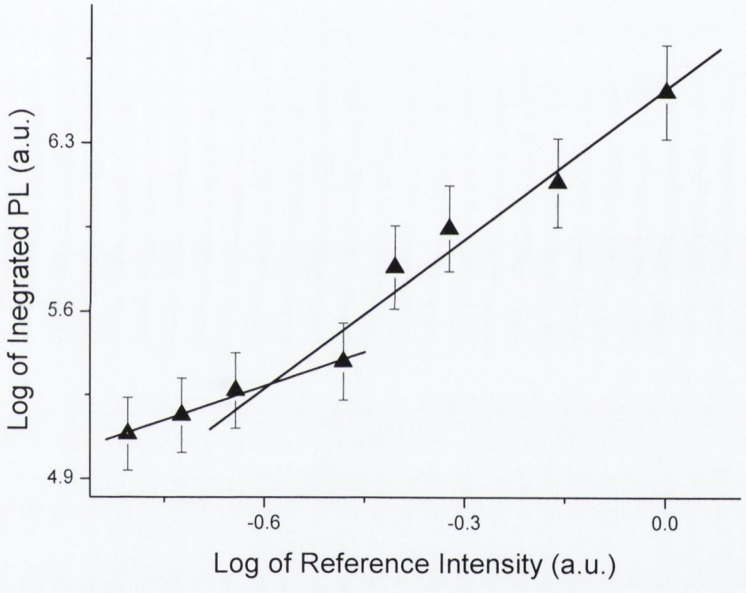

Figure 5.10 Logarithmic plot of GP photoluminescence as a function of intensity

Blackbody Radiation

Blackbody radiation is observed in all GP spectra over the examined intensity range. Blackbody emission is shown to dominate the spectrum at higher intensities in figure 5.11, with the many of the photoluminescence features being over riden.

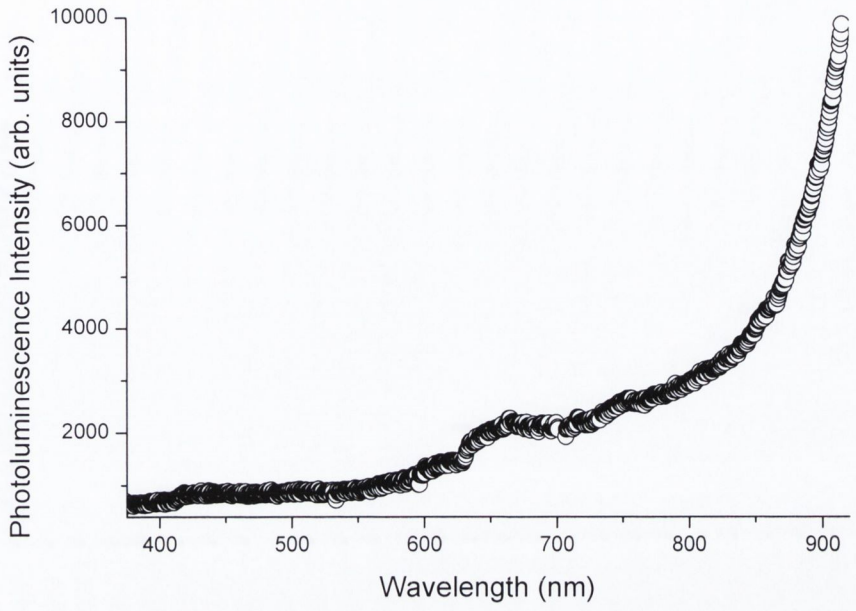

Figure 5.11 GP photoluminescence spectrum showing large blackbody radiation

The larger contribution of blackbody radiation to the GP photoluminescence spectra than in the case of the MWNT suggests that higher sample temperatures are reached in the case of the GP.

5.1.5 Comparison of Multiwalled Nanotube and Graphitic Luminescence

The profiles and relative intensity of the spectral features in the two materials differ significantly. MWNT spectra show a rise in photoluminescence from about 500 nm to a first main feature in the 665 nm region. The GP emission begins after 540 nm and rises to a clean Gaussian peak at 660 nm, which is broader and more distinctive than the MWNT feature in the corresponding spectral region. At longer wavelengths, the MWNT photoluminescence continues to rise, displaying many more shoulders and features reaching a broad maximum at around 780 nm. The corresponding spectral region sees the saturation of the GP emission until the onset of blackbody emission occurs in the near-infra red region. In MWNT the spectrum dramatically falls off beyond 900 nm the cases where no blackbody contribution is involved. Blackbody emission is observed in MWNT only at the highest end of the intensity range. These differences in the photoluminescence spectra of MWNT and

GP indicate that different electronic states are responsible for the photoluminescence in the two materials.

The most significant difference in the photoluminescence of the two materials is in the variation in their intensity dependence. GP shows an initial linear dependence on intensity, which indicates that there is a large thermal component to the photoluminescence even in the visible region. The change to a power law dependence at higher intensities confirms the presence of a definite photoluminescence process distinct from the thermal emission process. The fact that the power law has a dependence of two as opposed to the cubic dependence shown by MWNT throughout the intensity range demonstrates that the different excitation mechanisms of the luminescent states operate in the two materials. The strong cubic dependence shown by the MWNT also demonstrates their enhanced nonlinear optical response.

5.2 Thermal Processes

Thermal emission processes such as blackbody radiation are distinctive from the visible photoluminescence processes observed in these materials. Nevertheless, they play an important part in the material response to the intense laser irradiation. Here we examine a number of issues regarding the thermal activity of the materials. The first issue addressed is the vaporisation temperature of the materials and these investigations are carried out using a Thermo Gravimetric Analysis (TGA) technique. The sample temperatures reached under laser irradiation are then found by fitting blackbody radiation curves to the near infrared emission. The effect of laser irradiation on the sample stability is also examined using Raman and FTIR spectroscopy in order to determine any degradation effects in the sample. Also irradiation induced sample dissociation is also discussed

Thermo Gravimetric Analysis (TGA)

TGA is a simple technique, which monitors the mass of a sample as it is slowly heated. Here the temperature range at which the sample materials vaporise is investigated. TGA results for MWNT and GP are shown in figure 5.12.

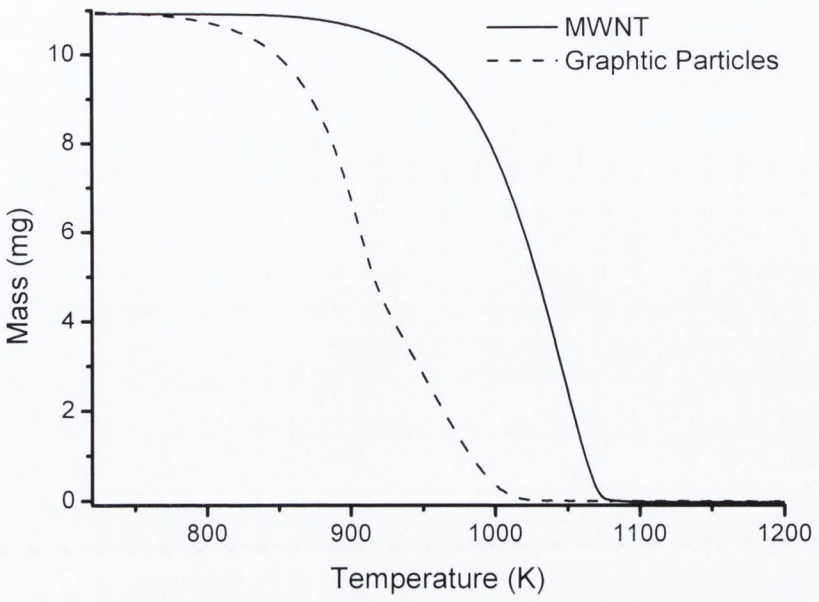

Figure 5.12 TGA of MWNT and GP

The material vaporisation temperatures can be read from the plot in figure 5.12. In the case of GP this occurs after 800 K and in the case of MWNT after 900 K. The lower vaporisation temperature of GP is understandable considering the many dangling bonds and interruptions to the graphite structure that occur in these particles. This is clearly shown in the TEM picture shown in figure 3.10. The MWNT are more unified and stable entities and therefore vaporise at a higher temperature. However the most important information from this analysis is that the sample temperatures reached on laser irradiation are far below the vaporisation temperatures, as given in the next section.

5.2.1 Planck Blackbody Radiation Temperature

Planck black body emission occurs around the 800 nm region of the spectrum in GP and in MWNT above 840 nm. Sample temperatures may be calculated by fitting Planck's blackbody formula, given in equation (5.1) to the emission intensity (I) in the near infrared region using.

$$I = \frac{2hc^2}{\lambda^5} \frac{1}{e^{hc/\lambda kT} - 1} \qquad (5.1)$$

where, h is Planck's constant, c is the speed of light, λ is the wavelength, k is Boltzmann's constant and T is the temperature.

The sample temperature (T) was left as a free parameter in the fitting process and hence its value could be calculated form the fit curves.

Examples of fitting blackbody radiation curves to the infrared emission for GP photoluminescence spectra are shown in figure 5.13. In order to eliminate interference of photoluminescence which occurs mainly in the visible region and hence to ensure a good fit, the blackbody radiation formula was only fitted in the NIR region of the spectra. The blackbody radiation curves fit reasonably well showing characteristic move to shorter wavelengths with higher intensities and hence higher temperatures.

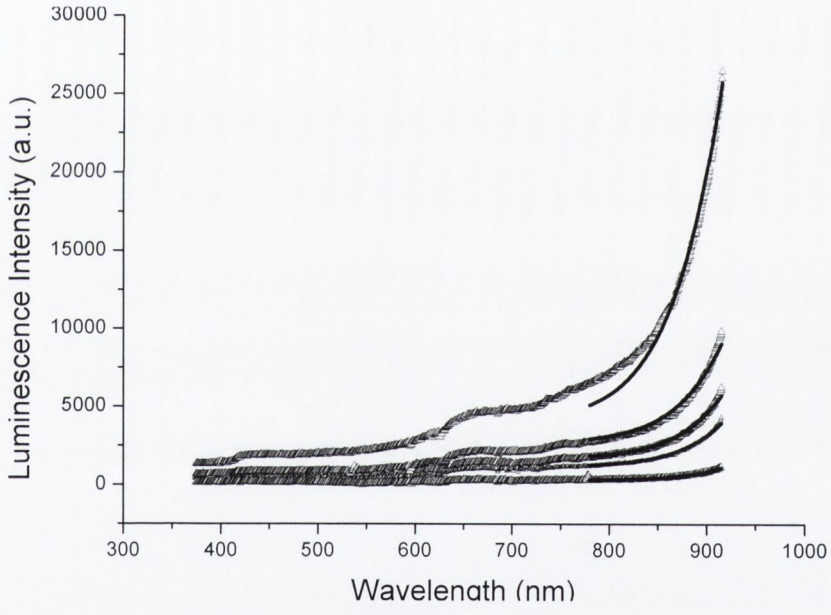

Figure 5.13 Blackbody radiation fits to GP luminescence

Calculated sample blackbody temperatures for MWNT and GP are shown as a function of incident intensity in figure 5.14.

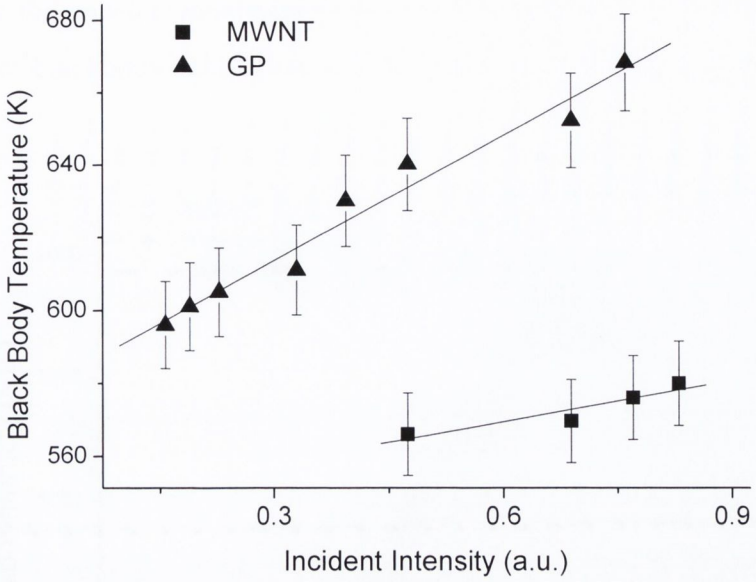

Figure 5.14 Blackbody radiation temperature calculated for MWNT and GP

It can be seen that for the same excitation intensity range MWNT temperatures are dramatically lower than those of GP. A less steep slope is also observed in the case of MWNT demonstrating a weaker thermal dependence than that of GP. These results can be understood in terms of the higher thermal conductivity of MWNT. Though thermal conductivity of inplane graphene is high, the overall thermal conductivity of graphite is low due to the poor interplane interactions, and hence also the thermal conductivity of GP. MWNT on the other hand encompass the favourable properties of inplane graphite and the large thermal conductivity serves to effectively dissipate heat and reduce sample heating. This is addition to the increased radiative decay pathways provided by the VHS account for the decreased thermal activity observed in MWNT.

In order to examine the possible influence of Planck blackbody radiation ok the scaling laws determined for the MWNT photoluminescence, the intensity dependence of the integrated MWNT spectra was repeated for a series of spectra from which Planck blackbody radiation had been subtracted. Specific criteria were used in determining suitable parameters in order to treat the case of greatest possible contribution of Planck blackbody radiation in the spectra. The MWNT spectra which were used in the determination of the original scaling law were all below 566

K. Therefore, a Planck Blackbody curve for a temperature of 566 K was subtracted from each of the spectra, maximising the area contribution to the overall spectra. An example of blackbody subtracted MWNT spectrum is shown in figure 5.15.

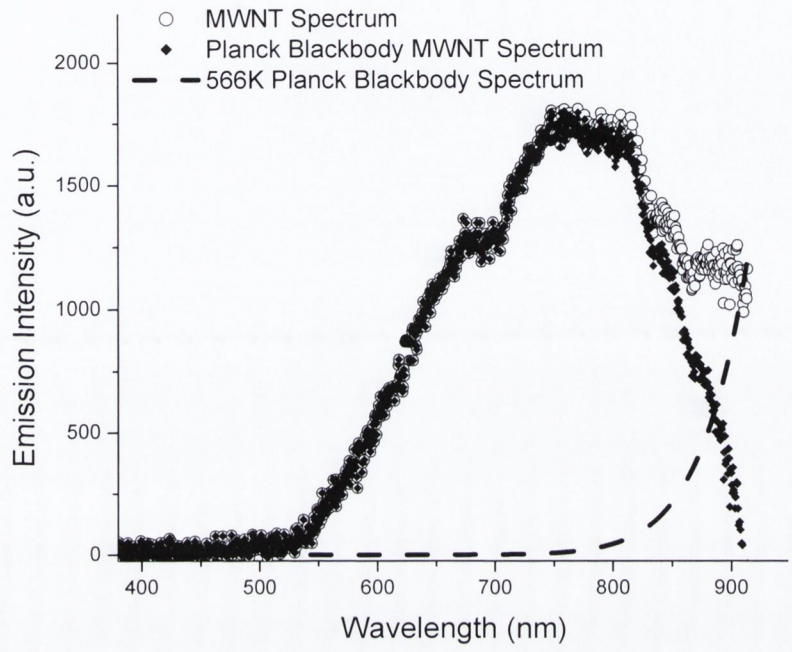

Figure 5.15 Blackbody subtracted MWNT luminescence spectrum.

From figure 5.15 it can be seen that the effect of subtracting Planck blackbody radiation is to reduce the amplitude of the contribution at near infrared wavelengths. This subtraction was carried out for a series of MWNT spectra, measured at different incident intensities.

The integration of the blackbody subtracted spectra as a function of incident intensity is shown on a logarithmic scale in figure 5.16. The linear fit has a slope of 3.17 ± 0.33, which, within the margins of experimental error, does not differ from that for the unsubtracted spectra shown in figure 5.5.

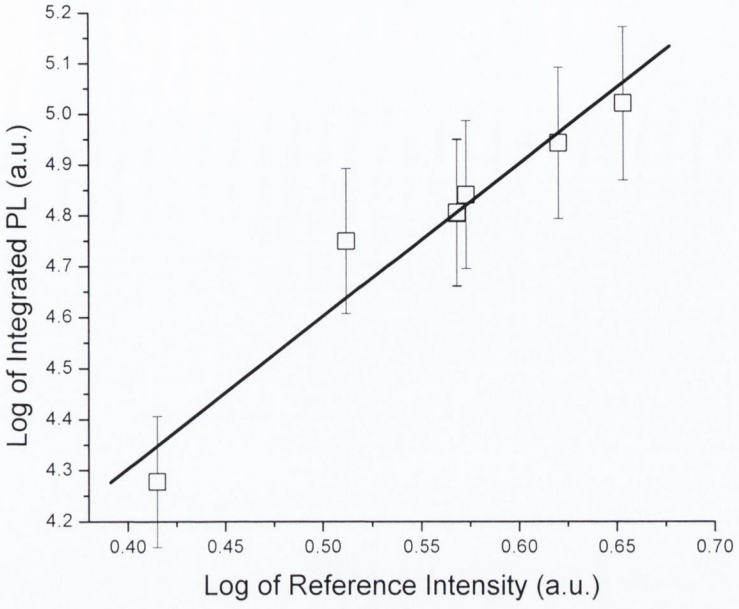

Figure 5.16 Logarithmic plot of Blackbody subtracted MWNT photoluminescence.

This result further substantiates the three photon nature of the multiphoton excitation process.

5.2.2 Effect of Laser Irradiation on Samples

The effects of heating due to laser irradiation are now detailed. Various spectroscopic methods are used to examine the before and after effect of irradiation on sample on aspects of sample condition such as stability and the possibility of degradation. Also some applications of the thermalisation effects are considered.

Sample Degradation

A useful method of examining sample degradation is absorption or in particular FTIR spectroscopy. FTIR spectroscopy provides information of the chemical bonding arrangements in materials. Inspection of FTIR spectra of before and after irradiation can reveal any damage to the material resulting from broken bonds. FTIR spectra of a polymer MWNT composite irradiated at both typical and very high intensities are shown in figure 5.17.

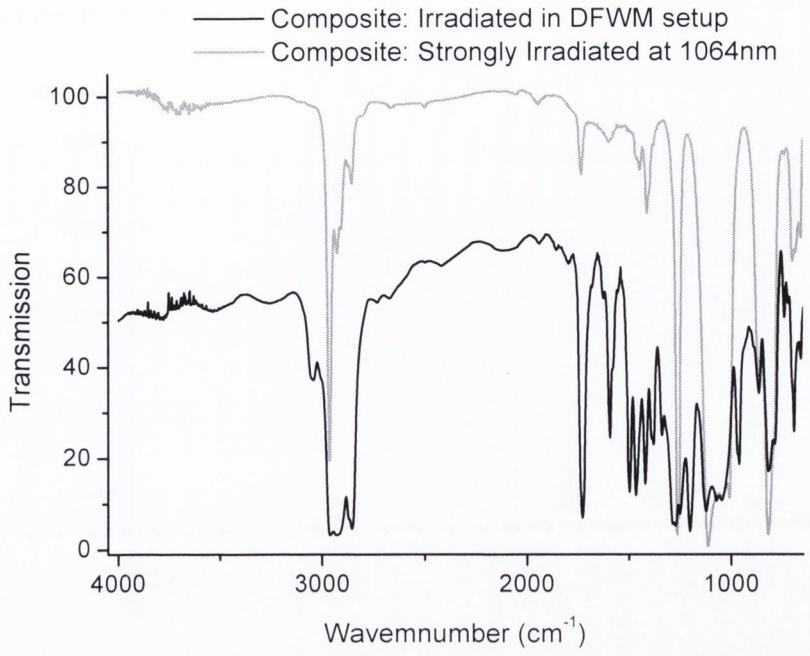

Figure 5.17 FTIR of composite irradiated at typical & very high intensities

The FTIR spectrum of the composite irradiated in the DFWM set-up is identical to that of a non-irradiated composite. This shows that under the typical irradiation conditions used in the experiments carried out here, no detectable sample damage occurs. However, the second spectrum of a very intensively irradiated composite shows significant differences to the first. Many of the absorptions characteristics of the polymer either have disappeared or are greatly weakened, particularly in what is known as the fingerprint region from 1700 cm^{-1} to 1300 cm^{-1}, indicating damage to the polymer. The sample colour was noted also to change to an orange shade. This confirms that sample damage is possible using the 1064 nm irradiation, though only at very high intensities.

As a means of checking damage to nanotubes, Raman spectroscopy is most useful. Raman spectra of before and after irradiation of MWNT showed no difference. However, a more definitive examination of carbon nanotubes is given by Raman spectra of the radial breathing mode in SWNT. It is assumed that SWNT and MWNT will respond in a similar manner to laser irradiation as regards sample degradation. An examination of the effect of irradiation on the SWNT radial breathing mode will provide information about the effect of irradiation on MWNT.

Raman spectra of the radial breathing mode of irradiated and non-irradiated SWNT are shown in figure 5.18.

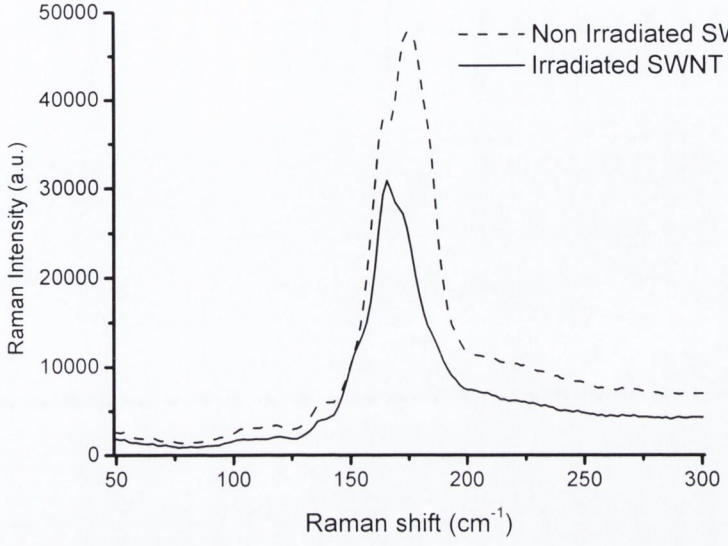

Figure 5.18 Radial breathing mode of irradiated and non irradiated SWNT

The most important observation in figure 5.18 is that the radial breathing mode is strongly present in both the irradiated and non-irradiated SWNT samples. This means that the SWNT are not damaged to any great degree in the laser irradiation process and therefore it can be inferred that the MWNT are also not degraded by the irradiation.

An interesting fact is found on closer inspection of figure 5.18, which involves the effect on the two components of the radial breathing mode peak. Lorenztian decomposition of the radial breathing mode for the irradiated and non irradiated SWNT is shown in figure 5.19. It shows that the 177 cm^{-1} component of the radial breathing mode is greatly reduced on irradiation. Since the radial breathing mode is related to the diameter of the nanotubes a change in its components corresponds to a change in the diameter distribution of the SWNT in the sample.

This indicates that while SWNT of a certain diameter are unaffected by the laser irradiation, others of different diameter may be adversely affected and even vaporised. It is most likely that this would occur in metallic SWNT as the local heating can lead to higher temperatures.

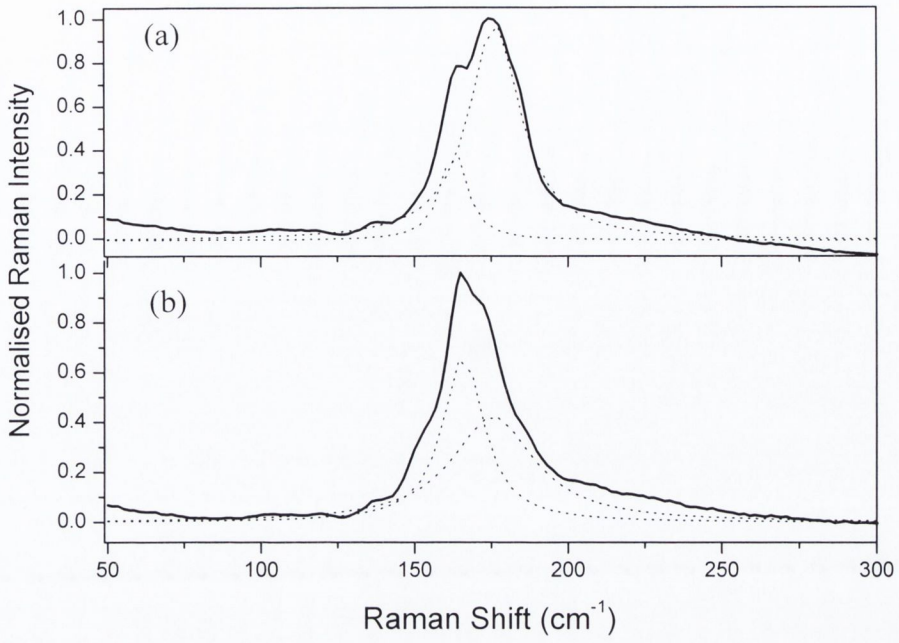

Figure 5.19 Lorentzian fits to RBM of (a) non irradiated & (b) irradiated SWNT

Speculatively such a process could be a means of selecting SWNT with a certain diameter distribution. Such a technique, termed size selection, is much sought after in the field of carbon nanotubes.

The issue of nanotube selection also arises due to the thermal influence of the laser irradiation. The basis for this is the decomposition of the carbon nanotube polymer composite on irradiation. The binding between the polymer and the nanotubes in the composite is known to be weak[6]. It is not surprising then that thermal energy is sufficient to separate the nanotubes from the polymer in solution. On irradiation of a dilute sample, black specks corresponding to groups of nanotubes can be observed emerging from the composite, by close inspection. The effect is particularly dramatic in the case of SWNT which given their tendency to form bundles and ropes, bunch together to form clumps before falling to the bottom of the vessel.

Sample Stability

For the purpose of the experiments carried out here, sample stability under irradiation is of importance. Transmission of the samples was monitored to ensure adequate stability and higher concentration composites served to counteract the thermal decomposition effect. A possible benefit of the thermal decomposition

process is as a method to separate nanotubes from the polymer in the composite. Since the composite is used as a method of purifying nanotubes, and also of size selecting SWNT in the case of low concentration composites[7], thermal separation could be used as a means of removing the nanotubes from the composite leaving SWNT of a particular diameter distribution.

5.3 Multiphoton Absorption Induced Luminescence

The information from the investigations carried out is now compiled in order to establish an understanding of the underlying processes responsible for the nonlinear photoluminescence observed in MWNT. A review of emission processes in related materials is given in order to ascertain if there are similarities with other phenomena. A discussion of the photoluminescence observed in GP is also given.

5.3.1 Review of Luminescence Processes in Carbon Materials

This review of luminescence processes highlights the fact that, although at first sight luminescence in carbon materials seems improbable, there are many factors, which can contribute to the generation of electronic states or the creation an environment where efficient luminescence can be induced in these materials. Additionally it is illustrated that many of these luminescent states can support nonlinear type photoluminescence. On reflection then, the prospect of nonlinear photoluminescence in MWNT does not seem so extraordinary.

Amorphous Carbon

Amorphous carbon refers to disordered arrangements of carbon atoms. These structures include sp^3 hybridised sites distributed among the usual sp^2 graphite hybridisation. The presence of sp^3 sites introduces a bandgap into the material the magnitude of which depends on the sp^3/sp^2 ratio[8,9]. The presence of the bandgap and defect sites provides the opportunity for luminescence in these materials. A schematic diagram of band structure of a typical amorphous carbon material[10] is shown in figure 5.20.

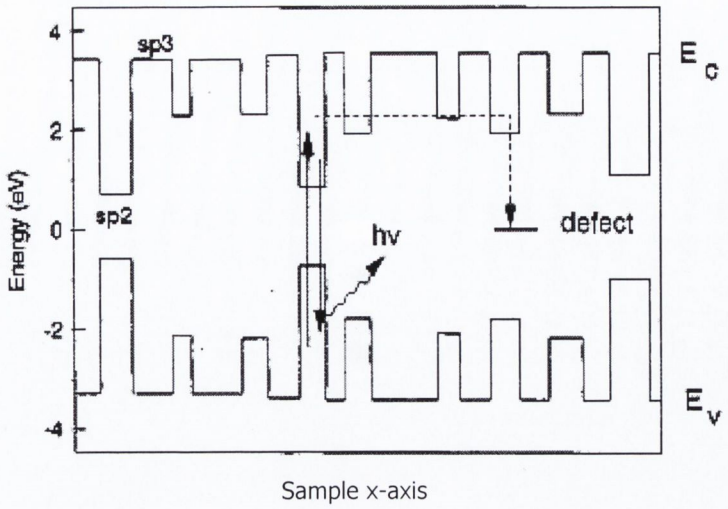

Figure 5.20 Schematic band diagram of an amorphous carbon material Luminescence occurs by photoexcitation and radiative recombination. Non-radiative recombination occurs by tunnelling or hopping to carriers or defects[10].

Large band edge fluctuations are present due to the sp^2 and sp^3 bonding. Photoluminescence can be understood in terms of the creation of an electron hole pair upon photo excitation. The electron and hole consequentially lose energy by thermalisation until they reach the valence and conduction band tail states respectively. Photoluminescence then arises when the electron and hole pair recombine across the bandgap.

Diamond Particles

Diamond specimens are commonly characterised by several types of optical centres that are present due to natural origin or the growing conditions[11,12]. These centres can give rise to luminescence and can be excited by either photons to give photoluminescence or by energetic electrons to give cathodoluminescence[12,13,14]. A luminescent response at photon energies ranging between 1eV and 5.5eV are produced depending on the type of emission centres present. Impurities and radiation induced defects in diamond result in the generation of electronic levels deep in the band gap. Excitation of these states is possible using photon energies smaller than the band gap in a multiphoton absorption process[15].

The photoluminescence properties of nanodiamond particles, have been studied by Glinka et al, using laser excitation at both a low and high power densities[16]. Analysis of the intensity dependences of the induced photoluminescence shows that

excitation in the low power regime corresponds to one-photon excited processes, whereas at high power it corresponds to multiphoton excited photoluminescence.

Fullerene C_{60}

Although the fullerenes were discovered more than sixteen years ago, the electronic spectroscopy of C_{60} molecules still possess a number of unsolved problems. The origin of certain components of even the molecular photoluminescence, as yet remain unclear[17,18].

Solid phase C_{60} gives rise to a photoluminescence spectrum whose features are different compared with molecular photoluminescence spectra, with broader line widths, a reduced number of structures and different intensity distributions[19,20]. These differences suggest that, other luminescent processes can arise in solid state C_{60}. Additionally there are inconsistencies in the luminescence spectra reported for solid phase C_{60}. Luminescence spectra from C_{60} single crystals has been known to depend on samples, crystal sites, cooling rates, heating processes and so on[21,22].

Pristine solid C_{60} is a van der Waals bonded molecular solid. In molecular solids energy transfer through the lattice is more difficult than in the case of ionic or covalent crystals. Hence the elementary excitations remain localised on each photoexcited C_{60} molecule. In self trapped states selection rules are broken and radiation recombination of self trapped exitons can occur.

Capozzi et al carried out a detailed study of optical spectra and photoluminescence of C_{60} thin films. In figure 5.21 the low temperature photoluminescence spectrum of an 80 nm C_{60} thin film, excited using a cw Ar^+ source[21] is shown. Four emission bands can be distinguished. These bands retain their spectral position though they broaden significantly with increasing temperature. There are further reports that fullerene thin films can be made to emit broad intense light under laser irradiation by the introduction of heterogeneous structures.

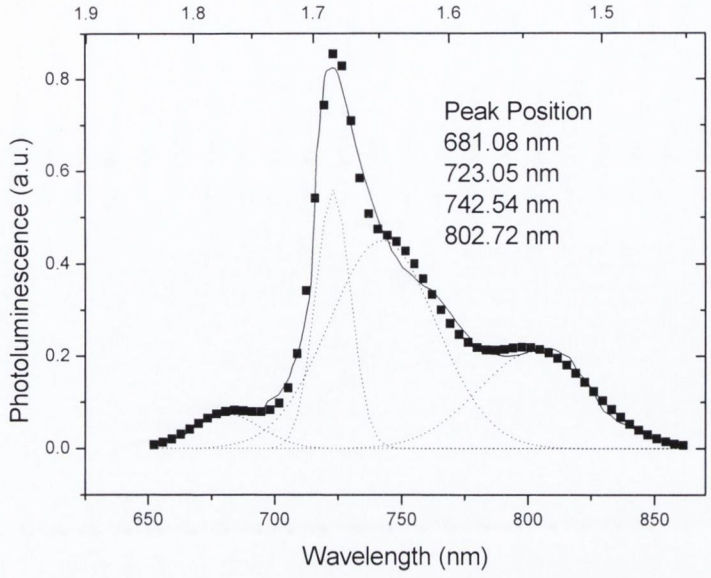

Figure 5.21 Luminescence spectrum at 10K of a C_{60} thin film[21].

Wen et al measured SEM mode cathode electroluminescence for pure C_{60} and C_{60}/Si composite thin films[23] as shown in figure 5.22.

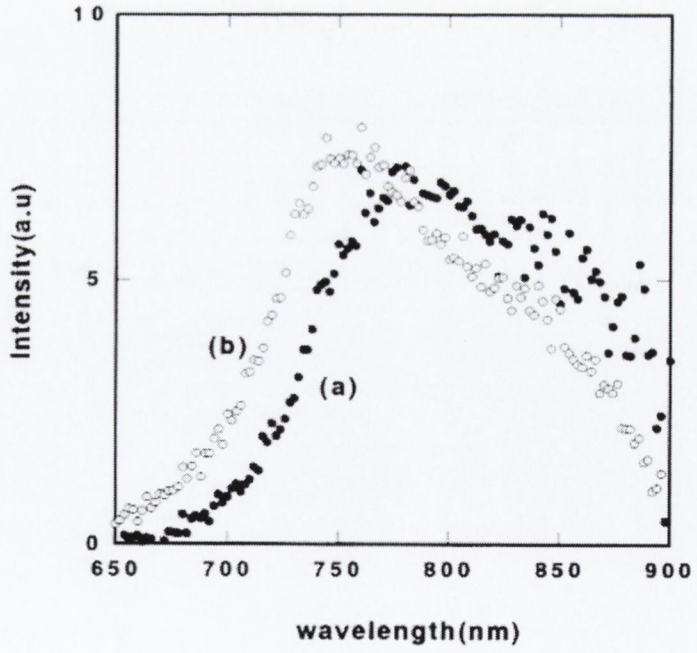

Figure 5.22 Cathodoluminescence of scratched films (a) C_{60}/Si & (b) pure C_{60} [23]

The films were scratched as a means of introducing heterogeneous structures. Microscopic FTIR spectra showed that little transformation occurred on the C_{60} cage as a result of scratching for either pure or composite C_{60} thin film. However, the fact that only the scratched part could show CL, suggesting that structures (undetectable by FTIR) introduced by scratching were involved in the electronic excitation and luminescent processes. Most likely these provide local enhancement of the optical processes by reducing the symmetry.

Thermally induced blackbody emission is also a feature of C_{60} thin film emission. Wen et al report a broad spectrum in the infrared region, produced at crack sites under laser irradiation, which can be fitted to Planck's blackbody formula[24].

There are also several reports of visible photoluminescence in highly excited solid fullerene C_{60} films and crystals. Byrne et al demonstrated the strong nonlinear behaviour of the luminescence[25],[26] while Feldmann et al attributed the photoluminescence to a multi–step absorption induced process[27]. These emissions are similar to the visible emission observed by Wen et al[23] shown in figure 5.22.

The prospect of multiphoton absorption induced photoluminescence in MWNT is further supported by similar photoluminescence mechanisms observed in solid C_{60}. Feldmann et al reported intense and spectrally broad luminescence from polycrystalline C_{60}. The luminescence was attributed, on the basis of time-resolved luminescence studies, to transitions between higher electronic band states, populated by two-step absorption processes. Their observation of white luminescence for excitation in the infrared verifies this interpretation.

5.3.2 Nonlinear Optical Properties

Theoretical calculations on carbon nanotubes predict a large nonlinear optical response, which is greatly enhanced by multiphoton resonant interactions[28],[29]. Xie et al have shown that peaks in the wavelength dependence of the third order nonlinear response for C_{60} derived nanotubes can result from three-photon excitation in the region of 1.2 eV[30].

The DFWM and Z-scan results confirm the presence of a considerable large third order nonlinear optical response in MWNT throughout the spectral range investigated. In particular the DFWM results showed the nonlinear response to have a considerable ultrafast component. The presence of a large electronic nonlinear response at 1064 nm (1.16 eV) substantiates the prospect of strong nonlinear optical activity at this energy. These results concur with an electronic origin to the nonlinear photoluminescence observed in MWNT. The nanosecond decay measurements of the MWNT photoluminescence further further support this conjecture.

Graphitic particles are known to exhibit a large thermal response to high intensity radiation[31]. This view is supported by DFWM measurements in which no signal was found for GP samples.

5.3.3 Mechanism of Multiwalled Nanotube Induced Luminescence

The remarkable spectral coincidence of the photoluminescence and a set of VHS in the visible region is now examined. The overlap of the two spectra is depicted in figure 5.23.

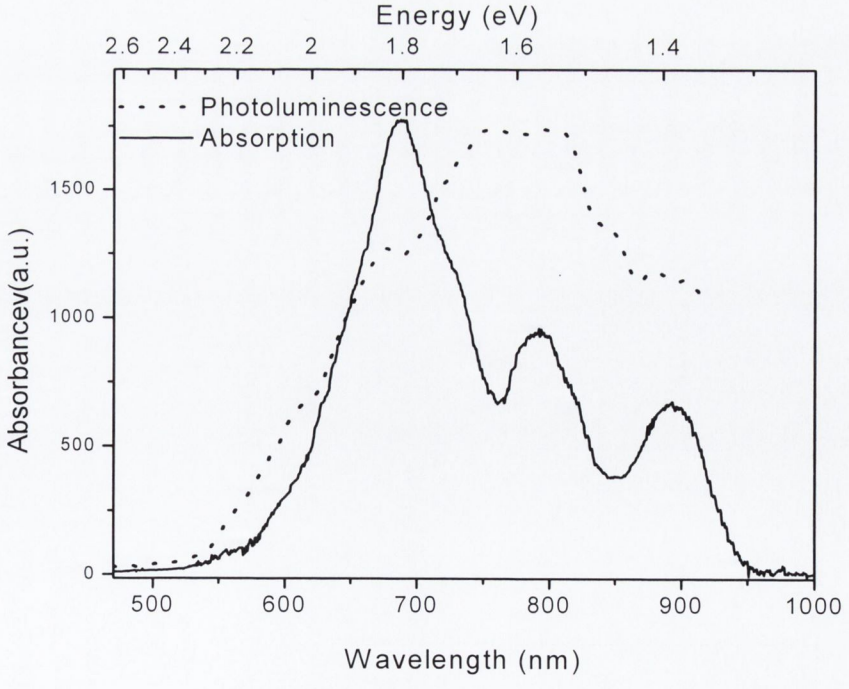

Figure 5.23 MWNT van Hove singularity absorption & photoluminescence spectra

There are many important features shared by the two spectra. The spectra both rise and fall in the same spectral range, and have almost the same spectral width, though the photoluminescence is slightly broadened. These factors indicated that the VHS absorption and the photoluminescence are intricately linked. A mechanism describing this underyling link is presented in diagrammatic form in figure. 5.24.

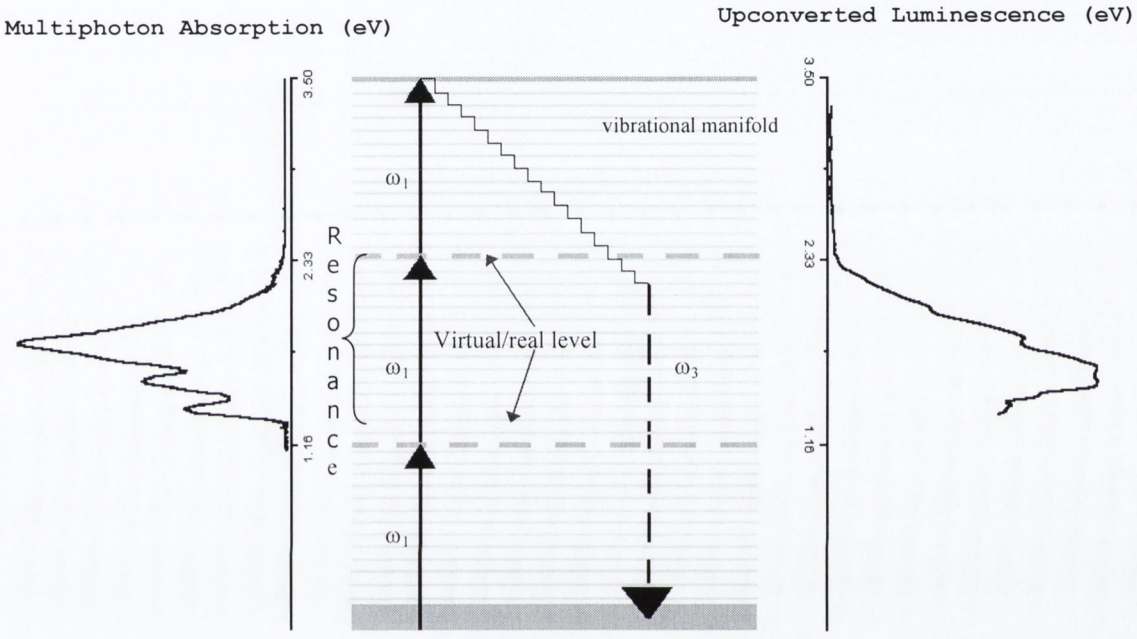

Figure 5.24 Schematic of MWNT multiphoton excited photoluminescence

According to the power law studies, a three photon process is involved. Multiphoton absorption consisting of three photons provides excitations, via real or virtual levels located at 1.16 eV and 2.33 eV to an energy level at 3.54 eV. The 2.3 eV energy level and possibly the 1.16eV level fall within the tail of the real energy levels of the identified VHS. Therefore, these interactions involve a partially resonant interaction and enhancing the multiphoton absorption process.

Once excitation has taken place the following scenario seems likely: initial nonradiative decay occurs through the extensive vibrational manifold of MWNT. Radiative decay is not possible at this point due to the insufficiently large transition probability of the environment. However, when the first VHS is reached the optical transition probability becomes large enough to initiate radiative emission. The first

VHS is located in the 688 nm region. This is a broad peak which begins rising above 500 nm, which corresponds precisely to the onset of the MWNT photoluminescence.

Further luminescence is prompted by the following van Hove singularities. As many of the singularities are broad and exhibit shoulders and features the induced photoluminescence can also be expected to be broad and contain features, as is the case in the MWNT photoluminescence spectrum. Again, it is significant that the photoluminescence appears to diminish just at the spectral region where no further van Hove singularities are present.

5.3.4 Quantum Theoretical Interpretation

A derivation of the physical origin of the photoluminescence using a quantum theoretical interpretation as given in Loudon[32] is now outlined. Consider the interaction between an atom and an electric field, which in quantum mechanics is described by a Hamiltonian. An electromagnetic wave is given in the form

$$E = E_0 \cos(kz - \omega t) \tag{5.2}$$

The total electric dipole moment of the atom is written –eD, where e is the electronic charge and $D = \sum_{\alpha=1}^{Z} r_\alpha$ with Z being the atomic number of the atom and r is the electronic distance from the nucleus. The main contribution to the interaction Hamiltonian ($\hat{H}_{ED}$) arises from the potential energy of this electric dipole in the electric field of the light beam as given by

$$\hat{H}_{ED} = eD.E_0 \cos(\omega t) \tag{5.3}$$

Setting the direction in which E_0 points as x, the x component of the dipole moment denoted X is where $X_{12} = \int \psi_1^* X \psi_2^* dV$. Setting $\hbar\zeta = eE_0 X_{12}$, the numerical factor in the electric – dipole matrix element.

Recalling standard relations of quantum mechanics;

$\Psi(r,t) = C(t)_1 \Psi_1(r,t) + C(t)_2 \Psi_2(r,t)$ Wave function is a linear superposition

$\hat{H}\Psi(r,t) = i\hbar\partial\Psi(r,t)/\partial t$ Time dependent Schrödinger equation

$\Psi_i(r,t) = \Psi_i(r)\exp(-iE_i t/\hbar)$ Solution to Schrödinger's equation

Applying these rules to equation (5.2) and (5.3) the following relations result

$$\zeta\cos(\omega t)\exp(-i\omega_0 t)C_2 = idC_1/dt$$
$$\zeta\cos(\omega t)\exp(i\omega_0 t)C_1 = idC_{21}/dt \qquad (5.4)$$

Expressions for Einstein coefficients are now introduced. Einstein B coefficient, which describe absorption and stimulated emission processes require solutions of equation (5.4). Assuming that the atom is in its lower state ψ1 at a time t=0 and $|C_2|^2$ is the probability that the atom is excited after a time t. It follows then that

$$B_{12}\langle W(\omega_0)\rangle = |C_2|^2/t \qquad (5.5)$$

where $\langle W(\omega_0)\rangle$ is the mean energy density in the light beam per unit frequency range at ω_0. Approximate solutions for C_1 and C_2 can be found using an iterative method. Setting the initial values as $C_1(0)=1$ and $C_2(0)=0$, substituting these into equation (5.4) and integrating with respect to time gives a first approximation to the time dependence of the coefficients as

$$C_1(t)=1 \qquad (5.6)$$

and

$$C_2(t) = \frac{\zeta}{2}\left\{\frac{1-\exp[i(\omega_0+\omega)t}{\omega_0+\omega} + \frac{1-\exp[i(\omega_0-\omega)t}{\omega_0-\omega}\right\} \qquad (5.7)$$

(second approximation is obtained by substituting these solutions into equation (5.4) and integrating again. The improved solutions have the forms

$$C_1(t)=1+\zeta^2\times(\text{function of t}) \qquad (5.8)$$

And $C_2(t)$ is unchanged form equation (5.7). Further approximations can be obtained enventually resulting in an even power series of ζ for $C_1(t)$, and odd power series for $C_2(t)$.

For light whose frequency ω is exactly equal to ω_0 equation (5.7) reduces to

$$C_2(t) = -(i\zeta / 2\omega_0)\{\sin(\omega_0 t)\exp(i\omega_0 t) + \omega_0 t\} \tag{5.9}$$

Since atomic transitions take place over time spans of 10^{-7} s or longer, where as the transition frequency is typically of the order of 10^{-15} s, it follows that the inequality $\omega_0 t >> 1$ holds. The many cycles of the electromagnetic wave that occur before any significant oscillation, means, that the second bracketed term in equation (5.9) is therefore much larger than the first. A similar case arises in equation (5.7) when ω is close but not exactly equal to ω_0. Neglecting this first term in equation (5.7) in what is known as the 'rotating wave approximation' gives

$$|C_2(t)|^2 = \zeta^2 \frac{\sin^2\{\frac{1}{2}(\omega_0 - \omega)t\}}{(\omega_0 - \omega)^2} \tag{5.10}$$

equation (5.10) gives a solution for the probability of excitation of the atom into its upper level.

The Dirac delta function is defined by

$$\delta(\omega_0 - \omega) = \frac{2}{\pi}\sum_{t\to\infty} \frac{\sin^2\{\frac{1}{2}(\omega_0 - \omega)t\}}{(\omega_0 - \omega)^2} \tag{5.11}$$

It is now possible to write equation (5.10) in the form of an expression for the transition rate $1/\tau$, using the Dirac-delta function as follows

$$1/\tau = |C_2(t)|^2 / 2 - \tfrac{1}{2}\pi\zeta^2\delta(\omega_0 - \omega) \tag{5.12}$$

This transition rate formula can be applied to the interaction Hamiltonian given in equation (5.3) as,

$$\left\langle 1\left|\hat{H}_{ED}\right|2\right\rangle = \tfrac{1}{2}eE_0X_{12}\exp(-i\omega t) = \tfrac{1}{2}\hbar\zeta\exp(-i\omega t) \tag{5.13}$$

The replacement for ζ in equation (5.12) gives

$$1/\tau = \tfrac{2\pi}{\hbar^2}\sum_f \left|\left\langle f\left|\hat{H}_{ED}\right|i\right\rangle\right|^2 \delta(\omega_f - \omega_i) \tag{5.14}$$

where the formula is generalised to apply to the transition between an initial state $|i\rangle$ and a range of final states $|f\rangle$, with energies $\hbar\omega_i$ and $\hbar\omega_f$ respectively. The transition rate formula given in equation (5.14) is known as 'Fermi's Golden Rule. Use of the delta function can become more physically meaningful on integration and the summation over f is best interpreted as an integral over a continuous range of final states $|f\rangle$. For the treatment of higher order interactions, such as the case of three photon interactions which are relevant to the events observed here, equation (5.14) can be expanded as give in equation (5.15).

$$\tau^{-1} = \frac{2\pi}{\hbar^2}\int d\omega_f \left| \langle f|\hat{H}|i\rangle + \frac{1}{\hbar}\sum_{\nu_0} \frac{\langle f|\hat{H}|\nu_0\rangle\langle \nu_0|\hat{H}|i\rangle}{\omega_i - \omega_{\nu_0}} \right. \qquad (5.15)$$
$$\left. + \frac{1}{\hbar^2}\sum_{\nu_1}\sum_{\nu_2} \frac{\langle f|\hat{H}|\nu_1\rangle\langle \nu_1|\hat{H}|\nu_2\rangle\langle \nu_2|\hat{H}|i\rangle}{(\omega_i - \omega_{\nu_1})(\omega_i - \omega_{\nu_2})} \right|^2 \rho_f \rho_i \delta(\omega_i - \omega_i)$$

where, ρ is the electron densities of states and $|\nu_0\rangle$, $|\nu_1\rangle$ and $|\nu_2\rangle$ correspond to the one, two and three photon states.

This equation allows us to qualitatively describe the multiphoton excited luminescence observed in MWNT in terms of quantum mechanical transitions which are involved. It shows that the rate of transitions is directly proportional to the density of states. Given that VHS have a very high associated density of states, hence according to Fermi's Golden Rule, any optical transitions which are resonant with these VHS are expected to be greatly enhanced. The linear absorption spectrum in figure 5.12 is representative of the distribution of the VHS density of states and account for the observation of optical transitions, specifically radiative decay, in this spectral region. Fermi's Golden Rule also provides a means of relating the transition states, visualised in section 5.33, to their quantum theoretical origin and is useful in validating the principles used in this model. Hence the basic quantum theoretical interpretations are in agreement with the qualitative model described in section 5.33.

5.3.5 Graphitic Particle Luminescence

TEM images show that the GP consist of micron and nanometer randomly structured particles indicating the presence of dangling bonds and defects. Further evidence for this is given by the presence of carbon hydrogen and carbon oxygen bonds in the GP FTIR spectra. Studies have shown that under such conditions a band gap is induced in the region of 1.5 eV to about 3 eV, depending on composition, size and shape of the carbon clusters.

Luminescence and thermalisation processes can readily occur in these materials. The spectral range of the luminescence depends on the width of the band gap. Here the luminescence occurs in the 1.9 eV region which corresponds to a relative low sp^3/sp^2 ratio.

The presence of a band gap and luminescence pathways also provides the potential for a multiphoton excitation mechanism. The power law investigations indicate that a two photon process is involved which only becomes apparent at the higher intensity range. This is due to the dominant thermalisation processes which occur, resulting in large contributions from blackbody radiation. However, given the nature of nonlinear processes, above a certain threshold intensity, they over ride the linear processes and the true luminescent nature of GP becomes apparent.

It is evident therefore that two different luminescent processes operate, the first being mainly thermal in nature. The second originates from radiative recombination across the bandgap. It is significant that a two photon absorption process is involved in the excitation process which contrasts with the three photon excitation involved in the MWNT photoluminescence. This underlines the fact that different mechanisms are responsible for the luminescence in the two materials.

5.4 Conclusions

Near infrared laser irradiation of carbon nanotubes produced a number of effects. The most exceptional was the production of visible/NIR luminescence from MWNT. Investigations reveal a multiphoton excitation process and indicate that the luminescence originates from optical transitions in the MWNT van Hove

singularities. MWNT were also shown to exhibit Planck blackbody radiation in the near infrared. This arises due to sample heating from absorption and non radiative decay. Significantly, the MWNT blackbody temperatures are less than in the case of graphitic particles under the same irradiation conditions.

Visible luminescence was also observed in graphitic particles on near infra excitation. However the difference in the spectral features and the power law dependence of the graphitic luminescence demonstrate that the emission process differs form that observed in MWNT. Defect sites in the graphitic particle structure are suggest as the source of the luminescence.

Examination of the effect of the laser irradiation on samples confirmed that the observed luminescence and blackbody radiation did not arise from a burning, ionisation or vaporisation processes. The induced thermal action within the samples was shown to have possible benefits, such as a method of separating nanotubes from the polymer in the composite aid a size selection process for SWNT.

References

1 Vitor Baranauskas, Marcelo C. Tosin, Alfredo C. Peterlevitz, Helder J. Ceragioli, and Steven F. Durrant, Thin Solid Films **315**, (2000).

2 Jun Xu, Tianfu Ma, Wei Li, Kunji Chen, Jiafang Du, and Xinfan Huang, Journal of Non-Crystalline Solids **769**, (2000).

3 R. Q. Zhang, E. Bertran, and S. T. Lee, Diamond and Related Materials **7** *11-12*, 1663 (1998).

4 H. Y. Yu, S. H. Jhang, Y. W. Park, A. Bittar, H. J. Trodahl, and A. B. Kaiser, Synthetic Metals **121** *1-3*, 1223 (2001).

5 R. Philip, P. Sathy, V. P. N. Nampoori, J. Philip, and C. P. G. Vallabhan, Journal of Physics B-Atomic Molecular and Optical Physics **25** *1*, 155 (1992).

6 B. McCarthy, J. N. Coleman, S. A. Curran, A. B. Dalton, A. P. Davey, Z. Konya, A. Fonseca, J. B. Nagy, and W. J. Blau, Journal of Materials Science Letters **19** *24*, 2239 (2000).

7 A. B. Dalton, W. J. Blau, G. Chambers, J. N. Coleman, K. Henderson, S. Lefrant, B. McCarthy, C. Stephan, and H. J. Byrne, Synthetic Metals **121** *1-3*, 1217 (2001).

8 J. Q. Chen, J. A. Freitas, and D. L. Meeker, Diamond and Related Materials **9** *1*, 48 (2000).

9 J. Robertson, Diamond and Related Materials **4** *4*, 297 (1995).

10 J. Robertson, Diamond and Related Materials **5** *3-5*, 457 (1996).

11 A. T. Collins, T. Sharda, A. K. Sikder, D. S. Misra, S. Bhargava, H. D. Bist, P. Veluchamy, H. Minoura, D. Kabiraj, D. K. Awasthi, and P. Selvam, Diamond and Related Materials **7** *2-5*, 250 (1998).

12 E. A. Ekimov, S. A. Klimin, H. F. Borovikov, G. V. Saparin, S. K. Obyden, and G. B. Rulev, Scanning **19** *7*, 469 (1997).

13 K. Iakoubovskii and G. J. Adriaenssens, Diamond and Related Materials **9** *7*, 1349 (2000).

14 P. Joeris, I. Schmidt, and C. Benndorf, Diamond and Related Materials **5** *6-8*, 603 (1996).

15 Y. D. Glinka, K. W. Lin, H. C. Chang, S. H. Lin, and Y. T. Chen, in *Defects and Diffusion in Ceramics* (Scitec Publications Ltd, Uetikon-Zuerich, 2000), Vol. 186-1, pp. 37.

[16] Y. D. Glinka, K. W. Lin, H. C. Chang, and S. H. Lin, Journal of Physical Chemistry B **103** *21*, 4251 (1999).

[17] J. H. Rice, R. Aures, J. P. Galaup, and S. Leach, Chemical Physics **263** *2-3*, 401 (2001).

[18] S. M. Argentine, K. T. Kotz, T. Rudalevige, D. Zaziski, A. H. Francis, R. Zand, and J. A. Schleuter, Research on Chemical Intermediates **23** *7*, 601 (1997).

[19] H. J. Byrne, W. K. Maser, W. W. Ruhle, A. Mittelbach, W. Honle, H. G. Vonschnering, S. Roth, and B. Movaghar, Synthetic Metals **54** *1-3*, 265 (1993).

[20] V. V. Kveder, V. D. Negrii, E. A. Shteinman, A. N. Izotov, Y. A. Osip'yan, and R. K. Nikolaev, Journal of Experimental and Theoretical Physics **86** *2*, 405 (1998).

[21] V. Capozzi, G. F. Lorusso, T. Trovato, B. Viguier, and A. Minafra, Journal of Luminescence **72-4**, 473 (1997).

[22] V. Capozzi, M. Santoro, G. Celentano, H. Berger, and G. F. Lorusso, Journal of Luminescence **76-7**, 395 (1998).

[23] C. Wen, T. Tada, and N. Minami, Carbon **38** *10*, 1503 (2000).

[24] C. Wen, Y. Tong, N. Minami, and T. Tada, Synthetic Metals **103** *1-3*, 2372 (1999).

[25] H. J. Byrne, W. K. Maser, W. W. Ruhle, A. Mittelbach, and S. Roth, Applied Physics a-Materials Science & Processing **56** *3*, 235 (1993).

[26] H. J. Byrne, A. T. Werner, J. Anders, W. K. Maser, M. Kaiser, L. Akselrod, W. W. Ruhle, A. Mittelbach, and S. Roth, Journal of Modern Optics **41** *6*, 1243 (1994).

[27] J. Feldmann, R. Fischer, W. Guss, E. O. Gobel, S. Schmittrink, and W. Kratschmer, Europhysics Letters **20** *6*, 553 (1992).

[28] V. A. Margulis, E. A. Gaiduk, and E. N. Zhidkin, Diamond and Related Materials **8** *7*, 1240 (1999).

[29] Vl.A. Margulis and T.A. Sizikova, Physica B: Condensed Matter **245** *2*, 173 (1998).

[30] R. H. Xie, Nuovo Cimento Della Societa Italiana Di Fisica D-Condensed Matter Atomic Molecular and Chemical Physics Fluids Plasmas Biophysics **19** *12*, 1867 (1997).

[31] K. Mansour, M. J. Soileau, and E. W. Vanstryland, Journal of the Optical Society of America B-Optical Physics **9** *7*, 1100 (1992).

[32] R Loudon, *The quantum theory of light*. Oxford University Press, Oxford, 2000.

Chapter 6
Optical Limiting

Optical limiting is one of the most useful applications of nonlinear optical effects. It can be used in devices for the protection of light sensitive elements, such as the human eye, against intense radiation sources. Optical Limiters can offer protection by employing nonlinear optical effects; such as reverse saturable absorption (RSA) or nonlinear scattering, to attenuate the incident radiation once it exceeds the threshold intensity.

Here the potential of the series of organic materials as optical limiters is examined. These materials encompass a range of specially designed features, intended to benefit their performance. The endohedral lanthanum fullerene has been shown in chapter 4, exhibit a nonlinear absorption response, which is both broadband and ultrafast. Carbon nanotubes were also shown to possess a broadband nonlinear optical response. Phthalocyanines are well established as optical limiting materials and the set of axially substituted phthalocyanines present the additional possibility of controlling the nonlinear absorption via chemical modulation. The materials chosen for study here therefore address many of the current issues concerning optical limiting materials while also exploring the potential to control optical limiting devices.

6.1 Background to Optical Limiting

Photonic sensors including the human eye can be irreversibly damaged by intense sources of radiation. The safety threshold of a sensor depends on the nature of the material and can differ over orders of magnitude. The value of 10^2 Wcm^{-2} is generally taken as standard for the human eye minimum damage threshold. The ideal action of a protection device for these sensors is depicted in figure 6.1.

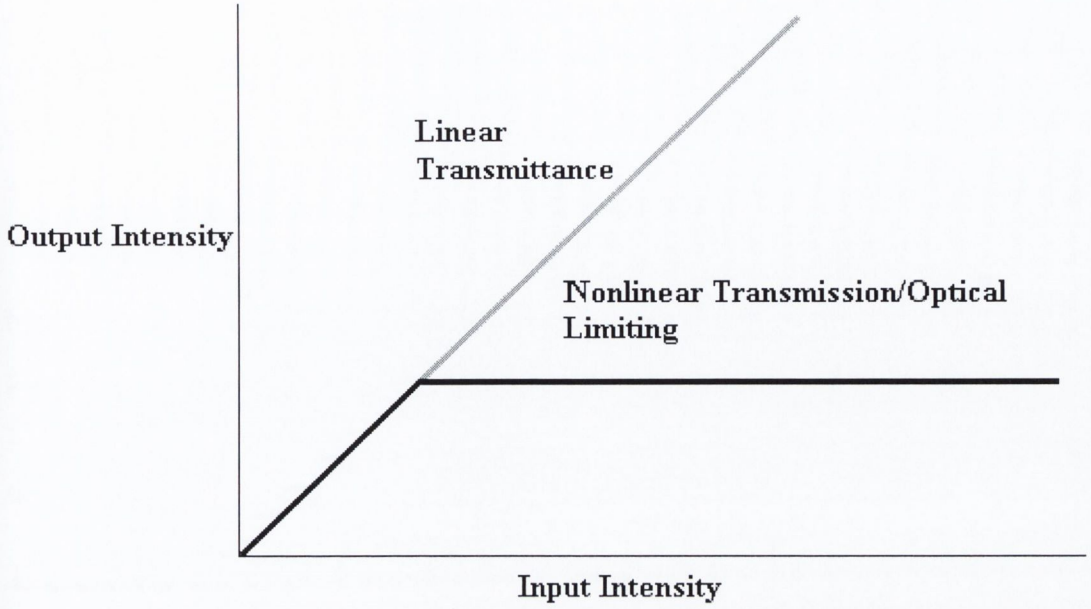

Figure 6.1 Transmission of linear materials & those exhibiting optical limiting

The diagram in figure 6.1 illustrates the transmittance behaviour of a normal linear material and that of an optical limiting material. A certain amount of linear transmission is required at lower intensity range in order for the photonic sensor to carry out its function as a detector. At higher incident intensities, approaching the sensor damage threshold, the transmission saturates and is maintained below the threshold level. This however is the ideal case and in most optical limiting materials the slope of the linear transmission is simply reduced. The effectiveness with which a material can carry out this task is a critical factor of its optical limiting performance.

6.1.1 Optical Limiting Mechanisms

Several nonlinear optical processes can give rise to an optical limiting type transmission response including; reverse saturable absorption, multiphoton absorption, nonlinear refraction, nonlinear scattering, and thermal blooming. Reverse saturable absorption was first observed by Giuliano and Hess when studying various organic dye molecules[1]. They noticed that under intense laser pulses, these organic dyes did not show bleaching (saturable absorption) as expected, but instead showed increased absorption at high intensities. This reverse

saturable absorption mechanism, has since been shown to provide high speed optical limiting. In the case of multiphoton absorption such as two-photon absorption, an electron is promoted from the ground state to the excited state by either the simultaneous or stepwise absorption of two photons. This mechanism is efficient for the limiting of short pulses.

Nonlinear refraction can be a consequence of various phenomena that may take place in materials, but the result is similar: self focusing or defocusing of light away from the sensor. Compared with optical limiting devices that function by absorbing the radiation, these types of limiter can have a much larger dynamic range.

Thermal nonlinearities arise from the absorption of radiation which gives rise to heating of the materials. The heating results in the expansion of the volume which in turn modifies the index of refraction of the material. In the case of nonlinear scattering, the thermally induced local changes result in the formation of small scattering centres. Increased scattering at higher intensity directly limits the transmitted intensity.

In general, materials that exhibit optical limiting behaviour use these mechanisms in any combination, although sometimes one or more processes are predominant in the material used. In the materials studied here reverse saturable absorption accompanied by nonlinear scattering are the dominant processes and these processes are now discussed in more detail.

Reverse Saturable Absorption

Reverse saturable absorption (RSA), which translates into increased optical absorption with increased incident optical intensity is a favoured mechanism for optical limiting. Materials showing RSA obey the Lambert-Beer law of transmission only at low intensities and deviate significantly from it at high intensities. The primary condition required is that the absorption cross-section of the excited states, $\sigma_{ex,}$ must be larger than that of the ground state, σ_0. The energy level scheme shown in figure 6.2 can be used to describe RSA processes.

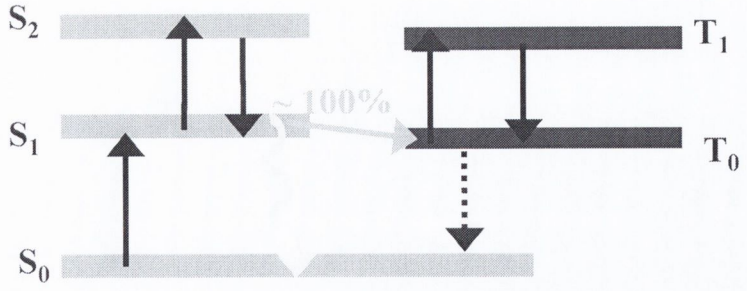

Figure 6.2 Schematic Energy level diagram

Initial absorption occurs from the singlet ground state S_0 to the first excited singlet state S_1. In materials where the absorption cross section of S_1 is higher than that of S_0 a significant fraction of the molecules electron population can be accumulated in the S_1 state whose lifetime is of the order of nanoseconds. The resultant transmission, which involves absorption from the ground state as well as from the excited state, therefore becomes smaller than the low intensity transmission. In materials in which the intersystem crossing time is shorter or comparable to the pulse duration, the excited population can subsequently relax to the nearby triplet state, T_1. In this case, a larger absorption from the triplet state than that from the ground state enables RSA, provided that the lifetime of the triplet state is longer than the pulse duration.

Intersystem crossing then occurs, transferring the population to the lowest triplet level T_0. Emission from the triplet level is slow and therefore the electronic population becomes stored there. Transitions between the higher excited singlet states play no great role in the reverse saturable absorption process, while those in the triplet states help to contain the population in the triplet levels.

Nonlinear Scattering

Nonlinear scattering is another process that can be utilised for optical limiting. There are two kinds of scattering: coherent and incoherent. Coherent nonlinear scattering includes stimulated Raman scattering and stimulated Brillouin scattering. Incoherent nonlinear scattering may occur due to several processes, which lead to a change in the local density and hence to refractive index of the medium. In an absorbing medium, the origin of the scattering can be manifold, however absorption

induced heating and thermal interactions are the primary mechanism of relevance here. Local material sites commonly experience volume expansion due to the heating. In solution, heating can result in bubble formation and vaporisation. These effects amount to the creation of scattering centres which can effectively scatter the incident light and provide strong optical limiting.

6.1.2 Criteria for Optical Limiting

Organic materials are of considerable interest for developing optical limiting devices. Many inherently incorporate important attributes and readily exhibit a natural tendency to act as optical limiters. The possibility to control and modulate the optical limiting performance of a material is another bonus afforded by the architectural flexibility of many organic materials. An outline is now given of the factors, which are important for optical limiting and the conditions required for materials to perform efficiently.

The criteria desired for optical limiting devices include; broadband operation, an ultrafast time response and an ability to perform at a range of pulse widths. These aspects are considered in terms of an optical limiter, which use RSA as its limiting mechanism. The bandwidth of the optical limiting operation in a material depends on the wavelength dependence of both σ_0 and σ_{ex}. A frequently used figure of merit is κ, which is the ratio of these two parameters

$$\kappa = \sigma_{ex} / \sigma_0 \tag{6.1}$$

In the case of ground state absorption, low residual type absorption is optimal. Such weak absorption enables sufficient optical interaction for the RSA processes to proceed without the adverse effects of saturable absorption. Materials with extended absorption tails provide suitable linear absorption requirements. In the case of excited states those, which can absorb incident photons with the same frequency as the ground state are required. But more importantly, the excited state must have a larger σ_{ex} than σ_0. An effective way of ensuring a larger σ_{ex} is to transfer the excited population to the triplet levels. An efficient and fast intersystem-crossing rate is therefore desired, allowing a fast response to the incident radiation. In materials where intersystem crossing occurs naturally, the

efficiency can be improved by the addition of a heavy metal atom to the molecular structure. In an effect known as the heavy atom effect the metal atom introduces further spin orbit coupling with the triplet level and so enhances the electron transfer process.

6.1.3 Review of Optical Limiting Materials

A review of several organic materials for optical limiting, with attention focused on those relevant to the materials for investigation here, is now given beginning with the fullerenes.

C_{60} is the benchmark material for optical limiting[2,3]. This arises from its remarkable intersystem crossing efficiency, which is almost 100 %[4]. For excitation pulses having durations of a few nanoseconds, the dominant contribution to RSA comes from absorption from the triplet state T_1 with $\sigma_{T_1} / \sigma_{S_0}$ being ~ 3 at 532 nm[5]. Ratios of $\sigma_{T_1} / \sigma_{S_0}$ only slightly greater than 1 are found beyond 650 nm. Thermalisation processes are known to provide additional contributions to optical limiting in C_{60}. All nonradiative relaxation processes result in heating of the solvent resulting in thermal lensing. However the time required for the development of a thermal lens is in the region of 10's of nanoseconds and therefore thermal refraction contributes to the optical limiting of ns pulses but not of ps pulses. Nonlinear scattering can also provide a contribution to the optical limiting action of C_{60}, however the exact source of the scattering is difficult to establish.

The limitations of C_{60} beyond 650 nm are evident from the linear absorption spectrum, where the ground state absorption cross-section becomes too small for effective optical limiting[6]. Materials possessing linear absorption at higher wavelengths are therefore necessary. Higher cage fullerenes are an obvious choice for greater linear absorption bandwidth. Figure 6.3 shows how linear absorption broadens towards longer wavelengths in the higher cage fullerenes. Optical limiting in the higher fullerenes has also been tested, however all of these have shown optical limiting weaker than C_{60} at 532 nm[7]. A higher degree of RSA occurs in C_{60} than in the larger fullerenes possibly due to their reduced intersystem crossing efficiency.

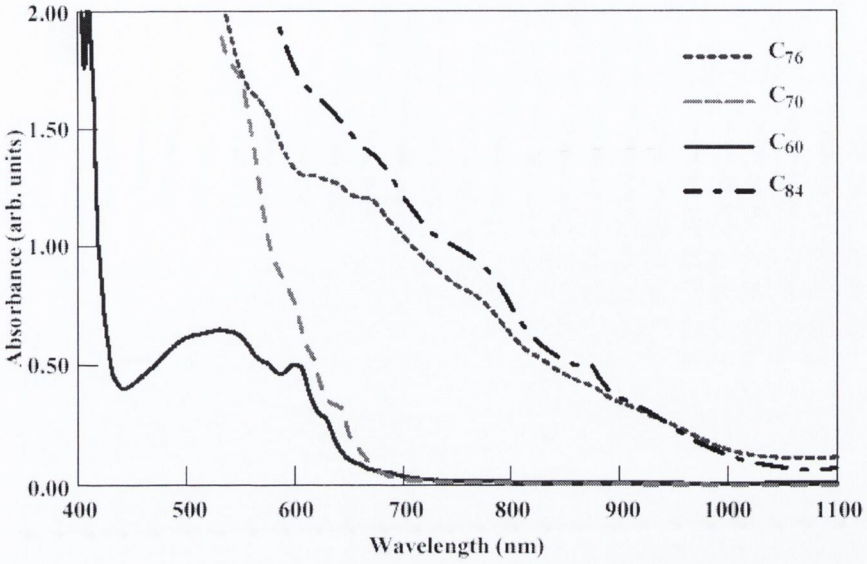

Figure 6.3 Absorption spectra of higher case fullerenes

In an effort to counteract this tendency the higher fullerene C_{82}, incorporating a metal atom, La, central to its cage is tested. The presence of a heavy metal atom in the vicinity of a molecule is known to increase the intersystem crossing efficiency in what is known as the 'heavy atom effect'.

Optical liming in carbon nanotubes has also being investigated[8,9]. MWNT suspensions have been shown to provide optical limiting stronger than C_{60} and carbon black suspensions[10]. The optical limiting action in carbon nanotubes is mainly attributed to nonlinear scattering arising from expanding microplasmas[11]. The microplasmas are assumed to be generated by absorption-induced vaporisation and ionisation, which is also the mechanism proposed for optical limiting in carbon blacks[12].

Porphyrins and phthalocyanines are one of the most studied classes of organic compounds[13,14]. These compounds are based on two dimensional macrocycles which can facilitate extensive chemical modulation. Very large transmission reductions have been reported in certain porphyrin and phthalocyanine compounds with κ values higher than 30 reported[15]. Limiting in these cases has been attributed to RSA and absorption induced thermal lensing. Metal substitution is noted as a means of enhancing the hyperpolarisability and the optical limiting performance of

these compounds[16]. Tests on a series of metallophthalocyanines have shown enhanced optical limiting performance going from lighter to heavier metal substitution[15]. This is interpreted to be a consequence of the increase in the intersystem crossing rate.

6.1.4 Z-scan Technique for Optical Limiting Measurements

In order to examine optical limiting properties of a material a method of determining the transmittance behaviour of the material at both low intensities (intensities at which only linear transmission occurs) and high intensities (intensities at which nonlinear transmission maybe induced) is required. Z-scan, given the large intensity range it encompasses, provides an ideal method to perform such measurements.

For the purposes of optical limiting only the open aperture of a typical Z-scan setup is necessary. This monitors the transmission of the sample over the range of intensities experienced as it traverses a focused beam. A typical Open Z-scan for an optical limiting material is shown in figure 6.4.

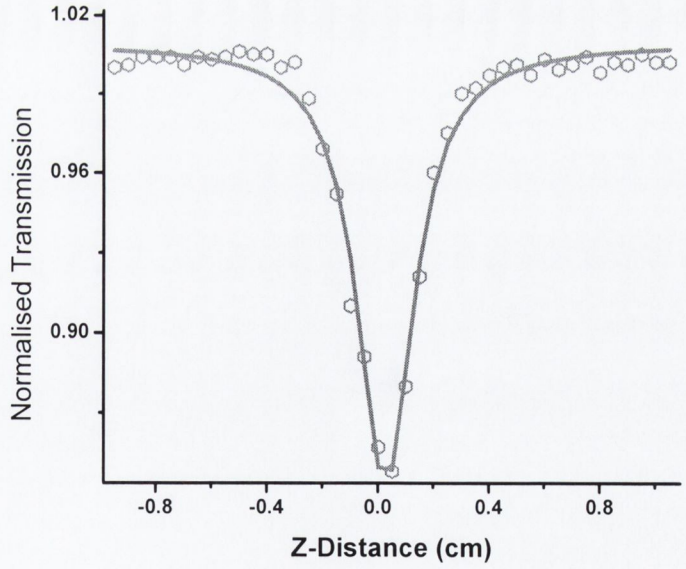

Figure 6.4 Open z-scan for a reverse saturable absorbing material

However, in the case of optical limiting it is usual to present the results as a function of incident intensity rather than position along the z-axis. In this format the

transmission (t) can be fitted with equation (6.2), which enable the σ_0 and σ_{ex} parameters to be calculated and κ to be evaluated.

$$t = 1 - \alpha = 1 - \frac{\sigma_0}{\left(1 + \frac{I}{I_{Sat}}\right)} + \frac{\sigma_{ex}\left(\frac{I}{I_{Sat}}\right)}{\left(1 + \frac{I}{I_{Sat}}\right)} \qquad (6.2)$$

This equation shows the absorption coefficient α expressed in terms of the ground and excited state components, where I is the incident beam intensity and I_{Sat} is the saturation intensity. The expression derives from the linear combination of the ground and excited state absorption coefficients as given in equation (6.3).

$$\alpha = \frac{\alpha_0 I_{Sat} + \alpha_{ex} I}{I + I_{Sat}} \qquad (6.3)$$

where, $I_{Sat} = \frac{h\nu}{\sigma_0 \tau}$ with ν being the excitation frequency and τ being the excited state lifetime.

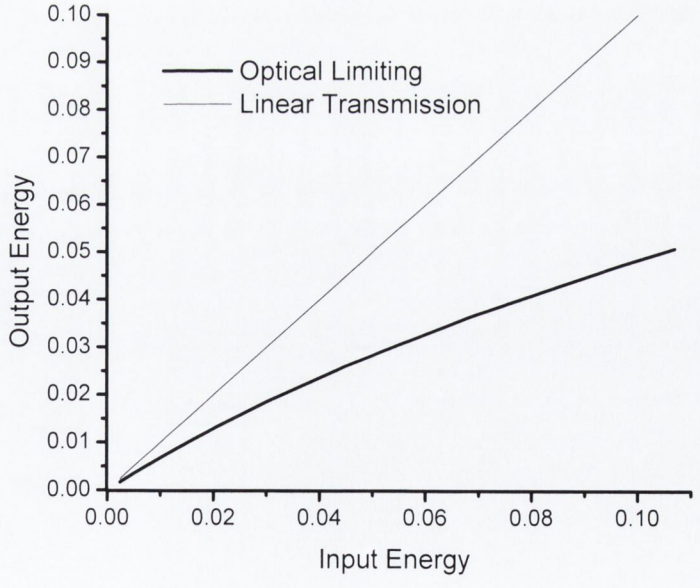

Figure 6.5 Open z-scan for a reverse saturable absorbing material

Results are presented here in the form of input fluence verses output fluence, which is found by multiplying the transmission by the incident energy. A typical result is

shown in figure 6.5 where the linear transmission has been given for comparison. The profile of these plots, though not completely resembling the ideal case as depicted in figure 6.1, they nevertheless approach the desired trend.

6.2 Optical Limiting in Designer Organic molecules

Materials such as the phthalocyanines can be chemically tailored to influence properties such as the location of the main absorption bands and hence influence the band width of the optical limiting response. The predictions and expectations for the axially substituted phthalocyanines, La@C_{82} and the carbon nanotubes are now tested.

6.2.1 Axially Substituted Phthalocyanines

Phthalocyanines are well known as efficient optical limiting materials[17]. On irradiation these molecules quickly reach the first excited singlet state, which subsequently converts to the first triplet state by efficient intersystem crossing. The triplet state has the required long lifetime and large absorption coefficient necessary for efficient optical limiting.

Improvement of reverse saturable absorption efficiency in phthalocyanines has been achieved through peripheral and metallic substitutions[18]. Extensive studies has have been carried out on various types of in-plane substituted phthalocyanines[19]. A new approach to the molecular design of phthalocyanines is to add out of plane substitutions, such as ligands, which lie perpendicular to the main macrocycle plane[20]. The central metal element in phthalocyanines can in many cases be coordinated to an additional axial ligand, giving rise to higher solubility of these dyes compared to their planar counterparts while at the same time inhibiting aggregation tendencies. Additionally this action introduces a dipole moment perpendicular to the plane of the macrocycle. Four different electron withdrawing ligands, as detailed in chapter 3, have been attached to a titanium phthalocyanine complexe[21], producing axially substituted phthalocyanine compounds labelled A, B, C and D. The chemical structures of the compounds were modelled using semi-empirical calculations in order to obtain a picture of the geometry optimised

structure. In addition, the dipole moments of the compounds were calculated. These properties are analysed in conjunction with the optical limiting performance of each of the compounds in order to establish any definite influence of axial substituents on the nonlinear absorption properties.

Molecular Modeling

Semi empirical calculations on the axially substituted titanium phthalocyanines were carried out[22]. The ZINDO method was used in these calcultions, as this is capable of performing calculations on molecules containing transition row elements. It allows calculation of energy states and optimal geometries of molecules.

Calculations were performed on each of the axially substituted phthalocyanine compounds, A, B, C and D, for which the geometry optimized structures are shown in figure 6.6. The results of the geometry optimisation show a consistent distortion of the 'planar' macrocyclic metallo-organic ring. This 'saddle' type distortion is seen for all four molecules indicating that the axial ligands effect the planar configuration of macrocycle. Peripheral substitution on a set of titanium phthalocyanines has previously been shown to give rise to similar curvature effects[23]. The results of this work suggested that tuning of the nonlinear optical properties of the titanium phthalocyanines can effectively achieved by functionalisation of the edges of the conjugated ring.

A more tangible parameter for quantifying the influence of the axial substitutions, than induced curvature is the magnitude of the dipole moments of the molecules. Calculations, given in table 6.1, showed that the molecular dipole moments increased systematically from compound A through to D.

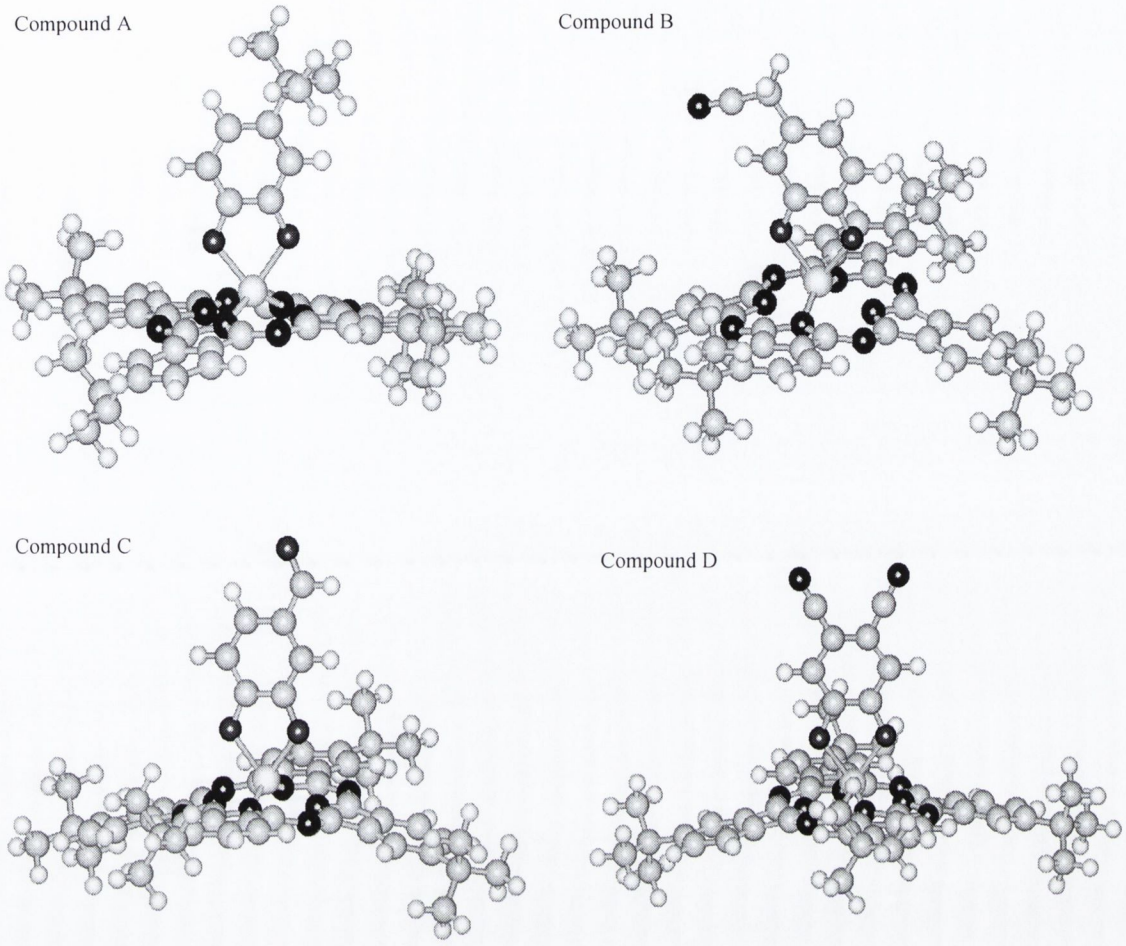

Figure 6.6 Chemical model of the axially substituted titanium phthalocyanines (a) (4-Tert.-butylcatecholato)-tetra-tert.-butylphthalocyaninatotitan(IV), (b) (4-Cyanomethyl-catecholato)-tetra-tert.-butylphthalocyaninatotitan(IV), (c) (4-Formyl-catecholato)-tetra-tert.-butylphthalocyaninatotitan(IV), (d) (4,5-Dicyano-catecholato)-tetra-tert.-butylphthalocyaninatotitan(IV)

This is in keeping the expected pattern the of electron withdrawing strength from a CH_3 group, which is relatively weakly, through to a double CN group which is know to be strong.

Optical Limiting Measurements

The optical limiting results for each of the phthalocyanine compounds are shown in figure 6.7. It is clear that the optical limiting performance varies significantly between the compounds, with Compound D showing the strongest results, C being the next most efficient, followed by B and finally A which is the weakest.

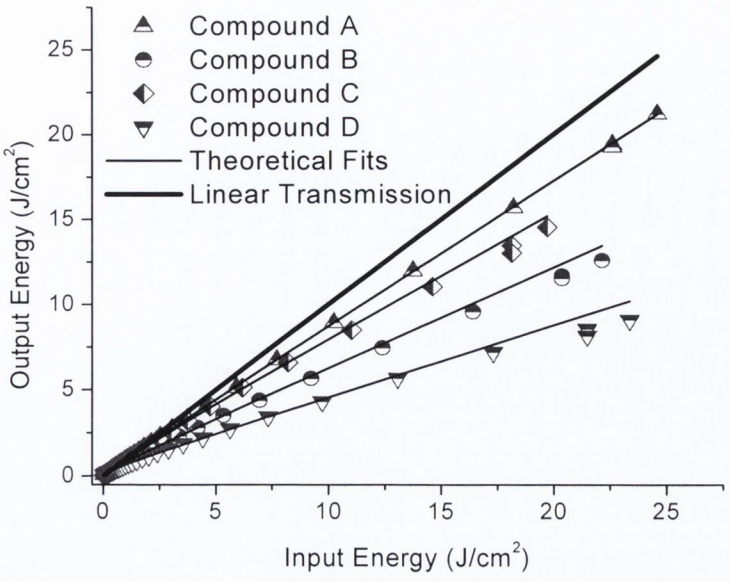

Figure 6.7 Optical Limiting of phthalocyanine Compounds A, B, C, D

Fitting of results, using the formula for the absorption given by equation (6.2) enables the calculation of Kappa (κ), the parameter used to quantify optical limiting efficiency. The calculated κ values, given in table 6.1, increase in accordance with magnitude of the molecular dipole moment. This trend is evidence that increasing the electron withdrawing effect of the axial substituent gives rise to an improved optical limiting performance of the phthalocyanine compound.

Sample	I_0 (GW/cm^2)	α_0 (cm^{-1})	Kappa	Dipole Moment (D)
Compound A	0.9±0.3	0.23±0.05	1.2±0.5	6.7±0.05
Compound B	0.7±0.2	0.55±0.05	1.3±0.5	7.08±0.05
Compound C	0.8±0.3	1.62±0.05	1.9±0.7	13.09±0.05
Compound D	1.06±0.3	0.99±0.05	2.56±1.2	20.4±0.05

Table 6.1 Parameters of Optical Limiting performance of Compounds A, B, C, D

On knowing precise values for the concentration and also the linear absorption coefficient (α_0), the values for the σ_0 and σ_{ex} parameters can be calculated using

equation (6.1). However due to concerns about sample degradation, as described in chapter 3, these values are not given here

In fact the overall relatively low values of κ, compared to what is typically found in such phthalocyanine molecules[23] are thought to be due to degradation of the samples. Nevertheless the observed trends in the nonlinear optical response of the molecules, substantiates the fact that the sample quality was sufficiently high to validate the studies carried out here.

Assessment of Optical Limiting Performance

The results show that significant control of the optical limiting performance of titanium phthalocyanines is offered by chemical modification of axial substituents. This an important result and is a very useful attribute for an optical limiting material.

6.2.2 Endohedral Metallofullerene La@C_{82}

La@C_{82} presents as quite a large endohedral type metallofullerene, for which the nonlinear absorption measurements, detailed in chapter 4, appear promising for optical limiting at certain wavelengths. Significant reverse saturable absorption was observed on picosecond irradiation, which suggests that the intersystem crossing rate in La@C_{82} is high.

Optical Limiting Measurements

Optical limiting measurements for La@C_{82} taken at different intensities at 532 nm are shown in figure 6.8. Strong optical limiting behaviour is observed with the largest reduction in the output intensity occurring at the highest incident energy.

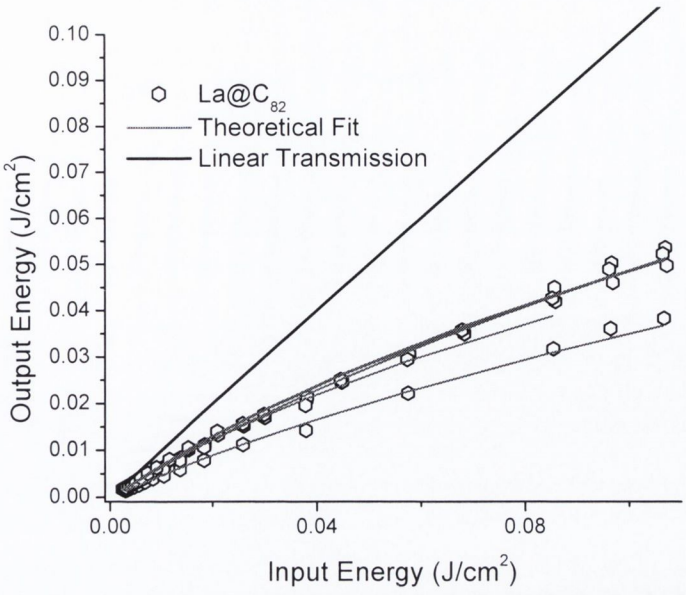

Figure 6.8 Optical limiting of La@C_{82} using 25 ps pulse at 532 nm

Optical limiting is also observed at 1064 nm, as shown in figure 6.9. On examining the graph it can be seen that initial linear behaviour gives way to rise to nonlinear behaviour and the onset of optical limiting. This change over occur above a incident threshold intensity of about 0.03 J/cm^2 where the threshold intensity indicates the point at which the data begins to adopt a nonlinear trend.

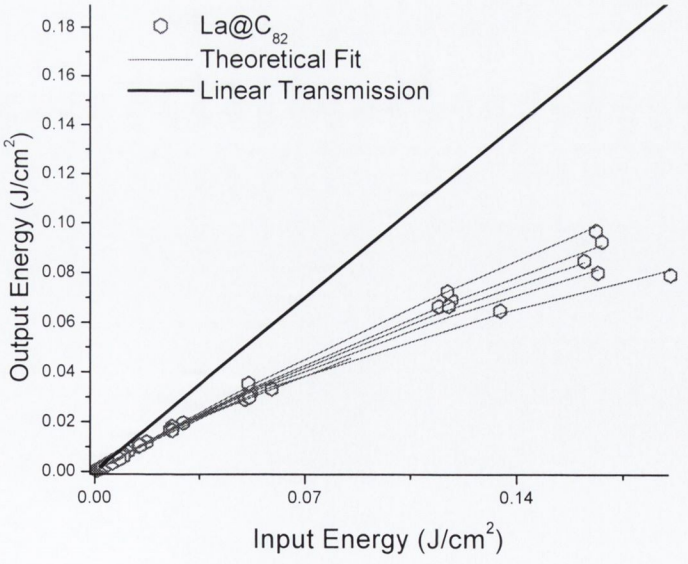

Figure 6.9 Optical limiting of La@C_{82} using 35 ps pulse at 1064 nm

Optical limiting for $La@C_{82}$ at the various wavelengths examined is shown in figure 6.10.

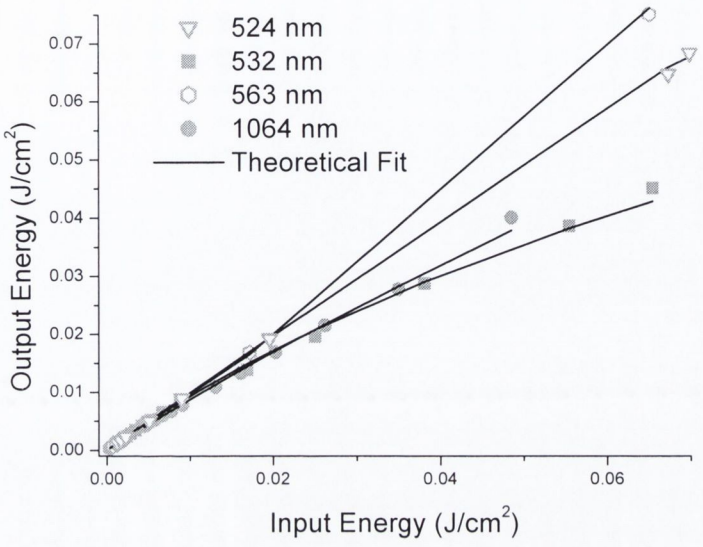

Figure 6.10 Optical limiting of $La@C_{82}$ at various wavelengths

A definite variation in the optical limiting efficiency with wavelengths is observed. This behaviour is easier to quantify from calculations of the κ values as given in table 6.2.

Wavelength (nm)	Pulse width (ps)	α_0 (cm^{-1})	I_0 (GW/cm^2)	$\lvert \Im m\, \chi^{(3)} / \Re e \chi^{(3)} \rvert$	Kappa
524	500	5.1±0.2	3.3±1.0	0.9±0.3	1.4±0.3
532	25	4.9±0.2	5.2±1.0	15.3±5.1	7.0±1.5
563	500	4.3±0.2	2.8±1.0	0.9±0.3	2.3±0.5
634	500	n/a	n/a	n/a	n/a
1064	35	0.5±0.2	10.4±1.0	5.5±1.8	3.1±0.7

Table 6.2 Wavelength dependent parameters of $La@C_{82}$ optical limiting.

A direct comparison of the values of nonlinear optical parameters obtained for the different wavelengths is difficult given the two different pulse width lasers, 500 ps and 25/35 ps that were used. The strongest optical limiting results from the use of the 25/35 ps pulses, which also provides the highest peak power (I_0) excitation. Nevertheless, the expected trend is apparent, that in regions of high linear absorption, κ values are generally smaller. Strong optical limiting is accompanied by a high ratio of the imaginary to the real $\chi^{(3)}$ values, and these again are seen mainly for the shorter pulsed excitation.

Assessment of Optical Limiting Performance

A summary of the optical limiting behaviour of $La@C_{82}$ is given in figure 6.11. The efficiency of $La@C_{82}$ optical limiting was found to exceed that of C_{60} at 532 nm. Although high linear absorption reduced the limiting behaviour at certain wavelengths in the visible region, the far greater optical limiting band width as demonstrated by efficient reverse saturable absorption at 1064 nm more than compensates for this drawback.

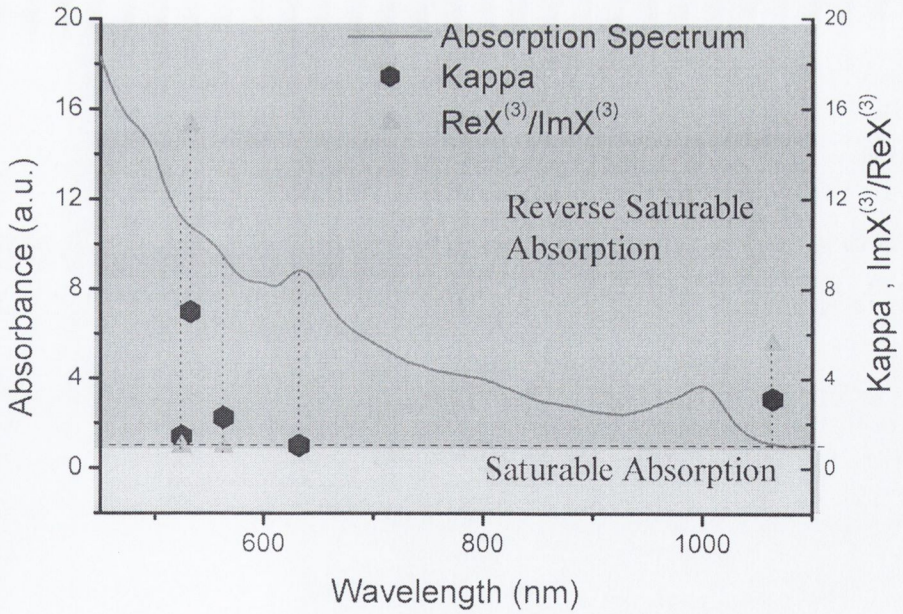

Figure 6.11 Wavelength dependence of $La@C_{82}$ Optical limiting

$La@C_{82}$ therefore possesses useful broadband optical limiting capabilities.

6.2.3 Carbon Nanotubes

A small number of studies of the optical limiting behaviour of carbon nanotubes are reported in the literature. These reports propose that the mechanism for optical limiting in nanotubes is a nonlinear scattering process similar to that which occurs in carbon black suspensions. A study by van Sun et al, has shown optical limiting behaviour in nanotubes using nanosecond pulses[11]. They also measured the response of the MWNT using short picosecond pulses and found no such optical limiting response, which leads to the conclusion that the picosecond pulses provide insufficient time for thermal processes and therefore no nonlinear scattering can take place.

The results obtained here for MWNT, partly agree and partly disagree with the literature findings. Measurements were carried out both using picosecond (25/35 ps and 500 ps) and nanosecond laser systems (6 ns).

Picosecond Nonlinear Absorption in Multiwalled Nanotubes

The wavelength dependent measurements of MWNT nonlinear absorption have been detailed in chapter 4. These have been carried out using picsecond pulses of 25/35 ps and 500 ps. At all the examined wavelengths nonlinear absorption, either saturable or reverse saturable was observed. These findings are in contrast to those reported by van Sun et al[11]. An explanation for the nonlinear absorption behaviour of the MWNT in terms of the newly discovered van Hove Singularities (VHS) is given in chapter 4.

The MWNT nonlinear absorption results have been fitted for κ, the values for which are given in table 6.3. A κ value less than one, corresponds to saturable absorption, while greater than one signifies reverse saturable absorption.

Sample	Wavelength (nm)	PulseWidth (ps)	I_0 (GW/cm^2)	$\lvert \Im m\ \chi^{(3)} / \Re e\ \chi^{(3)} \rvert$	Kappa
MWNT Solution	524	500	5.9±1.0	0.1	1.8±0.4
MWNT film	532	25	6.7±1.0	1.6	0.7±0.2
MWNT film	549	500	2.4±1.0	0.2	0.8±0.2
MWNT Solution	639	500	5.3±1.0	2.2	0.77±0.2
MWNT Film	1064	35	21.9±1.0	0.9	1.31±0.3
SWNT Solution	1064	35	19.8±1.0	1.6	0.97±0.3

Table 6.3 Wavelength dependent optical limiting parameters of MWNT

The κ values are plotted as a function of the measured MWNT VHS absorption in figure 6.12.

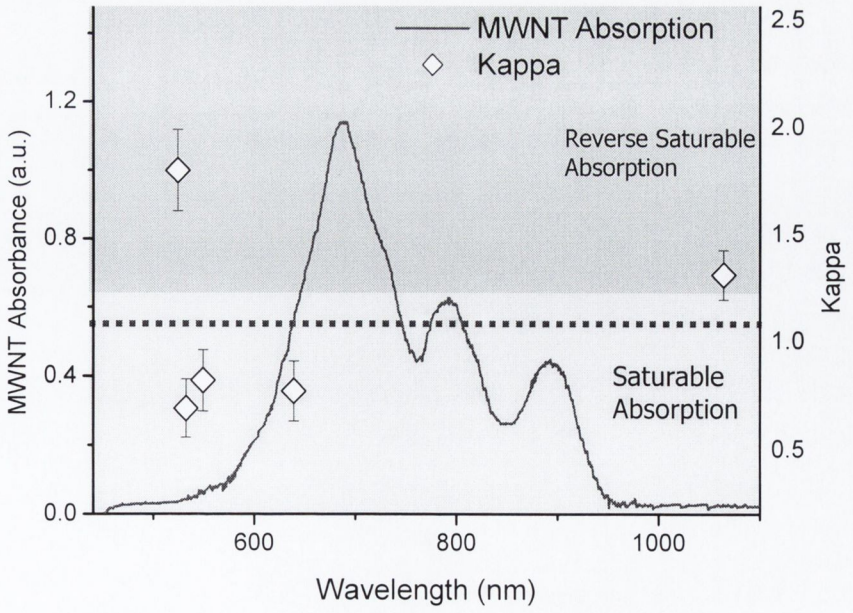

Figure 6.12 Wavelength dependence of MWNT nonlinear absorption

The typical dependence of the material nonlinear absorption on linear absorption is observed. At wavelengths where VHS peaks are absent the linear absorption coefficient is relatively low and hence reverse saturable absorption occurs such as that observed at 524 nm and 1064 nm. The in between wavelengths correspond to the onset of VHS absorption and consequently saturable absorption behaviour is observed. This dramatic effect of the VHS on the nonlinear absorption, demonstrates the important role they play in the nonlinear optical response of MWNT. This contrasts strongly with graphitic materials in which VHS are absent and the linear absorption spectrum is composed of a background π-plasmon absorption. These materials do not exhibit any significant optical nonlinear behaviour indicating that such π-plasmon absorptions do not give rise to any considerable optical nonlinearity

Nanosecond Nonlinear Absorption in Multiwalled Nanotubes

Nanosecond measurements were taken at 532 nm using 6 ns pulses. Strong optical limiting behaviour was observed as shown in figure 6.13. The optical limiting behaviour of C_{60} which is used as a reference was also measured. MWNT are found to clearly out perform C_{60} in the case of nanosecond irradiation.

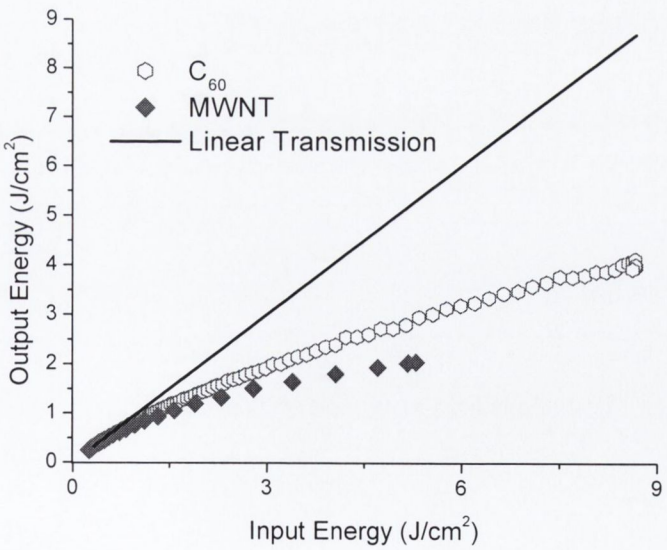

Figure 6.13 Optical limiting of MWNT and C_{60} using 6 ns pulses at 532 nm.

The nonlinear absorption behaviour of MWNT varies dramatically with pulse width for the same wavelength. The 25 ps measurement showed weak saturable absorption, while using nanoseconds gives very efficient optical liming behaviour. This suggests that different mechanisms are responsible for the picosecond and nanosecond excitation. It is suspected that, as suggested in the literature, nonlinear scattering is the dominant process for MWNT at 532 nm. This means that the optical limiting response cannot be analysed in manner used for reverse saturable absorption type limiting and therefore parameters such as κ cannot be applied. Instead, in order to quantify of the efficiency of the MWNT nanosecond optical limiting, the response of C_{60} has been measured. C_{60} is known to have a κ value in the region of 3 under these conditions[5], which is quite a significant value. The MWNT out perform C_{60} suggesting that as a nanosecond optical limiting material, nanotubes have much potential.

6.3 Conclusions

The axially substituted phthalocyanines demonstrated the possibility of controlling their optical limiting behaviour through chemical adjustment of the axial substituents. Increasing the magnitude of the axial substituent dipole moment was found to provide a corresponding increase in the optical limiting response, thereby providing a means of tuning the optical limiting in phthalocyanine materials. The endohedral fullerene La@C_{82} showed broadband optical limiting behaviour which has a picosecond response time. These are useful qualities for an optical limiting material. The carbon nanotubes showed strong optical limiting behaviour at a nanosecond response time. However, this nonlinear scattering mechanism for optical limiting is not sufficiently fast to provide a response on shorter time scales.

References

[1] C.r. Giuliano and L.D. Hess, IEEE Journal of Quantum Electronics **8**, 358 (1967).

[2] M. P. Joshi, S. R. Mishra, H. S. Rawat, S. C. Mehendale, and K. C. Rustagi, Applied Physics Letters **62** *15*, 1763 (1993).

[3] L. W. Tutt and T. F. Boggess, Progress in Quantum Electronics **17** *4*, 299 (1993).

[4] M. S. Dresselhaus, G. Dresselhaus, A. M. Rao, and P. C. Eklund, Synthetic Metals **78** *3*, 313 (1996).

[5] L. W. Tutt and A. Kost, Nature **356** *6366*, 225 (1992).

[6] S. V. Rao, D. N. Rao, J. A. Akkara, B. S. DeCristofano, and Dvgln Rao, Chemical Physics Letters **297** *5-6*, 491 (1998).

[7] J. Callaghan and W. J. Blau, Journal of Nonlinear Optical Physics & Materials **9** *4*, 505 (2000).

[8] P. Chen, X. Wu, X. Sun, J. Lin, W. Ji, and K. L. Tan, Physical Review Letters **82** *12*, 2548 (1999).

[9] Y. P. Sun, J. E. Riggs, K. B. Henbest, and R. B. Martin, Journal of Nonlinear Optical Physics & Materials **9** *4*, 481 (2000).

[10] Jason E. Riggs, David B. Walker, David L. Carroll, and Ya-Ping Sun, Journal of Physical Chemistry B **104** *30*, 7071 (2000).

[11] X. Sun, Y. N. Xiong, P. Chen, J. Y. Lin, W. Ji, J. H. Lim, S. S. Yang, D. J. Hagan, and E. W. Van Stryland, Applied Optics **39** *12*, 1998 (2000).

[12] K. Mansour, M. J. Soileau, and E. W. Vanstryland, Journal of the Optical Society of America B-Optical Physics **9** *7*, 1100 (1992).

[13] N. R. Armstrong, Journal of Porphyrins and Phthalocyanines **4** *4*, 414 (2000).

[14] J. W. Perry, K. Mansour, P. Miles, C. T. Chen, S. R. Marder, G. Kwag, and M. Kenney, Abstracts of Papers of the American Chemical Society **209**, 131 (1995).

[15] H.S. Nalwa and J.S. Shirk, *Phthalocyanines, Properties and Applications*. New York, 1996.

[16] Chunling Liu, Xin Wang, Qihuang Gong, Yunqi Liu, Wenfeng Qiu, and Daoben Zhu, Chemical Physics Letters **347** *4-6*, 378 (2001).

[17] G. de la Torre, P. Vazquez, F. Agullo-Lopez, and T. Torres, Journal of Materials Chemistry **8** *8*, 1671 (1998).

[18] P. Wang, S. A. Zhang, P. J. Wu, C. Ye, H. W. Liu, and F. Xi, Chemical Physics Letters **340** *3-4*, 261 (2001).

[19] H. S. Nalwa, M. Hanack, G. Pawlowski, and M. K. Engel, Chemical Physics **245** *1-3*, 17 (1999).

[20] T. Schneider, H. Heckmann, M. Barthel, and M. Hanack, European Journal of Organic Chemistry *16*, 3055 (2001).

[21] M. Barthel and M. Hanack, Journal of Porphyrins and Phthalocyanines **4** *7*, 635 (2000).

[22] S. O'Flaherty, Materials Ireland, Department of Physics, Trinity College Dublin, Dublin 2. Ireland.

[23] F. Henari, A. Davey, W. Blau, P. Haisch, and M. Hanack, Journal of Porphyrins and Phthalocyanines **3** *5*, 331 (1999).

Chapter 7
Conclusions

Multiphoton processes in a series of opportune organic materials have been investigated. The results demonstrate that the design of material architectures, which incorporate features to enhance the molecular hyperpolarisability is effective in improving their nonlinear optical performance. The performance of the endohedral fullerene La@C_{82}, is testimony to this. In the set of axially substituted phthalocyanines, successful control of the nonlinear optical response through chemical modulation was demonstrated. Chemical adjustment of the axial ligand was shown to influence the phthalocyanine nonlinear optical properties in a systematic fashion. Though the endohedral fullerene La@C_{82} and the axially substituted phthalocyanines fulfilled their expectations succeeding in accomplishing many of the tasks requested of them, it is the properties of the carbon nanotubes that are found to be the highlight of this thesis. Carbon nanotubes, in particular MWNT gave rise to many surprising and exciting results.

Linear characterisation was used to examine the properties which have implications for the material nonlinear optical properties. These studies showed that La@C_{82} has a broad absorption spectrum, which extends into the near infrared, therefore making it suitable for broadband nonlinear optical applications. The linear absorption of the axially substituted phthalocyanines had the normal profile of two strong absorption bands on either side of a residual absorption window in the visible. Charge transfer bands present in the absorption window, provided evidence of the influence of the axial substituents on the electronic structure of the phthalocyanines and hence can also be expected to influence their nonlinear optical behaviour. Careful linear absorption spectra revealed the presence of van Hove singularities (VHS) in MWNT, from the visible spectral region through to the far infrared. These regions

of high electronic state density can be expected to have important implications for the nonlinear optical properties of MWNT.

Wavelength dependent and nonlinear optical studies were used to determine the parameters of the nonlinear optical response of the materials. La@C_{82} showed weak real third order nonlinearities, with $\chi^{(3)}$ in the range of -10^{-12} esu and significant reverse saturable absorption. The response was found to have contain a large ultrafast component and was broadband extending into the near infrared. This amount to a dramatically improved response compared to C_{60}. The axially substituted phthalocyanines showed the expected reverse saturable absorption behaviour, the extent of which was found to depend on the axial substituent of the phthalocyanine. This demonstrated a definite influence of the axial substituent on the nonlinear optical performance of the phthalocyanines. The carbon nanotubes, in particular the MWNT showed a large negative refractive index, with $\chi^{(3)}$ as high as 10^{-9} in the case of film measurements. The nonlinear absorption showed a wavelength variation between reverse saturable and saturable absorption which was explained by the presence of VHS in the visble specral region.

Unexpected luminescence from MWNT was observed on near infrared excitation. Three photon absorption followed by upconversion luminescence is believed to be the responsible mechanism. These processes are associated with VHS in the visible region which can partially resonantly enhance the multiphoton absorption and also provide the opportunity for radiative emission. These results suggest that VHS play an important role in the linear and nonlinear optical properties of MWNT and can facilitate efficient nonlinear optical activity.

Optical limiting was investigated as a possible application for the nonlinear optical responses of the materials. La@C_{82} was found to exhibit a large broadband optical limiting with an ultrafast response. In the axially substituted phthalocyanines, effective control of their optical limiting performance was demonstrated by means of chemical adjustment of the magnitude of the dipole moment of the axial substituent. A means such as this of controlling the optical limiting response would be a powerful tool for optical limiting applications. It would help overcome difficulties such as the variation in transmission required to satisfy the different

sensor safety thresholds and sensitivity thresholds. MWNT showed effective optical limiting behaviour under nanosecond irradiation, which is presumed to originate from nonlinear scattering.

Associated Publications

1 M. E. Brennan, J. N. Coleman, T. Kobayashi, M. in het Panhuis and W.J. Blau, "Nonlinear photoluminescence from van Hove singularities in multiwalled Carbon nanotubes", submitted to Opt. Lett, (2002).

2 M. E. Brennan, S. O'Flaherty, M. Barthel, S. Maier, M. Hanack, W.J. Blau, "Tuning the Optical Limiting Efficiency of Titanium Phthalocyanines by Axial Substitution", submitted to Chem. Phys, Lett. (2002).

3 M. E. Brennan, J. N. Coleman, M. in het Panhuis, T. Kobayashi and W.J. Blau, "Nonlinear photoluminescence from multiwalled carbon nanotubes", Conference proceedings SPIE, 4461, **56**, (2001).

4 M. E. Brennan, T. Kobayashi, J. N. Coleman, M. in het Panhuis, W.J. Blau and H.J. Byrne, "Multiphoton absorption induced photoluminescence from multiwall carbon nanotubes", CLEO, Postconference Technical Digest (IEEE Cat. No.01CH37170), Opt. Soc. America, **454**, (2001).

5 M. E. Brennan, J. N. Coleman, L. Marty, H.J. Byrne, M. in het Panhuis, T. Kobayashi and W.J. Blau, "Nonlinear photoluminescence in multiwalled carbon nanotubes", Synth. Met. **119** (2001),

6 S. Curran, A. Davey, J. N. Coleman, A. B. Dalton, B. McCarthy, S. Maier, A. Drury, D. Gray, M. E. Brennan, K. Ryder, M. L de la Chapelle, C. Journet, P. Bernier, H.J. Byrne, D. Carroll, P. M. Ajayan, S. Lefrant, W.J. Blau, "Evolution and evaluation of the polymer nanotube composite", Synth. Met. **103**, (1999).